# TUNNELING ASSISTED FORBIDDEN TRANSITIONS IN THE SINGLE MOLECULE MAGNET $Ni_4$

A Dissertation Presented

by

YIMING CHEN

Submitted to the Graduate School of the
University of Massachusetts Amherst in partial fulfillment
of the requirements for the degree of

DOCTOR OF PHILOSOPHY

December 2016

Physics

# TUNNELING ASSISTED FORBIDDEN TRANSITIONS IN THE SINGLE MOLECULE MAGNET $Ni_4$

A Dissertation Presented

by

YIMING CHEN

Approved as to style and content by:

Jonathan Friedman, Chair

Donald Candela, Member

Mark Tuominen, Member

K. Sigfrid Yngvessone, Member

Rory Miskimen, Department Chair
Physics

# ACKNOWLEDGMENTS

It's my great pleasure to express my sincere appreciation to those who provide me the possibility to complete this thesis. First of all, I would like to thank my advisor Jonathan Friedman for his support, great help and priceless guidance. I would not have done nearly as much if he did not generously and patiently guide me through the whole project. I would love to thank Rafael Cassaro and professor Paul Lahti for making us samples throughout the experiment. I thank Professor Filippo Troiani for his contribution to some of the theoretic aspect of the thesis. I want to thank past and current members of Jonathan's lab for friendship and collaboration. Mohammad Ashkezari has always been of great help. His skills in programming make analyzing data an enjoyable experience. Saiti Datta fabricated the superconducting on-chip resonators, which we have been using throughout the whole project. I will thank Charles Collett for his help in my last year in the lab especially those valuable advises and suggestions for my thesis writing and my final defense. I'd also like to thank Norm Page. You have always been so kind and patient every time I bother you with broken instruments and bad solders. I am grateful to James Kubasek for his incredible ideas in designing and machining elegant devices. I'd also like to thank all the undergraduate thesis students in Jonathan's lab — Andrew Mowry, Changyun Yoo, etc. Thank all of you for the companionship in my long PhD period which left me with great memories in Amherst. Furthermore, I want to thank my parents for their unconditional support for me to chase dreams in my life. Funding and support for this research was provided by the National Science Foundation under grant No. DMR-1310135, and by the Amherst College Dean of Faculty.

# ABSTRACT

## TUNNELING ASSISTED FORBIDDEN TRANSITIONS IN THE SINGLE MOLECULE MAGNET $Ni_4$

DECEMBER 2016

YIMING CHEN

B.Sc., HEFEI UNIVERSITY OF TECHNOLOGY

M.Sc., UNIVERSITY OF MASSACHUSETTS AMHERST

Ph.D., UNIVERSITY OF MASSACHUSETTS AMHERST

Directed by: Professor Jonathan Friedman

This dissertation presents work in exploring novel quantum phenomena in single-molecule magnets (SMMs) and superconducting circuits. The degree of the freedom studied is the magnetic moment of a single molecule and the flux quantum trapped in a superconducting ring. These phenomena provide us with new insights into some basic questions of physics and may also find their application in quantum computing.

The molecule we studied is $Ni_4$ ($[Ni_4(hmp)(dmp)Cl]_4$) which can be treated as a spin-4 magnet. The large magnetic anisotropy of the molecule leads to bistability of the magnetic moment at low temperatures, with spin-up and spin-down states separated by a barrier. We applied electron spin resonance (ESR) measurements to study the forbidden transitions between spin-projection states. These transitions are usually not allowed due to the symmetry of the molecule but become possible under certain circumstance by symmetry breaking. In the first experiment, we attempted to couple the SMMs to a microstrip resonator hoping to

observe highly forbidden transitions between the states $|m = -2\rangle$ and $|m = 2\rangle$. We found that the resonator traps magnetic flux at high fields so that it fails to provide reliable results. To address this issue, we developed a mechanism that *in-situ* orients the resonator surface with the magnetic field to minimize flux trapping. In the second ESR experiment, we coupled the molecule to a 3D-cavity resonator and observed highly forbidden transitions when absorbing photons where the angular momentum changes by several times $\hbar$. These transitions are observed at low applied fields, where tunneling is dominated by the molecule's intrinsic anisotropy and the field acts as a perturbation.

In another experiment associated with superconducting circuits, we studied a single Cooper pair transistor (SCPT) driven by a microwave field, hoping to observe the Aharonov-Casher effect where flux tunneling paths can interfere and lead to a gate-charge modulation of the I-V behavior of the SCPT. We simulated the process and demonstrated that by choosing the parameters carefully, we should be able to fully suppress the flux-tunneling rate.

# TABLE OF CONTENTS

# LIST OF FIGURES

**Figure** **Page**

# CHAPTER 1

# INTRODUCTION

## 1.1 Macroscopic quantum phenomenon (MQP)

Quantum mechanics has been a successful theory in numerous applications since its birth. The validity of quantum mechanics is verified in numerous physical systems, including nuclear and subnuclear physics, molecules and also many condensed matter systems such as superconductors and super-fluids. But quantum phenomena, which are common in the microscopic world, are rarely observed in macroscopic systems, although no physical intuition is violated by supposing that quantum mechanics remains valid when pushing to the scale of "everyday life". Why do the laws of quantum mechanics fail for macroscopic objects although they are made of atoms that behave quantum mechanically? The Copenhagen interpretation actually circumvents this problem by treating quantum and classical systems differently. The projection postulate states that when a measurement is taken on a quantum system, the quantum system is projected onto a subspace that is determined by the measurement results. However, this formalism doesn't explain the apparent failure of quantum mechanics at the macroscopic level. It wasn't until the late seventies that decoherence theory [1] demonstrated that the density matrix of a quantum system becomes diagonal due to the system's interaction with the numerous degrees of freedom of the outside world, thus preventing different elements in the quantum superposition of the system's wave function from interfering with each other. This coherence time is short for a quantum system with many degrees of freedom, which explains why macroscopic objects behave classically.

In the early 1980's, Leggett and collaborators introduced the notion that it was possible to have macroscopic objects with microscopic energy scales behave quantum mechani-

cally provided they are sufficiently decoupled from the outside world [2–5]. Searching for macroscopic quantum phenomenon has been a subject of active research since then [6–8]. In our studies, we focus on two distinct physical systems that behave quantum mechanically: Single-molecule magnets (SMMs) and superconducting devices. For quantum behaviors to be treated as "macroscopic", two criteria need to be fulfilled: (1) The dynamics of the physical quantity in consideration must be described by macroscopic variables representing the collective motion of a large number of microscopic particles. For it to exhibit quantum phenomena, this degree of freedom must be independent of the microscopic degrees of freedom in the system. Therefore it is usually associated with some large energy scale such that at temperatures below such energy scales, the microscopic degrees of freedom are frozen out, making this collective coordinate a single quantum variable. For superconductors, this energy scale is provided by the superconducting energy gap. While for SMMs, it is provided by the exchange interaction between ions. On the other hand, this degree of freedom must be decoupled from the external degrees of freedom that act as a thermal reservoir. Due to its intrinsically collective nature, the macroscopic variable is coupled to many microscopic degrees of freedom in thermal equilibrium with the external environment and this circumstance is modeled by dissipation. Quantum effects are strongly reduced by dissipation so it must be extremely low in order for quantum phenomenon to be observed. (2) The states that are relevant to the quantum phenomena must be macroscopically distinct, that is to say, the difference in some parameter between the two states should be large compared to some well defined microscopic standards (e.g. the charge of the electron, the Bohr magneton).

For SMMs, the magnetic moment of the molecule is the quantum variable in consideration. It fulfills both criteria to some extent since each system consists a handful of exchange-coupled ions and the total magnetic moment is on the order of 10 $\mu_B$. So SMMs straddle the classical and quantum mechanical worlds. For the magnetic flux in a superconducting ring, both criteria are satisfied since it's a quantity that arises from all of the Cooper

pairs flowing in the ring which is in the order of $10^{10}$ and the tunneling occurs between two flux states with flux differing by $10^{10}$ $\mu_B$.

## 1.2 Quantum computing

The interest in MQP greatly increased in the 1990s, when the power of quantum mechanics for computing became a very active area of research. Unlike the classical computer that uses either 0 or 1 to represent a bit, a quantum computer exploits the quantum feature that the system can be put into a superposition state of $|0\rangle$ and $|1\rangle$, that is to say, a state can be 0 and 1 simultaneously with probability determined by quantum evolution theory. Theoretically, any two-state quantum system that can be put into such superposition states should be a good candidate quantum bit or qubit — the magnetic moment of SMMs as a vector pointing up or pointing down, supercurrent flowing in the superconducting ring clockwise or counterclockwise. But to build a practical quantum computer, a long coherence time is always the primary consideration. At the same time, the ability to control and manipulate individual qubits within a large-scale architecture is also a necessity. Compared with microscopic objects such as nuclear spins or trapped ions, which usually have long coherence times, macroscopic objects are more susceptible to the environmental noise, which leads to fast decoherence. However, macroscopic qubits have the advantage that they are easier to manipulate individually and can be more readily integrated into a large-scale architecture with existing technology.

Since the emergence of the idea of quantum computing, the study of qubits has spread to different areas of physics and achieving high quality qubits requires breakthroughs in multiple areas. Along the way to exploring new physical systems as potential qubits or extending the coherence time of known qubits, new physical phenomena start to appear that not only enrich the methodology for qubit control but also deepen our understanding of fundamental physics. In the next section I will review the progress being made in the last decade on the quantum phenomena of SMMs. Our study of the forbidden transitions

in $Ni_4$ is motivated initially by the study of atomic-clock transitions in superconducting circuits [9]. These transitions are expected to have long coherence times. The magnetic flux trapped within a superconducting ring could also be utilized as a flux qubit [10]. In our study, instead of exploring techniques to enhance the performance of a flux qubit, I focused on examining one fundamental quantum phenomenon, interference of the quantized flux as it tunnels across a superconducting ring. This part of my work is discussed separately in chapter 6.

## 1.3 Single-molecule magnets and their applications in quantum computing

An SMM is a molecule that is composed of paramagnetic transition-metal or rare-earth ions having unpaired electrons. These ions are coupled with each other to form a cluster that has a spin from a few to many times that of an electron. The well known $Mn_{12}$-ac ($Mn_{12}O_{12}(CH_3COO)_{16}(H_2O)_4$), for example, has a magnetic core of four $Mn^{4+}$ (S = 3/2) ions in a central tetrahedron surrounded by eight $Mn^{3+}$ (S = 2) ions. The superexchange interactions through oxygen bridges have the four inner and eight outer ions point in opposite directions, yielding a total spin S = 10. The exchange interaction between ions within the molecule is very strong, leaving no internal degrees of freedom inside the molecule at sufficiently low temperatures. In contrast, the exchange interaction between molecules is small. So to a very good approximation, a crystalline sample behaves at low temperatures as an ensemble of identical, noninteracting nanoscale magnets. The spin's energy can be modeled as a double-well potential, which results from a spin Hamiltonian, $H = -DS_z^2$ (Figure 1.1). One well corresponds to the spin pointing up and the other to the spin pointing down. The discrete energy levels within each well correspond to different projections, *m* = 10, 9, . . . , -9, -10, of the total spin along the easy axis of the molecule.

SMMs show fascinating quantum effects. In 1996, the macroscopic quantum tunneling of the magnetization in $Mn_{12}$ was observed by Friedman et al. [11] and shortly thereafter

confirmed by Hernandez et al. [12] and Thomas et al. [13]. A series of steps was discovered in the magnetic hysteresis loops in $Mn_{12}$ below the blocking temperature of $\sim 3$ K. These steps correspond to the enhanced relaxation of the magnetization when the energy levels in opposite wells align at certain values of magnetic field. This magnetization tunneling phenomenon has also been seen in hundreds of SMMs as well as in some high-spin rare-earth ions [14, 15]. In addition, under certain conditions, magnetic avalanches, occur in molecular magnets. These avalanches are attributed to the conversion of Zeeman energy to thermal energy, which further accelerates the magnetic relaxation. The magnetic avalanche spreads as a narrow interface that propagates through the crystal at a constant velocity [16]. This phenomenon has been studied by the measurements of the local magnetization [17] and by measurements of bulk magnetization during avalanches ignited by surface acoustic waves [18, 19], as well as theoretically by Garanin and Chudnovsky [20]. The avalanche speed is enhanced at the tunneling resonance fields [16, 18, 19].

Tunneling path interference is another interesting quantum phenomenon found in SMMs and was first observed in $Fe_8$ [21]. A physical system adiabatically following a closed path in some parameter space acquires a nontrivial phase change which is called a geometric phase [22]. $Fe_8$ has three inequivalent directions that provide a hard $x$ axis and a medium y axis within the hard plane. In zero field, the tunneling of the spin orientation has two least-action tunnel paths that pass the $\pm$y axis. Each path acquires a different geometric phase and therefore can interfere with the other. A field along the x axis changes the phase difference and thus alters the interference. In SMMs, the interference effect manifests itself as a modulation of the tunnel splitting by the magnetic field along x axis. Geometric-phase interference is observed in SMMs that have an effective Hamiltonian like that of $Fe_8$ with a single hard-axis direction [23, 24]. It is also observed in a $Mn_{12}$ variant ($Mn_{12}$-tBuAc) that has a fourth-order transverse anisotropy of the form $S_+^4 + S_-^4$ in which the system has two hard axis directions [25, 26]. Another interference effect has been reported in systems that behave as exchange-coupled dimers of SMMs [27, 28], where the effective exchange

interaction is modulated by an applied field. It is also predicted theoretically that uniaxial stress applied along the hard axis of a four-fold symmetric SMM, such as $Mn_{12}$-tBuAc, will produce a geometric-phase effect in the absence of a magnetic field [29].

The possibility of utilizing SMMs in quantum computing has been extensively examined. Leuenberger and Loss proposed in 2001 that Grover's algorithm can be implemented in a single molecule with large spin, making use of the non-degenerate transitions provided by the SMM's anisotropy [30]. This theoretical work triggered a boom in the study of extending coherence time in SMMs.

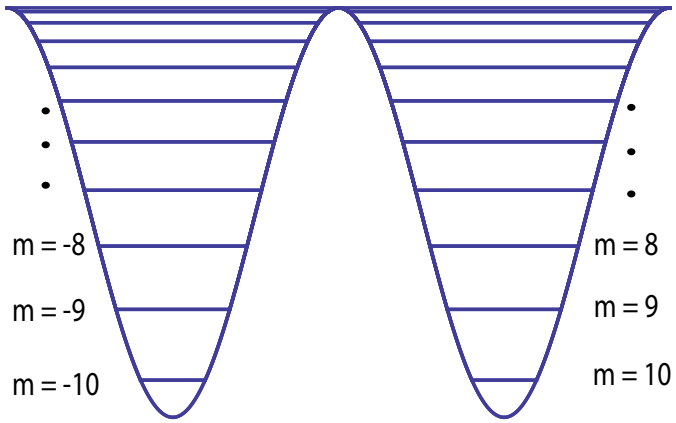


**Figure 1.1.** Double-well potential for $Mn_{12}$-ac molecule

Ideally, when excited, all the molecules will evolve with time identically and there is a fixed phase relationship between the wavefunctions of the molecules. The period during which the phase of the wavefunctions remain intact is the coherence time, $T_2$. Long coherence time can be achieved if the decoherence process in the SMMs is well understood and can be minimized. For molecular magnets, theory predicts three principal contributions to environmental decoherence: from phonons, from nuclear spins and from intermolecular dipolar interactions. 1. The coupling of spins to phonons will randomly flip the spins and lead to irreversible dephasing. To minimize the spin-lattice coupling effect, most experiments are performed at cryogenic temperature to decrease the population of phonons. 2. The interaction with the nuclear spin is another major source of decoherence. This effect

can be minimized by using isotopes with small or no nuclear magnetic moments. The substitution of deuterium for hydrogen in the molecule of $Cr_7Ni$ increases the coherence time by a factor of 3 [31]. SMMs based on polyoxometalates have been suggested as qubit candidates because they lack nuclear spins [32]. 3. Dipole-dipole interactions between spins may cause them to flip-flop (a pair of spins exchange their longitudinal angular momentum simultaneously) [33]. Dipolar interactions can be reduced by dissolving the crystal in solution to increase the average distance between molecules. This method works fine for spin 1/2 molecules such as $Cr_7Ni$ [31] and $V_{15}$ [34] since they have no zero-field anisotropy and the orientation of the molecule to the applied field is therefore irrelevant. However, for molecules with S $>$ 1/2, the existence of the anisotropy causes the energy of the qubit to depend on orientation. Such molecules are oriented randomly in solution so that they are no longer identical under field. In the case of SMMs crystals, instead of performing the experiment under low fields, Takahashi et al. [35] used a large magnetic field to polarize the molecules within a single crystal of $Fe_8$ to reduce dipolar field fluctuations.

All the techniques to reduce decoherence discussed above are aimed at reducing "external" impacts — the fluctuation of dipolar fields or the coupling to the nuclear spins. Another approach is to increase $T_2$ by having the molecule's spin itself less sensitive to the external field. This can be achieved by working at atomic-clock transitions where the transition frequency between qubit states depends quadratically on the external field, resulting in a vanishing contribution from dipolar decoherence. This strategy has been extensively used in Si based qubits [36], superconducting qubits [9] and also recently in molecular-spin qubits [37].

## 1.4 Motivation

The molecule studied in this project is $[Ni(hmp)(dmb)Cl]_4$, hereafter $Ni_4$, where hmp is the anion of 2- hydroxymethylpyridine and dmb is 3,3-dimethyl-1-butanol. This molecule resembles $Mn_{12}$ in that it has negative anisotropy, which leads to a double-well potential

similar to $Mn_{12}$. The states $|m\rangle$ and $|-m\rangle$ ($m$ = -4, -3, ...) in the different wells align at zero magnetic field and form anti-crossing states $|+\rangle \approx |m\rangle + |-m\rangle$ and $|-\rangle \approx |m\rangle - |-m\rangle$. The transition frequency between these two states at zero field is immune to first-order fluctuations of the external field and therefore has the potential to act as a qubit with a long coherence time. In our first experiment, we tried to observe these atomic-clock transitions. In another experiment, we observed highly forbidden transitions in which the absorption of a single photon permits a near reversal of the molecule's spin. This observation might have application in Leuenberger and Loss' implementation of Grover's quantum search algorithm. In the protocol they proposed, the transitions to higher energy levels involve multiphoton transitions to conserve angular momentum, which is challenging to implement in practice [30]. The realization of highly forbidden transitions lifts this requirement and could be exploited for quantum information processing.

In chapter 2, I will first elucidate the background knowledge about the $Ni_4$ molecule. The crystal structure, the Hamiltonian and the spin properties of $Ni_4$ will be discussed in detail. Following that, I will discuss the experimental techniques I applied in this project to characterize the system — electron spin resonance (ESR). In chapter 3, I will discuss in detail the experimental apparatus used in our ESR experiments, the characterization of the thin-film superconducting resonator and the fabrication of the 3D-cavity resonator, each of which is designed to work in different frequency ranges. In chapters 4 and 5, I will discuss the experiments I've done to examine forbidden transitions in SMMs. We studied transitions in two frequency ranges $\sim 5$ GHz and $\sim 115.5$ GHz, with parallel-mode and perpendicular-mode, respectively. For the low-frequency experiment, we were not be able to detect the expected transitions. One obstacle comes from the poor performance of the superconducting resonator we used. We identified magnetic flux trapping as a factor that degrades our superconducting resonator at high fields and customized the experimental setup to minimize the trapped magnetic flux. This work provided us with a resonator that offers a robust microwave environment for ESR experiments using superconducting

resonators. For the high-frequency experiment, we observed forbidden transitions assisted by inter-well tunneling between spin states. These forbidden transitions occur between two highly localized states in each well, which leads to almost a complete reversal of the spin. In chapter 6, I will discuss another experiment to study the flux-tunneling interference in a superconducting ring. This predicted effect, analogous to the well known Aharonov-Bohm effect, would manifest as a modulation of the flux-tunneling rate by an applied gate voltage.

# CHAPTER 2

# BACKGROUND THEORY

## 2.1 Introduction to $Ni_4$ SMMs

Our study on SMMs were focused on crystalline $Ni_4$. The crystal sample was synthesized by Rafael Cassaro in the Chemistry Department at the University of Massachusetts (Recipe in Appendix A). As shown in Figure 2.1, a single $Ni_4$ molecule has $S_4$ site symmetry in the crystal. The molecular core consists of four S = 1 $Ni^{II}$ ions residing on opposing corners of a distorted cube. Ferromagnetic exchange interactions between the $Ni^{II}$ ions leads to an S = 4 ground state at low temperature that is separated ($\sim 35$ K) from higher-lying states with S $< 4$ [38, 39]. So, the low-energy dynamics are that of an effective S = 4 "giant spin" with an effective spin Hamiltonian of the form:

$$\mathcal{H} = -DS_z^2 - BS_z^4 + C(S_+^4 + S_-^4) - \mu_B \vec{B} \cdot \mathbf{g} \cdot \vec{S} \tag{2.1}$$

The first three terms parametrize anisotropic magnetic interactions, which lead to the zero-field splitting of the energy levels. The last term represents the Zeeman interaction. The system can be treated as a single large spin with anisotropy that gives rise to a double-well potential (Figure 2.2). The energy levels in each well correspond to the eigenstates of $\hat{S}_z$ with $|m\rangle = |\pm 4\rangle$ as the lowest energy states in zero field. A field applied along the easy (z) axis, tilts the well and changes the energies of the levels in it, as illustrated in Figure 2.2. When levels in two wells cross with each other, the degeneracy is removed by the perturbation terms that does not commute with $S_z$ and tunneling can happen. These perturbations could come from the magnetic anisotropy or the transverse component of the magnetic field.

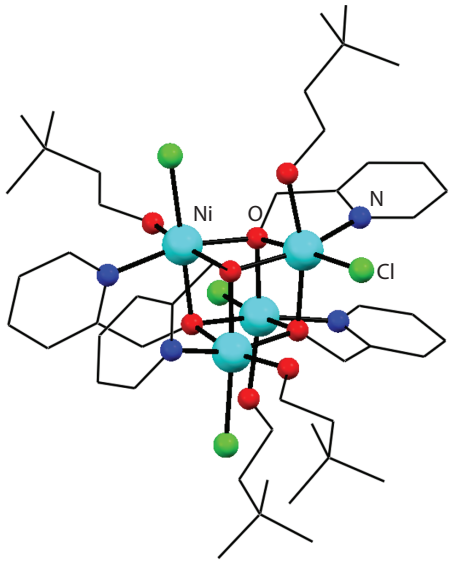


**Figure 2.1.** Chemical structure of the core of [Ni(hmp)(t-BuEtOH)Cl]$_4$ molecule

The tunneling of magnetization in $Ni_4$ was first investigated in the magnetic hysteresis response [40]. An abrupt jump of the magnetization at close to zero field reflected a fast rate of quantum tunneling of the direction of spin. The source of the fast tunneling is due to the forth-order interaction term $(S_+^4 + S_-^4)$ in the Hamiltonian. This term connects states that differ by $m = \pm 4$ in second-order perturbation theory and lifts the degeneracy of the lowest-lying $m = \pm 4$ states, leading to a significant ground-level splitting on the order of 10 MHz.

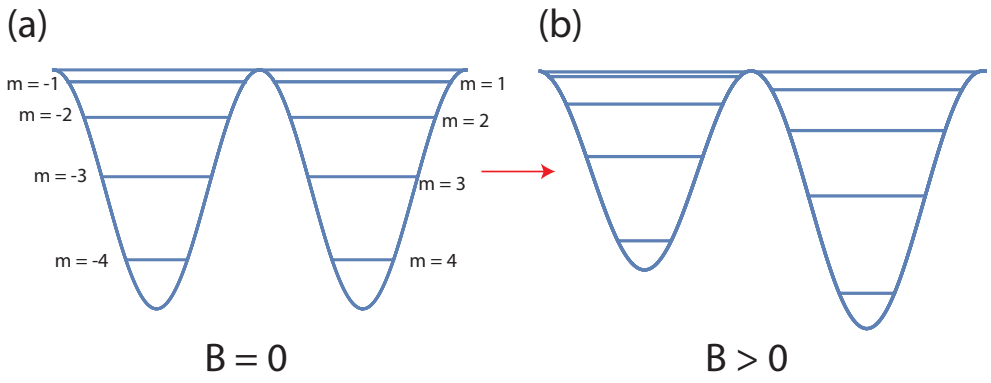


**Figure 2.2.** (a) Double-well potential in the absence of a magnetic field showing spin-up and spin-down levels separated by the anisotropy barrier. Different spin projection states $|m\rangle$ are indicated for $S = 4$. (b) Double-well potential is tilted when a magnetic field is applied along the easy axis.

## 2.2 ESR background and the Bloch Equations

Electron-spin resonance (ESR) studies the interaction between electronic magnetic moments and magnetic fields and is frequently considered to be in the microwave branch of spectroscopy. In our experiment, a resonator is used to sustain the microwave oscillation. The sweeping of the static field shifts the energy levels and when the energy difference matches the resonance frequency of the resonator, energy is absorbed, which leads to the resonance frequency shift and quality factor suppression. Figure 2.3 shows the simulated field dependence of the energy of $Ni_4$ and the measured ESR absorption spectrum.

To understand the lineshape of the ESR spectrum, I will first review the magnetic resonance phenomenon and the Bloch equations that describe the motion of the magnetization in a bulk crystal. Here I start with the Bloch equation for non-interacting spins [41, 42]. The motion of each spin's magnetic moment in a magnetic field is found simply by equating the torque applied by the field to the rate of change of angular momentum: $\frac{d\vec{J}}{dt} = \vec{\mu} \times \vec{B}$. By substituting $\vec{\mu} = \gamma \vec{J}$ ($\gamma$ is gyromagnetic ratio), we get $\frac{d\vec{\mu}}{dt} = \gamma \vec{\mu} \times \vec{B}$. When considering a macroscopic sample having an enormous number of spins ($> 10^{15}$), $\vec{M}$, the net magnetic moment of the sample, obeys the same equation as the individual dipoles but with the ad-

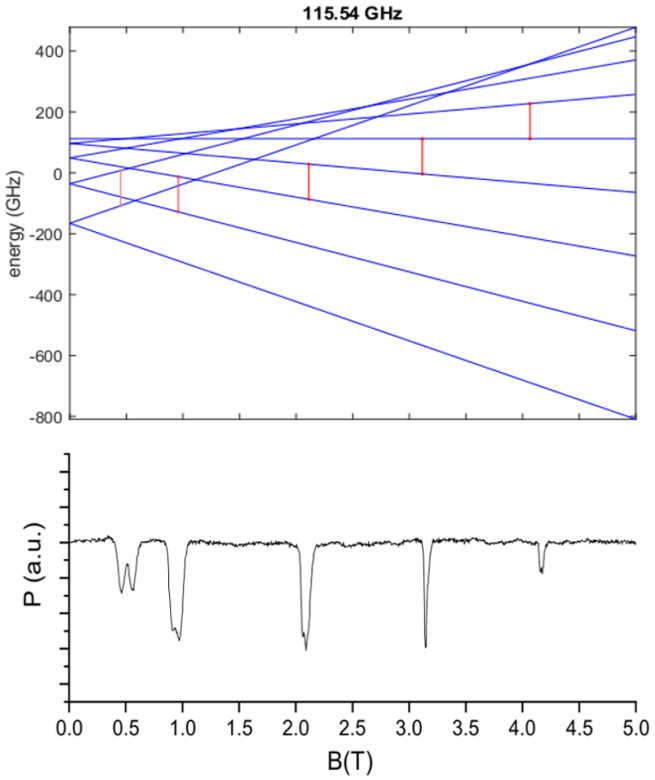


**Figure 2.3.** Diagrams to show the connection between energy-level transitions and the absorptive ESR spectra. The energy diagram (top) is for $Ni_4$ with the magnetic field along the crystal easy axis. An ESR spectrum from $Ni_4$ at 9 K with the ac field in the hard plane of the crystal is shown in the lower panel. The red arrows indicate the ESR transitions with f $\sim$ 115.5 GHz. One can determine the anisotropy parameters and $g$ factor by analyzing the ESR spectrum in the framework of the spin Hamiltonian model.

dition of relaxation terms. The Bloch equations for the magnetization of the sample in the laboratory coordinate frame {X, Y, Z} can be expressed as:

$$\frac{dM_X}{dt} = \gamma(\vec{M} \times \vec{B})_X - \frac{M_X}{T_2} \tag{2.2a}$$

$$\frac{dM_Y}{dt} = \gamma(\vec{M} \times \vec{B})_Y - \frac{M_Y}{T_2} \tag{2.2b}$$

$$\frac{dM_Z}{dt} = \gamma(\vec{M} \times \vec{B})_Z - \frac{M_Z - M_0}{T_1} \tag{2.2c}$$

The relaxation terms on the right of the equations express the fact that in equilibrium, the magnetization will be parallel to Z. That is, the X and Y components tends to vanish and the Z component relaxes to $M_0$, a value that depends on the applied longitudinal field. The $T_1$ term accounts for the relaxation of the magnetization along the longitudinal direction. This process is associated with exchanging energy with the environment, e.g., through absorption and emission of phonons. The magnetization can also relax within the XY plane. This process describes how fast the spins lose relative phase and is also called decoherence. Here the decoherence time $T_2$ is different than the relaxation time $T_1$ because, in contrast to longitudinal decay, transverse decay conserves energy. So there's no necessity for them to be the same. $T_2$ is always shorter than $2T_1$.

Now consider a linearly oscillating field along the $X$ axis $\vec{B}_1 = \hat{X} B_1 \cos\omega_1 t$ as a perturbation to the system, where $B_1$ is small enough to avoid saturation. The oscillating field can be decomposed into two equal-magnitude and oppositely rotating fields,

$$\begin{aligned} \vec{B_1} &= \vec{B}_1(+) + \vec{B}_1(-) \\ &= \frac{1}{2}B_1(\hat{X}\cos\omega_1 t + \hat{Y}\sin\omega_1 t) + \frac{1}{2}B_1(\hat{X}\cos\omega_1 t - \hat{Y}\sin\omega_1 t) \end{aligned} \tag{2.3a}$$

Here we transform the coordinate frame to one that rotates at $\omega_1$ clockwise $\{$x,y,z$\}$. The clockwise component $\vec{B}_1(+)$ is then a constant vector with magnitude $\frac{1}{2}B_1$ along the x axis in the rotating frame while the counter-clockwise component $\vec{B}_1(-)$ rotates with $2\omega_1$ in the opposite direction and can be averaged out. In addition, the longitudinal field is changed from $B_0$ to $b_0 = B_0 + (\omega_1/\gamma)$ in the rotating frame:

$$\frac{dM_x}{dt} = \gamma M_y b_0 - \frac{M_x}{T_2} \tag{2.4a}$$

$$\frac{dM_y}{dt} = \gamma(\frac{M_z B_1}{2} - M_x b_0) - \frac{M_y}{T_2} \tag{2.4b}$$

$$\frac{dM_z}{dt} = -\gamma\frac{M_y B_1}{2} - \frac{M_z - M_0}{T_1} \tag{2.4c}$$

If we introduce a complex magnetization $M_+ = M_x + iM_y$ and add Eqn. 2.4a and $i$ times Eqn. 2.4b, we get:

$$\frac{dM_+}{dt} = -M_+\alpha + i\gamma M_0 B_1/2 \tag{2.5}$$

where $\alpha = \frac{1}{T_2} + \gamma b_0 i$. Here we replaced $M_z$ by $M_0$ because $M_z$ differs from $M_0$ by a factor of order $B_1^2$. We obtain the steady-state solution by setting $\frac{dM_+}{dt}$ to zero and define $\omega_0 = \gamma B_0, \omega = -\omega_1$:

$$M_x = \frac{\gamma M_0}{2} T_2 \frac{(\omega_0 - \omega)T_2}{1 + (\omega - \omega_0)^2 T_2^2} B_1 \tag{2.6a}$$

$$M_y = \frac{\gamma M_0}{2} T_2 \frac{1}{1 + (\omega - \omega_0)^2 T_2^2} B_1 \tag{2.6b}$$

Under equilibrium, the magnetization is a constant in the rotating frame and therefore is rotating at frequency $\omega$ in the laboratory frame. We can relate $M_X$ to the component $M_x$ and $M_y$ in the rotating frame by:

$$M_X = M_x \cos\omega_1 t + M_y \sin\omega_1 t \tag{2.7}$$

We see from Eqn. 2.6 that both $M_x$ and $M_y$ are proportional to $B_1$. Knowing that $B_1 = H_1$ in Gaussian units, we can write:

$$M_X = (\chi' \cos\omega_1 t + \chi'' \sin\omega_1 t) H_1 \tag{2.8}$$

with the quantities $\chi'$ and $\chi''$ defined by using Eqn. 2.6:

$$\chi' = \frac{\gamma M_0}{2} T_2 \frac{(\omega_0 - \omega)T_2}{1 + (\omega - \omega_0)^2 T_2^2} \tag{2.9a}$$

$$\chi'' = \frac{\gamma M_0}{2} T_2 \frac{1}{1 + (\omega - \omega_0)^2 T_2^2} \tag{2.9b}$$

It is convenient to regard both $M_X(t)$ and $H_X(t)$ as being the real parts of complex function $M^C(t)$ and $H^C(t) = H_1(\cos\omega_1 t + i\sin\omega_1 t)$. By defining the complex susceptibility $\chi$ by $\chi' - i\chi''$, we find [42]:

$$M^C(t) = \chi H^C(t) \tag{2.10}$$

or

$$M_X(t) = Re\{\chi H^C(t)\} \tag{2.11}$$

$\chi'$ is the ac susceptibility component in-phase with the driving field and $\chi''$ is the ac susceptibility component out-of-phase with the driving field. A crystal sample with susceptibility $\chi$ increases the inductance of the resonator by a factor of $(1+\chi)$. Therefore the resonator impedance becomes:

$$Z = iL_0\omega(1+\chi) + \frac{1}{iC_0\omega} + R_0 = iL_0\omega(1+\chi') + (L_0\omega\chi'' + R_0) + \frac{1}{iC_0\omega} \tag{2.12}$$

where $L_0$, $C_0$ and $R_0$ are the inductance, capacitance and resistance of the resonator in the absence of a sample. $\chi'$ changes the inductance of the resonator. Its response does not absorb power from the signal source and, in ESR, corresponds to dispersion. Meanwhile, $\chi''$ modifies the resistance, which corresponds to absorption. The absorption curve is a Lorentzian line with width at half height: $\Delta\omega = 1/T_2$. The Bloch equations are derived for classical spins. They can be generalized to any two-state quantum systems interacting with electromagnetic fields. Eqn. 2.9 also applies to the multiple projection states of the molecule where $\omega$ here corresponds to the photon energy and $\omega_0$ is the energy gap between the two states involved in absorbing a photon. Each absorption peak shows up when the photon energy matches the energy gap (Figure 2.3). Eqn. 2.9 describes both frequency-swept ESR, where $\omega_0$ is fixed and $\omega$ is varied, and field-swept ESR detected at a constant microwave frequency ($\omega = \omega_c$) where $\omega_0$ is field dependent. Hence, the field-domain line

shape is a projection of the frequency-domain line shape determined by the dependence of energy difference $\omega_0$ on $B$: $|\frac{\partial\omega_0}{\partial B}|^{-1}$.

The line width can be attributed to two different mechanisms: homogenous broadening and inhomogeneous broadening. A homogenous broadening lineshape corresponds to each spin experiencing the same magnetic field and the total lineshape is a sum of many lines with the same frequency and linewidth, therefore still has a Lorentzian shape. For a inhomogeneous broadening lineshape, each spin will precess with a slightly different Larmor frequency and will lead to a Gaussian distribution most of the time. The overall contribution to decoherence can be described more accurately by the time constant $1/T_2^* = 1/T_2 + 1/T_{inhom}$ where $T_2^*$ is usually much smaller than $T_2$. $T_2^*$ places a lower bound on the value of $T_2$.

Besides the linewidth of each absorption peak, the intensity (denoted as the area of each resonance peak) is also informative in understanding each transition. The intensity depends on the Boltzmann population difference $(N_i - N_f)$ and transition matrix element between the initial and final states, i.e.,

$$I \propto (N_i - N_f)|\langle f|\hat{\mathcal{H}}_{rad}|i\rangle|^2 = (N_i - N_f)g\mu_B|\langle f|\hat{S}\cdot\vec{B}_{rad}|i\rangle|^2 \tag{2.13}$$

where $|i\rangle$ and $|f\rangle$ represent the initial and final projection states, respectively, $N_i$ and $N_f$ are the populations associated with these two states, and $\hat{\mathcal{H}}_{rad}$ describes the dipole operator associated with the ac magnetic field of the incident radiation.

The forbidden transitions we examined can be explained by the matrix element of the transition. To get a better sense, we rearrange the Hamiltonian terms in Eqn. 2.1 to get the following form:

$$\mathcal{H} = -DS_z^2 - BS_z^4 - g_z\mu_B S_z B_z + \mathcal{H}' \tag{2.14}$$

$\mathcal{H}'$ contains all symmetry-breaking operators that do not commute with $S_z$ — the transverse anisotropy term $\hat{S}_+^4 + \hat{S}_-^4$ and the transverse component in the magnetic field. In the

absence of $\mathcal{H}'$, $S_z$ is a conserved quantity so that the Hamiltonian shares the same eigenstates with the operator $\hat{S}_z$. The matrix element $\langle i|\hat{S}_z|f\rangle$ is non-zero only if $|i\rangle = |f\rangle$, and $\langle i|\hat{S}_x|f\rangle$ is non-zero only if $|i\rangle$ and $|f\rangle$ differ in $m_s$ by $\pm 1$, the standard single-photon selection rule. That is to say, if $\vec{B}_{rad}$ is parallel to the $z$ axis, no transition is allowed; if $\vec{B}_{rad}$ is perpendicular to the $z$ axis, transitions can only take place between consecutive $m$ states within one potential well. An essential point, as will now be seen, is that with the $\mathcal{H}'$ term included, $\mathcal{H}$ does not commute with $\hat{S}_z$ anymore and $m$ is no longer a good quantum number. Each energy eigenstate $|E_n\rangle$ is a superposition of the states $|m\rangle$:

$$|E_n\rangle = \sum_m |m\rangle \langle m|E_n\rangle = \sum_m c_m |m\rangle \tag{2.15}$$

$c_m$ refers to the weight of state $|m\rangle$ in $|E_n\rangle$ and $|c_m|^2$ normalizes to 1 by $\sum_m |c_m|^2 = 1$. Due to the state mixing, transitions that are previously forbidden by the selection rule can take place. In particular, transitions between localized states in different wells can be observed. Our ESR experiments in both parallel mode and perpendicular mode should allow us observe such highly forbidden transitions:

*Forbidden transition under a longitudinal ac field (parallel mode)*

Forbidden transition under a longitudinal ac field can occur when the energy levels in opposite potential wells approach each other so that they mix into each other. Let's consider the $|m = \pm 4\rangle$ and $|m = \pm 2\rangle$ pairs in $Ni_4$. Without $\mathcal{H}'$, $|m = 4\rangle$ is degenerate with $|m = -4\rangle$, and $|m = 2\rangle$ is degenerate with $|m = -2\rangle$ at $B_z = 0$. The transverse anisotropy term $\hat{S}_+^4 + \hat{S}_-^4$ couples $|m = 2\rangle$ to $|m = -2\rangle$ to first order and $|m = 4\rangle$ to $|m = -4\rangle$ to second order in perturbation theory. The tunnel splitting between the $|m = \pm 4\rangle$ states is $\sim$10 MHz and that for the $|m = \pm 2\rangle$ pair is $\sim$3.7 GHz; thus, the degeneracy is lifted significantly and leads to superposition states:

$$|S\rangle \simeq a_m |m\rangle + b_m |-m\rangle \tag{2.16a}$$

$$|A\rangle \simeq a_m |m\rangle - b_m |-m\rangle \tag{2.16b}$$

where $m = 2$ or $4$, $a_m$ and $b_m$ are determined by the value of $B_z$, with normalization: $|a_2|^2 + |b_2|^2 = 1$. At $B_z = 0$, $a_m = b_m = \frac{1}{\sqrt{2}}$ and the states $|S\rangle$ and $|A\rangle$ are totally delocalized having the same probability to be found in each well. The matrix element $\langle S|\hat{S}_z|A\rangle$ is maximized at $B_z = 0$, indicating the ESR signal is strongest. As $B$ increases, the matrix element $\langle S|\hat{S}_z|A\rangle$ decreases and the states become more and more localized. Figure 2.4 shows the simulated energy diagram for $|m = \pm 2\rangle$ pair and the matrix element $\langle S|\hat{S}_z|A\rangle$ as a function of field. The matrix element is significant at a field below $\sim 1000$ Oe, implying that a forbidden transition is observable in that region. Also of note is that at $B$ close to zero, the energy difference of the two states depends quadratically on $B$ and the transition frequency between the two states is unaffected by the environmental field noise to first order.

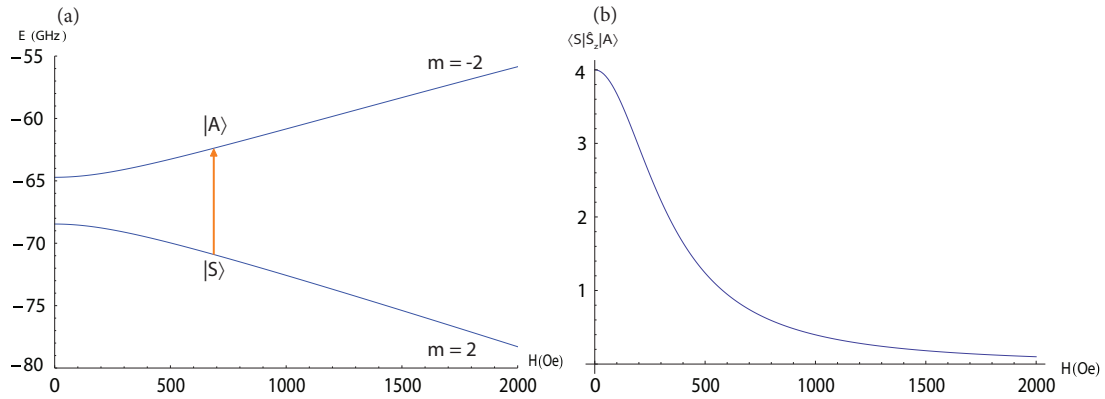


**Figure 2.4.** (a) Simulated energy diagram shows the energy splitting between $|m = \pm 2\rangle$ states at magnetic field close to zero. The orange arrow shows the transition at 5 GHz which is excited by an ac field along the easy axis. (b) Matrix element $\langle S|\hat{S}_z|A\rangle$ decreases as magnetic field increases from zero.

*Forbidden transition under a transverse ac field (perpendicular mode)*

The introduction of $\mathcal{H}'$ makes the final state of the transition ($|f\rangle$ in Figure 2.5) have a significant amplitude of levels in the opposite well if it is nearly aligned with an energy level in that well. Under such a scenario, $|f\rangle$ becomes delocalized with significant amplitude of states in both wells. The transition to this superposition state could occur because $|f\rangle$ contains a component in the same potential well as $|i\rangle$ that allows for the $\Delta m = 1$ transition. Since a significant amplitude of $|f\rangle$ belongs to a level in the other potential well, there is a substantial probability for a direct transition from one well to the other. Consider the transition shown in Figure 2.5, where $|i\rangle \simeq |m = -4\rangle$ and $|f\rangle$ is a superposition state of $|m = -3\rangle$ and $|m = 2\rangle$. The mixing of $|m = -3\rangle$ and $|m = 2\rangle$ is a consequence of the perturbation applied by $\mathcal{H}'$, where the $\hat{S}_+^4 + \hat{S}_-^4$ term couples states with $m$ differing by 4, and $\hat{S}_x B_x$ term couples states with $m$ differing by 1. Thus, the tunneling between $|m = -3\rangle$ and $|m = 2\rangle$ is produced by matrix-element products like $\langle m = -3| \hat{S}_-^4 |m = 1\rangle \cdot \langle m = 1| \hat{S}_- |m = 2\rangle$ in second-order perturbation theory. The tunnel splitting is significant ($\sim$ 1 GHz). Figure 2.5 shows the simulated matrix element $\langle i|\hat{S}_x|f\rangle$. At most fields, the matrix element is zero while a strong peak shows up at $\sim 6000$ Oe close to the tunneling field of $|m = -3\rangle$ and $|m = 2\rangle$. This indicates that a significant amount of the $|m = -3\rangle$ state is mixed with the $|m = 2\rangle$ state near the crossing enabling a $\Delta m = 1$ transition.

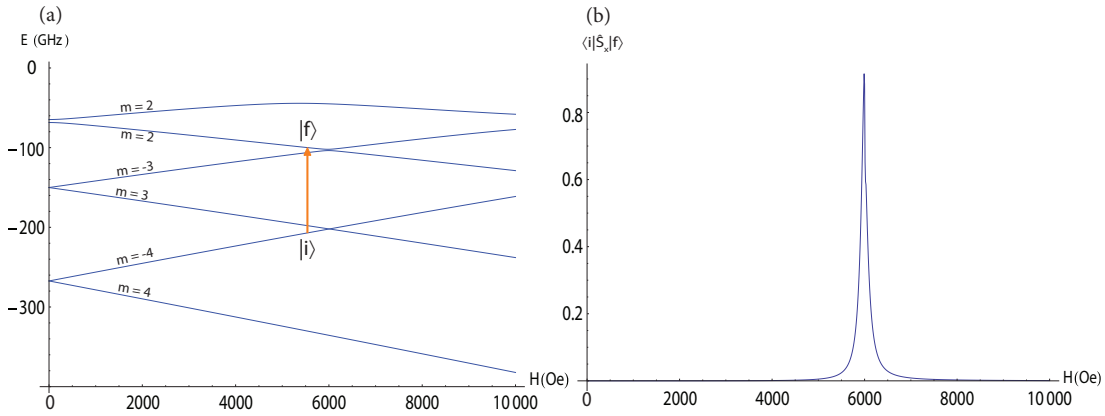


**Figure 2.5.** (a) Simulated energy diagram with magnetic field up to 1T. The orange arrow shows the transition from nominally $|m = -4\rangle$ to $|m = 2\rangle$ states under an ac field perpendicular to the easy axis of the crystal. (b) Matrix element $\langle i|\hat{S}_x|f\rangle$ of the transition peaks at the field where $|m = 2\rangle$ crosses $|m = -3\rangle$.

# CHAPTER 3

# EXPERIMENT

Interest in molecular magnets has attracted researchers to employ various experimental techniques to study them. $Ni_4$ SMMs have been characterized by ESR [43–48], magnetization measurements [39, 40, 44] and heat-capacity measurements [47, 49, 50]. A continuous-wave ESR technique is applied in our study to investigate the transitions between various levels of the molecule's spin. In this chapter, I will discuss the instrumentation we used in our ESR experiment.

The main part of the experimental setup is the Quantum Design Physical Property Measurement System (PPMS), which provides a measurement environment with base temperature of 1.7 K and maximum static field of up to 9 T. The crystal sample is coupled to a resonator that is situated at the end of a probe inside the PPMS. Once inserted into the main chamber of the PPMS, the probe with sample mounted is pumped down and filled with $\sim$ 20 mbar He gas to ensure thermal contact between the chamber and the sample. The superconducting coil inside the PPMS provides a static magnetic field along the axis direction. Microwave signals are generated by an Agilent 83650B signal generator with an output frequency up to 50 GHz. On occasions that higher frequencies are needed, an active $4\times$ multiplier (Millitech AMC-15-RFH00) and a doubler (Millitech MUD-06-LF000) are employed that can multiply the output frequency by a factor of 8. The output signal is routed into the top of the probe and then transmitted into the low-temperature regime of the PPMS via a coaxial transmission line ($\sim$5 GHz) or WR-10 waveguide ($>$ 100 GHz) where it interacts with the sample-resonator system. The reflected or transmitted signal, modified by the resonator-sample system, is measured at room temperature. We use a diode detector

(Pacific Millimeter DD) for high frequency (>100 GHz) signals and a crystal detector (HP 8472A) for low frequency (∼5 GHz) signals.

In our study, we investigated ESR transitions under a longitudinal ac field and a transverse ac field as discussed in chapter 2. In our first experiment, we attempted to observe the transition between the superposition of spin states $m_s = \pm 2$ at a static magnetic field close to zero (red arrows in Figure 3.1). For this experiment, a superconducting thin-film resonator with resonance frequency $\sim 5$ GHz that generates an ac field aligned with the static field was used. This configuration of fields is sometimes called parallel mode ESR since the static field and oscillating field are along same direction. In our second experiment, we examined the transitions that involve a resonance frequency of $\sim$ 115.5 GHz for $Ni_4$ (green arrows in Figure 3.1). A 3D cylindrical cavity resonator is implemented in this situation. The configuration for this experiment is called perpendicular mode because the ac field is perpendicular to the dc field in this case.

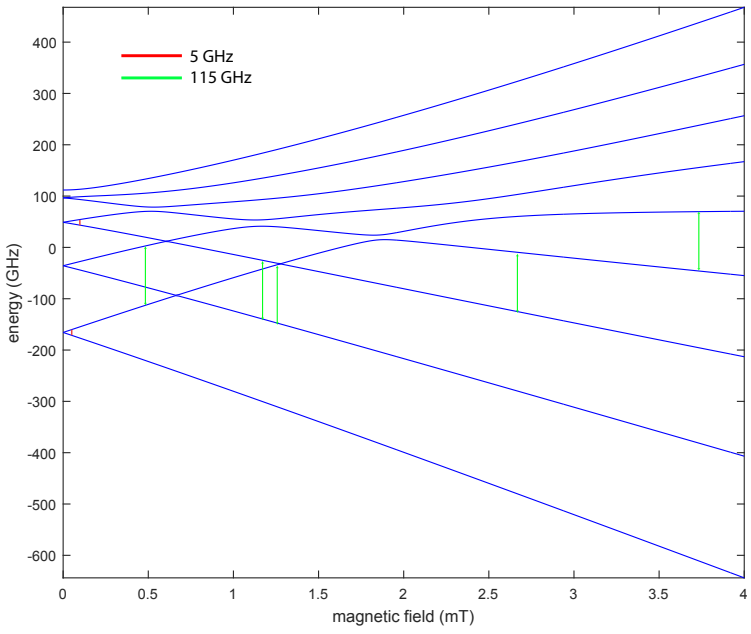


**Figure 3.1.** Transitions excited by a longitudinal ac field with a frequency of 5 GHz (red arrows) and by a transverse ac field with a frequency of 115 GHz (green arrows)

In the next two sections, I will describe in detail the setup of the parallel and perpendicular ESR experiments respectively. Focus will be on the design of the custom-built probe and the fabrication of the superconducting thin-film resonator and the 3D cavity resonator.

## 3.1 Parallel-mode ESR experiment setup

### 3.1.1 Probe

The parallel ESR experiment involves the transmission of microwave signals in the range of 4 GHz – 6 GHz. Semi-rigid coaxial cables are well suited to transmit signals in this frequency range. Figure 3.2 shows the design of the probe. The assembly consists of a circuit board holder (CBH) that encases the on-chip resonator, the coaxial cables and the G10 control rod (this part is used to align the resonator circuit board, which will be discussed in chapter 4). The semi-rigid coaxial cable loop is made of four sections: Two straight lengths extend from the chamber top plate to around $4''$ above the CBH. They have stainless steel outer sheath and a silver-plated BeCu inner conductor to prevent excessive thermal conduction along the transmission cables from the room temperature top plate to the working space. Two shorter sections of cable within the working space are made from copper, which is non-magnetic to avoid distorting of the field near the resonator. They are terminated with brass SMA connectors that are crimped on to the cable. We avoid using solder for the electrical connections since most common solders are superconducting at the experimental operating temperatures or are too soft to provide a secure mechanical connection. The thin-film resonator is deposited on the surface of a silicon wafer that is attached to the circuit board. The circuit board (CB) is sitting inside the CBH with female SMA connectors on both sides that provide electrical connection to the coaxial cable.

### 3.1.2 Superconducting resonator

Superconducting thin-film resonators have been extensively used to read out superconducting qubits [9]; they can be thought of as one-dimensional transmission-line resonators

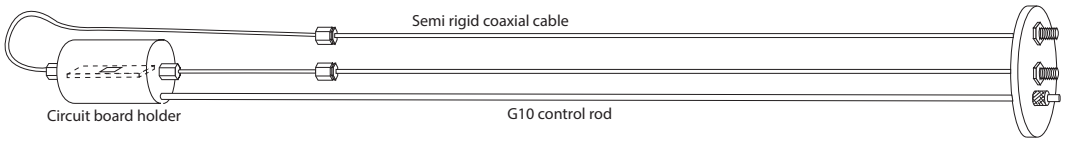


**Figure 3.2.** Design of the probe for low-frequency (5 GHz) parallel-mode ESR experiment.

in which the central conductive line is deposited as a thin film onto the silicon wafer [51]. Our resonator is made out of niobium and has a negligible resistance below the critical temperature of Nb ($\sim$10 K), exhibiting a quality factor of $\sim 10^4$. Other than this, thin-film resonators have the following advantages over 3D cavity resonators: 1) The size of the resonator can be much smaller than the size of the 3D cavity required for the same frequencies. 2) The ac magnetic field is concentrated in a smaller volume near the conducting strip, which allows measurement of photon absorption in very small crystals while ensuring a strong field at the sample location.

The resonances for such resonators occur when the length of the resonator is equal to half the wavelength of the incoming radiation frequency and for integer multiples of this fundamental frequency. A typical thin-film resonator used in this experiment is shown in Figure 3.3. The width of the center niobium stripline is 4 μm, and to make the resonator chip small, the center line is designed to have a snake pattern while it still maintains the property of a one dimensional harmonic oscillator. The central line is capacitively coupled to feed lines via $\sim 50$ μm gaps at both ends (Figure 3.3(c)). Ground planes on the sides of the center conductor are also capacitively coupled to the center strip. The metal is deposited as a thin layer of 100 nm onto the surface of a Si wafer. [52] The fundamental resonance frequency $\omega_r$ is determined by the speed of light ($c$) and the length of the resonator ($l$):

$$\omega_r = \frac{c}{\epsilon_{eff}^{1/2}} \frac{\pi}{l} \tag{3.1}$$

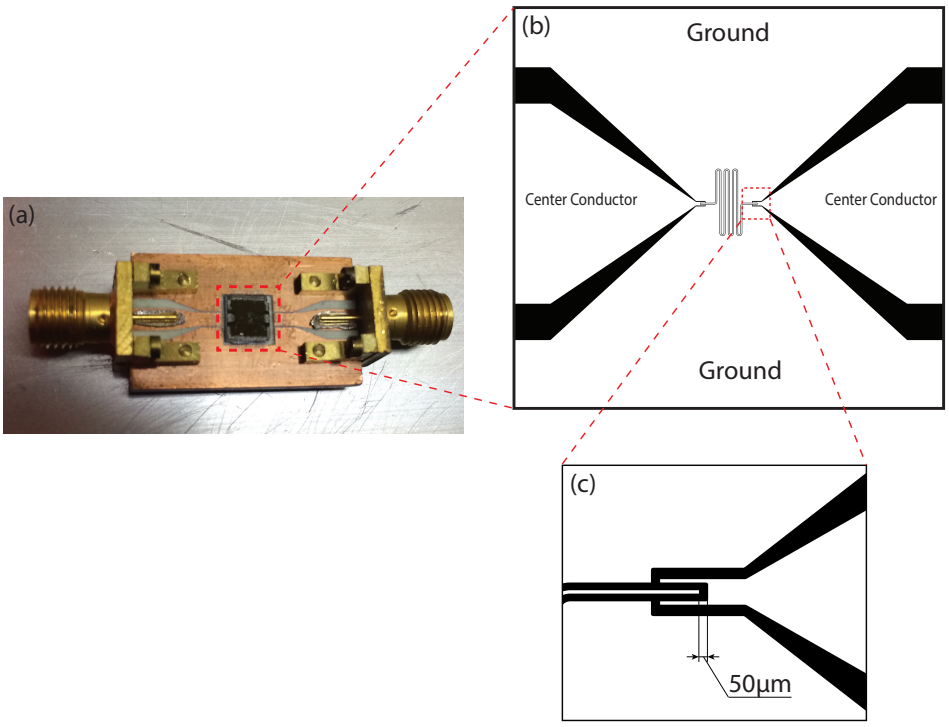


**Figure 3.3.** Thin-film resonator: (a) Circuit board and mounted resonator. Wire bonds are densely formed around the edge of the chip for connection between the conducting strips and between the ground planes. (b) The surface layout of the thin-film resonator. The black is insulator and the white is conductor. (c) Enlarged view of the gap between center leads.

Although the effective dielectric constant ($\epsilon_{eff}$) is difficult to calculate exactly, the frequency can still be adjusted linearly by adjusting the length. For the purpose of our experiments, we aimed for resonance frequencies around 4 - 5 GHz. In practice, we fabricated a series of resonators on one wafer with various lengths to obtain the desired resonance frequency.

The on-chip feed lines are electrically connected to the CB central strip with Al wire bonds, and the ground planes of CB and the resonator chip are wirebonded as well (Figure 3.3(a)). The ratio of the width of the central conducting strip of the CB to the gap is calculated to have 50 Ohm impedance to match the resonator's impedance so as to mini-

mize any parasitic resonances. The CB is held in the cylindrical CBH, which fits tightly inside the PPMS inner chamber.

The sample crystal is laid flat with one of its facets on the surface of the resonator to ensure the strongest coupling. The projection of the easy axis of the crystal on the resonator surface is along the direction of local ac field. Ideally, the circuit board should be aligned with the inner chamber axis so that the static magnetic field is in the same plane of the resonator chip. In such a setup, the static field and the ac field should both be along the z axis of the chamber and the easy-axis of the crystal is at an angle of $\theta$ to the fields. We found in our experiment that any deviation of the resonator off the vertical direction will allow magnetic field to penetrate the surface of the resonator. The resonance is lost at modest fields ($\sim$ 50 Oe) and this renders the resonator unserviceable. To overcome the misalignment issue, we designed a mechanism that can tune the orientation of the chip board *in situ*, which offers a stable environment for ESR measurements. This part of the work will be discussed in detail in chapter 4.

## 3.2 Perpendicular-mode ESR experiment setup

### 3.2.1 Probe

Perpendicular-mode ESR is generally employed to study the transitions with $\Delta m_s = \pm 1$. For $Ni_4$ the energy separations between adjacent projection energy levels are usually 100 GHz –150 GHz. Coaxial cables become very lossy at this frequency and we adopted waveguide instead for signal transmission. A cylindrical cavity is used as a resonator to couple the sample to the radiation. The design of the probe is shown in Figure 3.4. The probe consists of the waveguides and the cylindrical cavity. The sample is mounted inside the cavity at the end of the probe. The signal coming out of the multiplier and doubler is multiplied in frequency by a factor of 8 and covers the frequency range of 100 - 150 GHz. The signal is then transmitted to the resonant cavity (located in the sample chamber at cryogenic temperatures) via the $\sim$1-m-long WR-10 waveguide (gold-plated stainless steel

with ∼3 dB attenuation). A mylar window, at the top of the probe, creates a vacuum seal (not shown in the figure). Power is controlled with an adjustable attenuator at the room-temperature end of the waveguide. A phase shifter is used to control the frequency of waveguide resonances to mitigate their influence on the cavity resonance. Reflected power is monitored using a directional coupler and a diode detector.

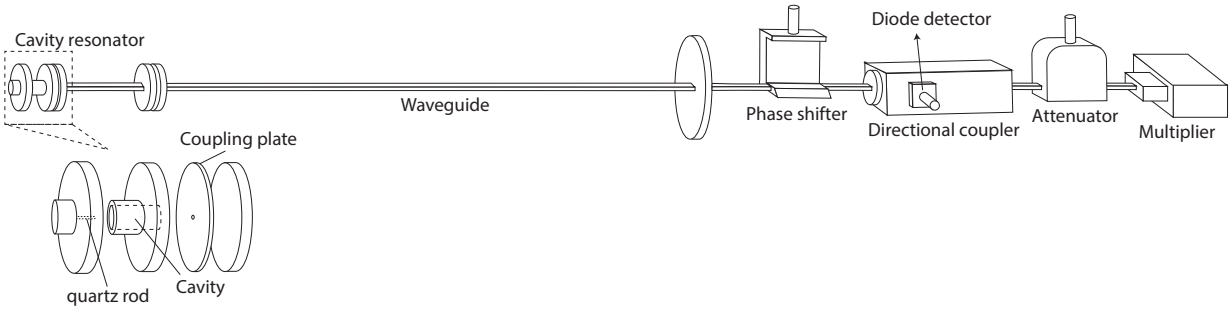


**Figure 3.4.** Design of the probe for high-frequency (∼115.5 GHz) perpendicular-mode ESR experiment.

### 3.2.2 Resonant Cavity

A microwave resonant cavity is a box fabricated from high-conductivity metal with dimensions comparable to the wavelength. At resonance, the reflection of microwaves from the walls forms a three-dimensional standing-wave interference pattern known as a resonant mode. The cavity used in our experiment is made out of oxygen-free copper and composed of three parts — a bottom plate, a hollow cylindrical tube and a coupling plate on top (Figure 3.4). The three parts are screwed together tightly to form a cylindrical space. By theory, cylindrical cavities can support both $\mathrm{TE}_{mnp}$ and $\mathrm{TM}_{mnp}$ modes, where $m$, $n$ and $p$ refer to the number of half-cycle variations in the angular, radial and longitudinal directions, respectively. For a cylindrical cavity of inner radius $R$ and length $d$, the resonance frequencies are calculated to be [53]:

$$[\omega_{mnp}]_{TE} = \frac{1}{\sqrt{\mu\epsilon}}\sqrt{\frac{x'^2_{mn}}{R^2} + \frac{p^2\pi^2}{d^2}} \tag{3.2}$$

$$[\omega_{mnp}]_{TM} = \frac{1}{\sqrt{\mu\epsilon}}\sqrt{\frac{x_{mn}^2}{R^2} + \frac{p^2\pi^2}{d^2}} \tag{3.3}$$

where $x_{mn}$ and $x'_{mn}$ are the $n_{th}$ roots of the $m_{th}$ order Bessel function and its first derivative, respectively. Around the resonance frequency, the rf amplitude follows a Lorentzian function:

$$A(\omega) = \frac{I}{4(\omega - \omega_0)^2 + (2\pi\Gamma)^2} \tag{3.4}$$

where the resonance frequency is $f_0 = \omega_0/2\pi$, $\Gamma$ is the full width at half-maximum, $I$ is the intensity of the resonance peak. The quality factor of the cavity is given by:

$$Q = \frac{f_0}{\Gamma} \tag{3.5}$$

The cavity used in our experiments has $d = 6.86$ mm and $R = 1.69$ mm, respectively, and has a fundamental $TE_{011}$ mode of $\sim$ 115.54 GHz at low temperature. For this mode, the current flows round the circumference of the cavity walls and the end plate and no current flows between the walls and the endplate. We use this mode as our working resonance frequency. However according to Eqs. 3.2 and 3.3, the $TM_{111}$ mode is degenerate with the $TE_{011}$ mode. To separate the two modes, a small quartz rod is placed at the center of the end plate along the axis; the rod acts as a small perturbation to the $TM_{111}$ mode while it has negligible effect on the $TE_{011}$ mode. This causes the resonance frequency of $TM_{111}$ to shift to lower frequency by $\sim$500 MHz. Our sample is coupled to the $TE_{011}$ mode of the cavity and when the sample is on resonance with the cavity, the characteristics of the resonance change slightly, producing a shift of the resonant frequency and a change in $Q$.

The microwaves from the waveguides were coupled to the cavity through a small coupling hole. The coupling hole acts as an electric-field node and couples to the magnetic field inside the cavity. The diameter and thickness of the aperture determines the coupling strength. A large diameter ensures strong coupling, but decreases the sensitivity and the Q factor of the cavity. A small diameter, on the other hand, limits the incident power but

ensure higher cavity Q value and sensitivity. We tried coupling plates with various hole sizes and tried different offsets of the hole position from the center. We finally obtained a Q factor of $\sim 8000$ with a coupling plate with hole diameter is 0.64 mm and thickness 0.76 mm. In addition, to guarantee a high Q of the cavity for each run of the experiment, we cleaned the cavity carefully before mounting the sample. All pieces of the cavity are first polished with Simichrome metal polish to clean off the oxide on the surface. Then they are ultrasonic cleaned in toluene for 15 min. Afterwards each piece is ultrasonic cleaned in isopropanol for another 15 min. After each cleaning, the pieces are blown dry to remove any residues. We characterized the cavity at room temperature with the oscilloscope first. Three pieces of the cavity are first loosely attached together with screws. Then the cavity is mounted to the probe and microwave signal is sent in with a frequency range that covers the resonance frequency. We gently tighten the screws until a resonance dip shows up on the screen of the oscilloscope that indicates the cavity is formed. The characterization process is repeated after mounting the sample to ensure the cavity mode is intact.

The sample crystal is mounted to the bottom of the cavity with grease where the local rf field is along the radius direction. The easy axis of the crystalline sample is first aligned vertically, then tilted at angles ($\theta_H$) towards the azimuthal direction (Figure 3.5). The crystal is oriented this way to ensure the rf field is perpendicular to the easy axis. The angle between the field and the x direction of the hard plane of the crystal ($\phi_H$) has some minor effect on the ESR result based on the simulation, which will be discussed in Chapter 5. ESR spectra are taken at various values of $\theta_H$ and $\phi_H$.

### 3.2.3 Measurement

A static magnetic field $\vec{H}$ is applied along the axis of the cavity. The rf field of the $TE_{011}$ mode at the sample position is along the radius of the cavity, perpendicular to the static field. The static field is slowly swept continuously from 0 to 40 kOe and, at each field, we measured the reflected power as a function of frequency, recording the dependence with

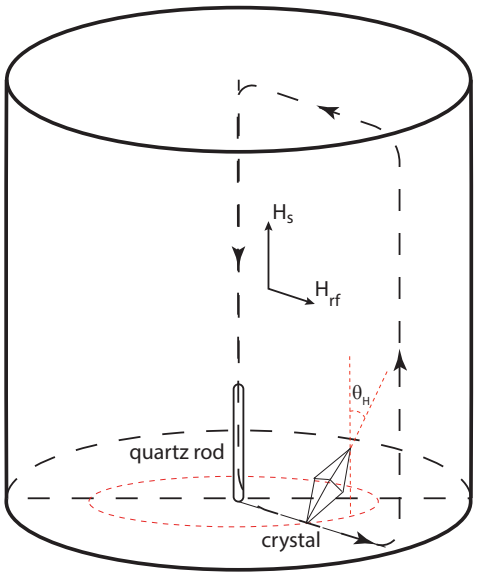


**Figure 3.5.** The positioning of the sample crystal inside the cylindrical cavity. The directions of the static field and the rf field at the sample position are shown. The dashed line with arrow demonstrates the distribution of the magnetic field of the TE011 mode of the cavity. The easy axis of the crystal is tilted towards the azimuthal direction (red dashed lines assist identifying the crystal direction).

an oscilloscope. The measurement is repeated for various values of $\theta_H$. Since we do not have *in-situ* control of the orientation of the crystal, between each run of experiment, we warmed up the probe to room temperature to manually adjusted the orientation. The exact value of $\theta_H$ is determined by fitting the spectrum.

In the process of measurement, the resonance spectrum can be affected by 60 Hz noise due to a ground loop. To overcome this issue, all the electronic instruments — the multiplier, the microwave generator, the oscilloscope — are isolated from ground and powered by one power strip which is also not grounded. The whole experimental setup is then connecting to the ground through a thick grounding strip. Thus every device has only one path going into the ground and no ground loop is present.

Figure 3.6 displays the reflected power as a function of frequency at $H = 0$ and $\theta_H = 26.6^\circ$. The resonance peak is deeply embedded in the background signal which is due to the high-order harmonics of the long waveguide. This background must be subtracted to extract the resonance from the cavity. To do so, we shifted the background using the phase shifter to locate the resonance dip on a plateau of the background harmonics where it can be more easily distinguished: We narrow the frequency range (Figure 3.6) and fit the curve with a sum of a quadratic function (green background curve) and a Lorentzian (red resonance curve). Since the background pattern presumably doesn't change as we sweep the DC field, we used the fitted quadratic function to represent the background for all fields. After subtraction of this background, a Lorentzian fit is applied to extract the resonance frequency ($f_{res}$) and the quality factor ($Q$) of the cavity. The resonance frequency shown in this figure is a bit less than 115.5 GHz. This is because each time we change the direction of the sample ($\theta_H$), we open up the cavity and then rebuild it afterwards by screwing in the covering plate. This may vary the length of the cavity which leads to some variation of resonance frequency.

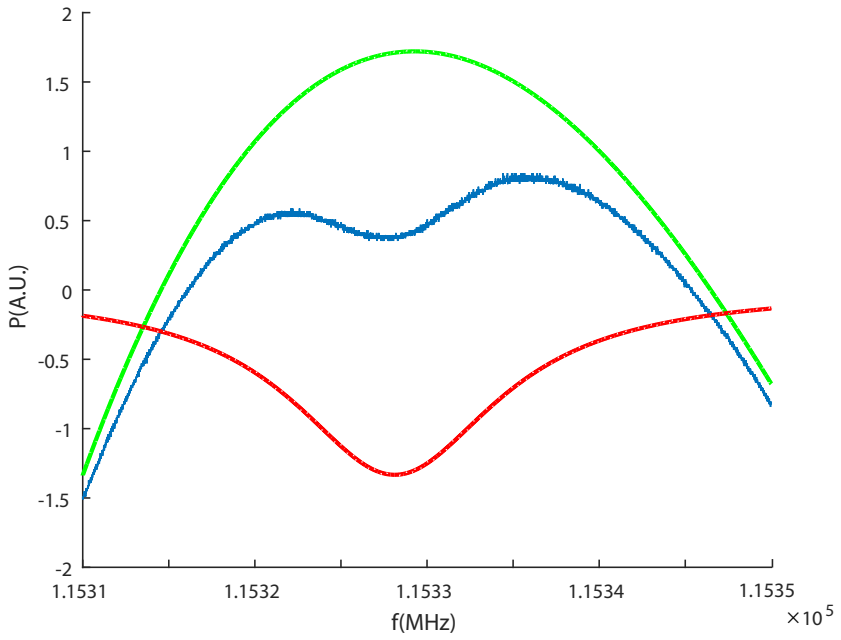


**Figure 3.6.** Lorentzian fit of the resonance peak. The reflected power spectrum (blue) is decomposed into a sum of the background harmonics (green) and a Lorentzian (red).

# CHAPTER 4

# FLUX TRAPPING IN SUPERCONDUCTING THIN-FILM RESONATORS

## 4.1 Background

Superconducting thin-film resonators have drawn a lot of attention in the field of ESR experiment in the past decade due to their high quality factor and small modal volume. In the process of characterizing our resonator, we ran into some difficulties: The magnetic-field dependence of the resonant frequency and quality factor of the resonator, $f_{res}(H)$ and $Q(H)$, were not reproducible between experimental runs. This makes the resonator unreliable for use in an ESR apparatus. In addition, the resonator degrades rapidly with increasing field so that the resonance peak disappears at a field above several hundreds Oe. Several causes of the poor performance of the resonator have been proposed such as faulty SMA connections, improper impedance matching, defective wire bonds from the resonator chip to circuit board, etc. After excluding all these possibilities, we were able to pinpoint the issue to magnetic vortices generated by the magnetic field component perpendicular to the superconducting film surface. The motion of these vortices can produce significant dissipation for high-frequency signals [54–57]. In the following, I will describe the source of the dissipation that occurs in our niobium resonator.

We chose niobium as the material for our resonator because it has a high critical temperature (9.2 K) that is well above the working temperature inside our PPMS (1.8 K). Unlike a Type I superconductor that has an abrupt phase change between superconducting state and normal state at a field $H_c$, a Type II superconductor has two phase changes happening at $H_{cl}$ and $H_{cu}$. Below $H_{cl}$, a good Type II superconductor excludes the field completely. Above

$H_{cl}$, the field is partially excluded, but the specimen remains electrically superconducting. At a field above $H_{cu}$, the flux penetrates completely and superconductivity vanishes. In the intermediate state, $H_{cl} < H < H_{cu}$, magnetic vortices are generated circulating around the magnetic flux. To understand this mixed state in type II superconductors, I will give some background on Ginzburg-Landau (GL) theory, which was a great triumph in explaining the spacial inhomogeneity in superconductors.

The GL theory introduces a complex pseudowave function $\psi$ as an order parameter that can be thought of as the wavefunction of the superconducting electrons. The local density of superconducting electrons is given by $n_s = |\psi|^2$. An important result of GL theory is the derivation of the dynamics of $\psi$ by the differential equation:

$$\frac{1}{2m^*}\left(\frac{\hbar}{i}\nabla - \frac{e^*}{c}\mathbf{A}\right)^2 \psi + \beta|\psi|^2\psi = -\alpha(T)\psi \tag{4.1}$$

where $e^*$ and $m^*$ are the charge and effective mass of the superconducting electrons. $\alpha$, $\beta$ are experimental parameters that are functions of temperature. $\mathbf{A}$ is the magnetic vector potential. Based on this equation, the GL theory introduces a characteristic length, the GL coherence length $\xi$, which describes the distance over which $\psi(r)$ can vary without appreciable energy increase. Another characteristic length in superconductors is the penetration depth, $\lambda$, which describes how the magnetic field decreases exponentially into the interior of a bulk superconductor:

$$h(x) = h(0)e^{-x/\lambda} \tag{4.2}$$

where $h$ denotes a magnetic field component parallel to the surface and $x$ is measured from the surface into the superconductor. Based on the magnitude of these two lengths, we can define Type I and Type II superconductors. Consider the situation close to $H \approx H_c$ so that the superconductor and normal domains coexist. The domain wall between normal $\{\mathrm{N}\}$ and superconducting $\{\mathrm{S}\}$ material is displayed in Figure 4.1 for different values of $\xi$ and $\lambda$. In generating such an NS interface, energy is either absorbed or released by

the material and this energy is described as the surface energy, which is defined as the additional energy gained or lost in creating the NS interface. The energy can be treated as a balance between the positive diamagnetic energy and the negative condensation energy due to the superconductivity[1]. The values of the two characteristic lengths determines the sign of the surface energy, and therefore determines the flux penetrating pattern:

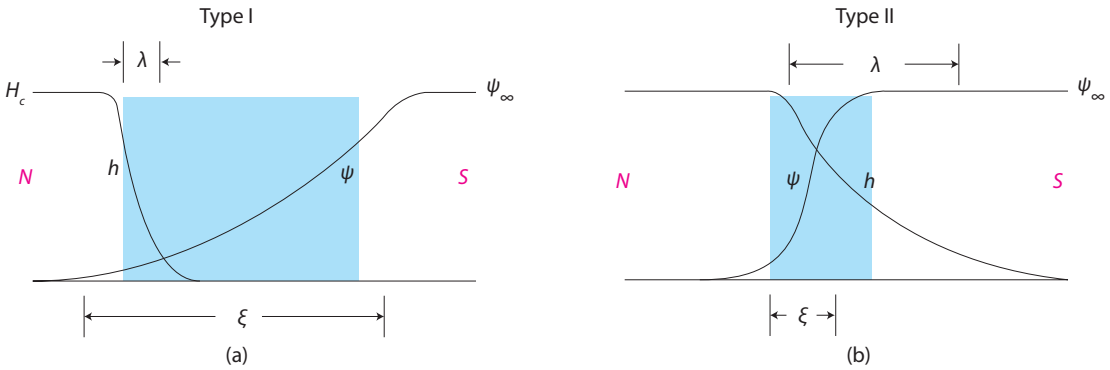


**Figure 4.1.** The domain wall between the normal and superconducting material for Type I superconductor (a) and Type II superconductor (b) close to $H_c$.

1. $\xi \gg \lambda$ (Figure 4.1(a)):

If $\lambda$ is small, the field drops abruptly at the interface and there is a region of thickness $\sim (\xi - \lambda)$ from which the field is held out which contributes to a positive diamagnetic energy. While on the superconducting side, superconductivity is partially "damaged" in a region of thickness $\xi$ near the interface and we lose the condensation energy $H_c^2/8\pi$. This leads to a positive surface energy which is exactly the case of Type I superconductor. Since energy is lost in creating NS boundaries, when the field is large enough to penetrate into the Type I superconductor, it tends to form laminar boundaries to save energy.

2. $\lambda \gg \xi$ (Figure 4.1(b)):

[1]Diamagnetic energy refers to the energy to exclude the magnetic field out and the condensation energy refers to the energy reduction from normal state to superconducting state.

The argument above is reversed for large $\lambda$, which leads to a negative surface energy for Type II superconductors. Any flux-bearing normal regions in the superconductor prefer to subdivide to attain lower energy. This situation is very different from that encountered for Type I superconductors, where the sufaces are less numerous. The flux penetrates into the material in a way to maximize the surface to volume ratio of the normal region. Calculations show that the formation of filaments with small diameters ($\sim \xi$) is more energetically favorable. Each filament is carrying a quantum of flux $\Phi_0 = \frac{hc}{2e}$. The quantization of the flux trapped in a superconductor ring is a consequence of the condition that $\psi(r)$ is a single-valued function. There is a vortex of supercurrent rotating around the axis toward the filament center. In the core of a vortex the electrons whirl around so quickly as to exceed the critical-current density and locally destroy superconductivity; this generates a normal-phase region in the core of the vortex.

The degrading of the niobium resonator's performance is caused by the movement of the vortices through interactions with the oscillating current in the resonator. The dissipation can be explained by at least two mechanisms: 1) The energy may dissipate as Joule heating when the normal-phase electrons of the vortices interact with the thermal vibrations of the lattice during the movement. 2) The superconducting-phase electrons in the bulk of superconductor will interact with the normal-phase electrons in the vortices and will be "normalized" at the leading edge of the moving vortex.

The dissipation caused by the vortex movement can be characterized by the flux-flow vortex viscosity $\eta = \Phi_0 B_{c2}/\rho_n$, where $\rho_n$ is the normal-state resistivity of the material, and $B_{c2}$ is the upper critical field. A current density $J$ flowing through a superconductor exerts a Lorentz force on the vortices, $F_L = \vec{J} \times \Phi_0 \hat{n}$, where $\hat{n}$ is normal to the surface of the film. In addition, any practical superconductor inherently contains various materials defects which produce vortex pinning. In the simplest case, the pinning potential wells $U(x)$ can be assumed to be harmonic with spring constant $k_p$, giving a pinning force $\mathbf{F}_p = k_p \mathbf{x}$. The vortex equation of motion at zero temperature is given by:

$$\eta\dot{\mathbf{x}} + k_p\mathbf{x} = \mathbf{F}_L \tag{4.3}$$

The interplay between the viscous force and the pinning will determine the frequency dependence of the vortex response. At low frequencies ($\sim$MHz) the pinning will dominate and the response will be primarily elastic, while at higher frequencies the viscosity will become more important and the response will be more dissipative. Our experiment is performed at a microwave frequency of $\sim$5 GHz, which is well within the dissipative range.

Controlling vortex formation and behavior is a major challenge in any ESR experiment in which superconducting resonators are used. One attempt to minimize the energy dissipation is to somehow constrain the movement of the vortices using the flux-pinning effect. By following this idea, Bothner et al. have had considerable success in implementing antidots on their superconducting resonators to pin the vortices to the crystal lattice and achieve a significant increase of the quality factor [58]. Alternatively, since the amount of trapped flux is proportional to the component of the magnetic field normal to the film, the magnetic field can be applied parallel to the thin film if experimentally feasible. Several research groups make use of superconducting striplines or resonators for ESR experiments and some report the alignment issue to require careful attention or consideration [59–70]. In working with niobium coplanar-waveguide resonators in our experiment, we found that a half-degree tilt of the field renders the apparatus unserviceable at a field of 100 Oe. To address this issue, we developed an apparatus to allow for precise *in-situ* control of the resonator orientation.

## 4.2 Design of the apparatus

Figure 4.2 shows a CAD drawing of the lower portion of our ESR probe in both assembly and exploded forms. The assembly consists of a Nb resonator chip bonded to the circuit board (CB), the circuit board holder (CBH), and the gear mechanism, along with

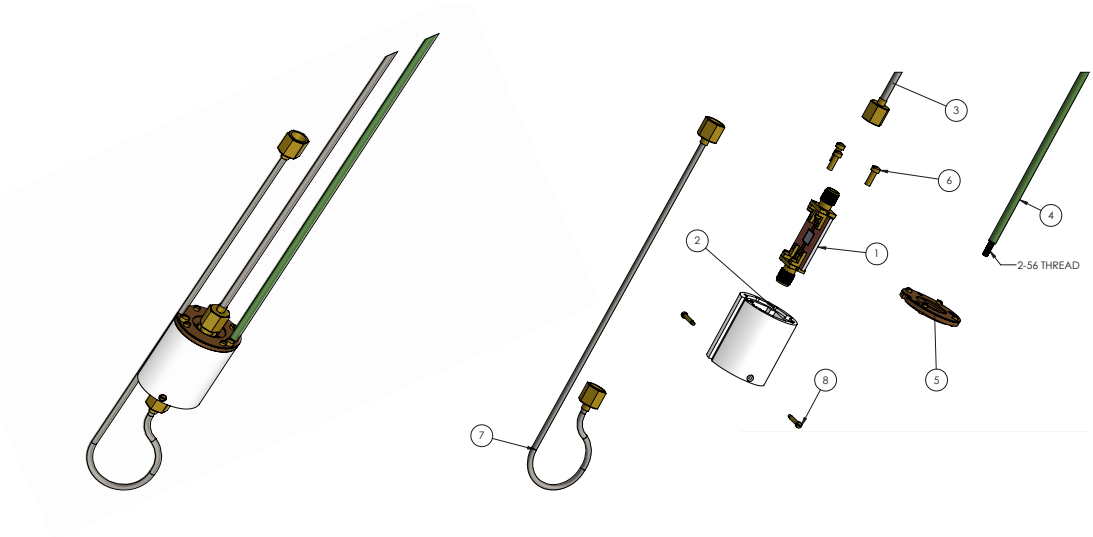


**Figure 4.2.** CAD drawing ESR probe, assembled and exploded views. The CBH holds CB. The top SMA connector on CB passes through the gear mechanism, which controls CB's rotation about the bottom pivot pins. The green G10 rod extends from the gear mechanism through the probe top plate, allowing manipulation of the mechanism *in situ*. The semi-rigid coaxial cables pictured also extend through the top plate. ① CB; ② CBH; ③ & ⑦ non-magnetic, semi-rigid copper coaxial cable (Tek-Stock, UT-085C-LL); ④ threaded G10 control rod (.125" diameter, 2-56 thread on last .25"); ⑤ gear mechanism; ⑥ 2-56 x .25" brass screw to affix the gear mechanism to the CB holder; ⑧ a pivot screw to constrain the motion of CB within CBH.

the coaxial cables and the green control rod that extends through the top plate. The basic functioning of this mechanism is as follows: CB is held in CBH by two pins that allow it to pivot about the pins' common axis. The coaxial cables are arranged to provide a torque that tends to rotate the top of CB towards one side of CBH. The gear mechanism controls a counter torque that allows precise orientation of CB and its embedded resonator. Figure 4.3 demonstrates the operation of the mechanism. The angle between CB's surface and the axis of CBH is precisely controlled by twisting the control rod. In the remainder of this section, I will provide more detail of each of the components and the mechanism's functioning.

The CB, pictured in detail in Figure 4.4, is meant to hold the resonator chip and connect the resonator to the transmission line. To ensure good electrical connection and mechanical contact between the transmission line and CB, we customized standard SMA launch jacks.

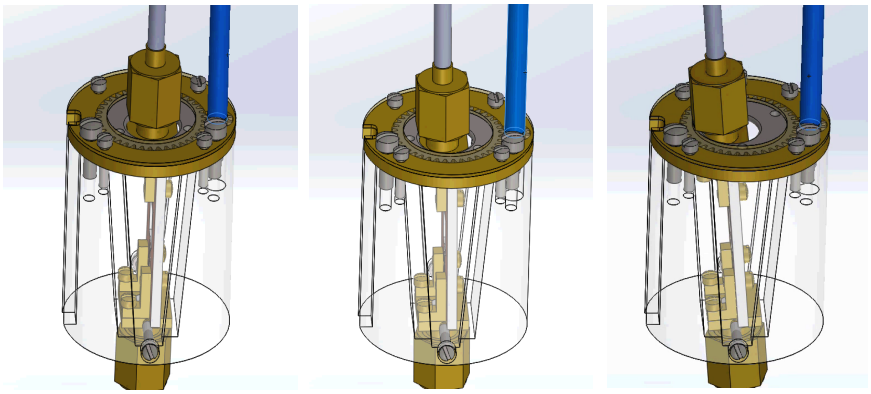

**Figure 4.3.** Rotation of the carriage within the holder. Twisting the control rod (blue) clockwise or counterclockwise will rotate the carriage.

As pictured in Figure 4.4, each brass, nonmagnetic SMA jack is securely attached to the circuit board using two brass L brackets; screws attach each bracket to the outer conductor of the connector and to the ground plane of the copper circuit board. A bit of soft indium is sandwiched between the center pin of each SMA launch and the central conducting strip of CB to ensure good electrical contact.

The CB carriage sits inside the CBH, which is made of ABS plastic by 3D printing. Its outer diameter is such that it fits snugly inside the sample space at room temperature, although it contracts slightly at low temperature. The tight fit ensures that the force applied on the CBH during the manipulation of the CB orientation won't cause its movement. CB nestles in the holder's central cavity, which is shaped in the form of a cutout wedge to allow CB to pivot about its lower end (Figure 4.3). The lower SMA connector of CB has two blind holes into which pins affixed to CBH are inserted, providing a single degree of freedom for the rotation of CB. The upper SMA connector of the carriage protrudes through the gear mechanism on the top of the holder body. Additionally, a notch is cut along the outside length of one side of the holder so that the transmission line can pass by.

The transmission lines are composed of four sections: Two straight sections extend from the chamber top plate to about 10 cm above CBH and the other two sections, one

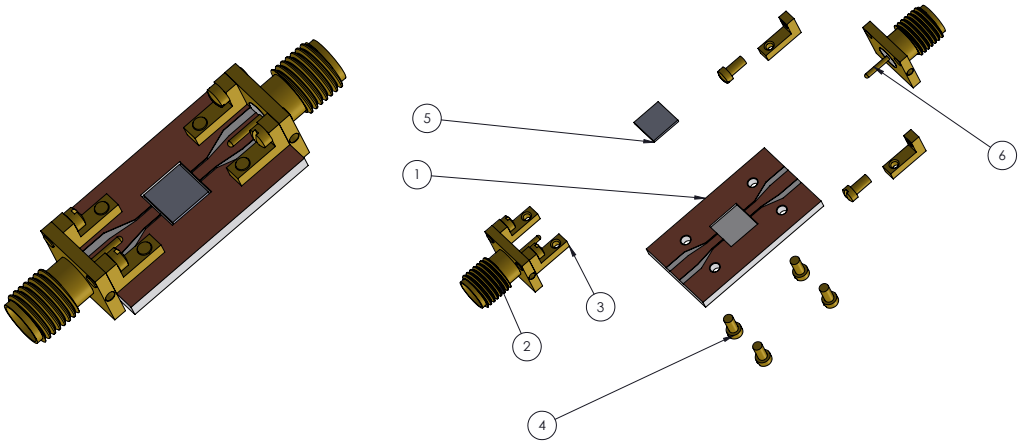


**Figure 4.4.** CAD drawing of CB, assembled and exploded views.. Two modified brass SMA connectors are affixed by brass brackets. The superconducting coplanar waveguide resonator is located in the center of the circuit board. ① the circuit board (copper clad ceramic, Rogers Corp., R04350B), drilled to accept the bracket connectors; ② the modified brass SMA connector; ③ the brass bracket used to affix the SMA connector to the CB; ④ the brass screw used to connect the circuit board to the bracket; ⑤ the superconducting (niobium) thin-film resonator; ⑥ the central conducting pin of the SMA connector, which rests on top of CB's central conducting strip (a small piece of indium metal is held between the two for electrical contact).

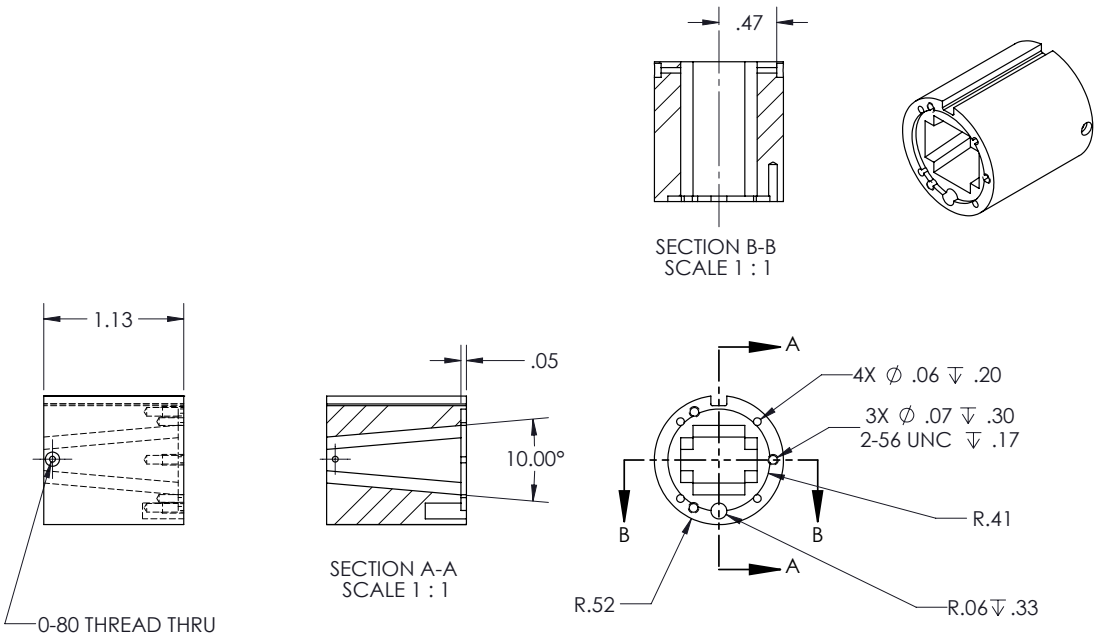


**Figure 4.5.** Technical drawings of CBH. The piece was fabricated using a 3D printer. The tapered slot allows CB to pitch through a range of angles.

straight and one hooked, as shown in Figure 4.2, link the upper lines to CB. The shape of the loop in the lower cable is such that, when CB is integrated into the apparatus, the circuit board leans towards the outer coaxial cable (the one passing through the notch in CBH). The cable thus provides the necessary restoring torque for the carriage that opposes the active torque applied by the gear mechanism. This way the gear mechanism only needs to apply torque in one direction to have the CB carriage rotate both clockwise and counter clockwise from vertical.

The gear mechanism functions, as noted above, to pull the top of CB away from the outer coaxial cable. To achieve this, we designed a central gear that sits in a cartridge on the top of CBH (Figure 4.6). The gear contains an off-center aperture through which the upper SMA connector of CB passes. The edge of the aperture is in contact with the top SMA jack and, as the gear rotates, it causes CB to pivot about the pins inserted into the lower SMA jack. The central gear is driven by a smaller drive gear. The gear ratio of 4:1 allows precise manipulation of the CB angle. The gears are encased within a two-piece

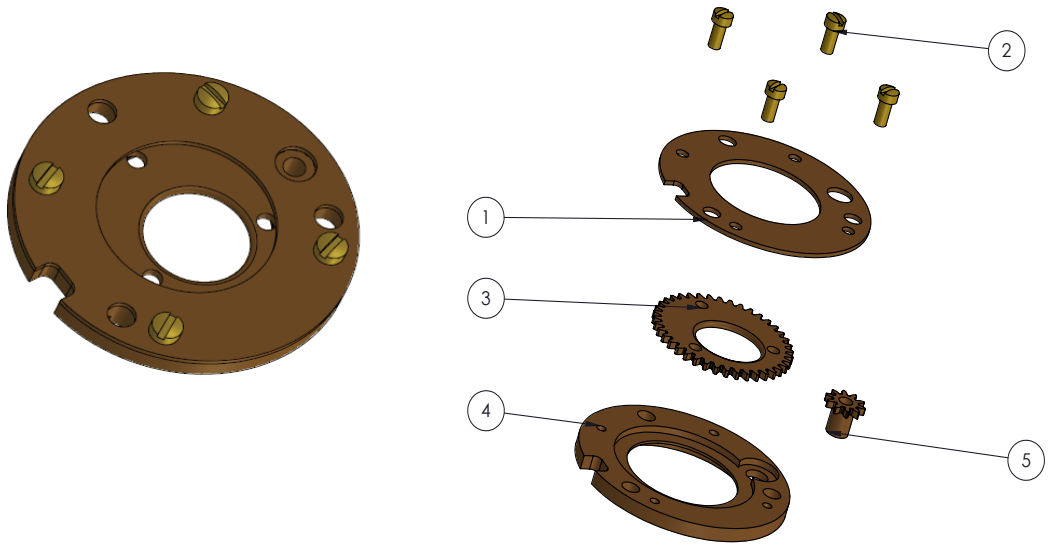


**Figure 4.6.** CAD drawing of the gear mechanism. The top SMA connector of CB passes through the central hole of the gearing mechanism, which is affixed to the top of CBH. The gears can be rotated with respect to the outer casing via a control rod threaded into the small gear (hole opposite the notch). Since the rotating central gear forces the aperture to move relative to CBH – and thus relative to CB's pivot axis – CB's pitch will adjust in a smooth and reproducible manner. ① the top gear cover plate; ② brass screw that holds the top gear cover plate to the gear cartridge (0-80 x .125"); ③ central ring gear that contains the aperture; ④ containing-gear cartridge; ⑤ the drive gear that threads onto the control rod and interfaces with the central ring gear.

cartridge. Each piece of the gear mechanism is machined out of phosphor bronze using a CNC milling machine. The surfaces of the gears are lubricated with Teflon spray to minimize friction.

A drive shaft made from a G10 phenolic rod extends from the gear mechanism up and through the sample chamber top plate, where it terminates in a knob to allow manipulation by the experimenter. The drive shaft needs to be disconnected from and reconnected to the gear mechanism between experiments. So the center of the drive gear is threaded, as is the end of the drive shaft such that the drive shaft can then easily be screwed into the gear. To allow both clockwise and counterclockwise rotation of the drive gear without

unscrewing the drive shaft, vacuum grease is applied to the threads: at low temperatures the grease vitrifies, effectively gluing the shaft to the gear. The drive shaft passes through the top plate via a custom hermetic bulkhead connector that permits the rod to rotate without compromising vacuum.

## 4.3 Results and Discussion

The frequency-dependent transmitted power near the fundamental mode of a resonator is measured at 1.8 K and each spectrum is fit to a Lorentzian to extract the resonance frequency $f_{\text{res}}$ and $Q$. Figure 4.7(a)-(c) shows the dependence of $f_{\text{res}}$ on the applied field $H$ for three different tilting angles ($\alpha = 5^\circ$, $\lesssim 1^\circ$, $\sim 0^\circ$, respectively) of the CB plane to the field direction, controlled by the mechanism described above. (Note that each panel has different scales – as $H$ increases, the resonance peak becomes suppressed and fitting of the peak eventually becomes unreliable. The maximum value of $H$ that allows for a reliable fit decreases as $\alpha$ increases.) For $\alpha = 5^\circ$ (Figure 4.7(a)), $f_{\text{res}}$ drops suddenly as the field is swept up to $\sim 50$ Oe, which indicates a significant flux-trapping effect. When the field is reduced back from $2$ kOe to $0$, the curve shows a strong hysteretic behavior and the original $f_{\text{res}}$ is not restored at $H = 0$. The flux trapping issue is essentially resolved after the chip has been carefully oriented parallel to the field (Figure 4.7(c)). The resonance frequency follows a smooth curve as the field is ramped up and persists up to a field of $0.22$ T. Almost no hysteresis is observed when the field is swept back and $f_{\text{res}}$ recovers its initial value at $B = 0$, evidence that almost no flux is trapped during the sweep cycle. We found that tilting the chip slightly off the vertical orientation ($\alpha \lesssim 1^\circ$) (Figure 4.7(b)) will degrade the resonance curve, indicating that flux trapping is very sensitive to the chip orientation and that accurate control is paramount for the reproducibility of the field dependence of $f_{\text{res}}$.

Similar conclusions are obtained from the dependence of $1/Q$ on magnetic field. Figure 4.7 (d)-(f) show this dependence for the same angles as in Figs. 4.7(a)-(c), respectively.

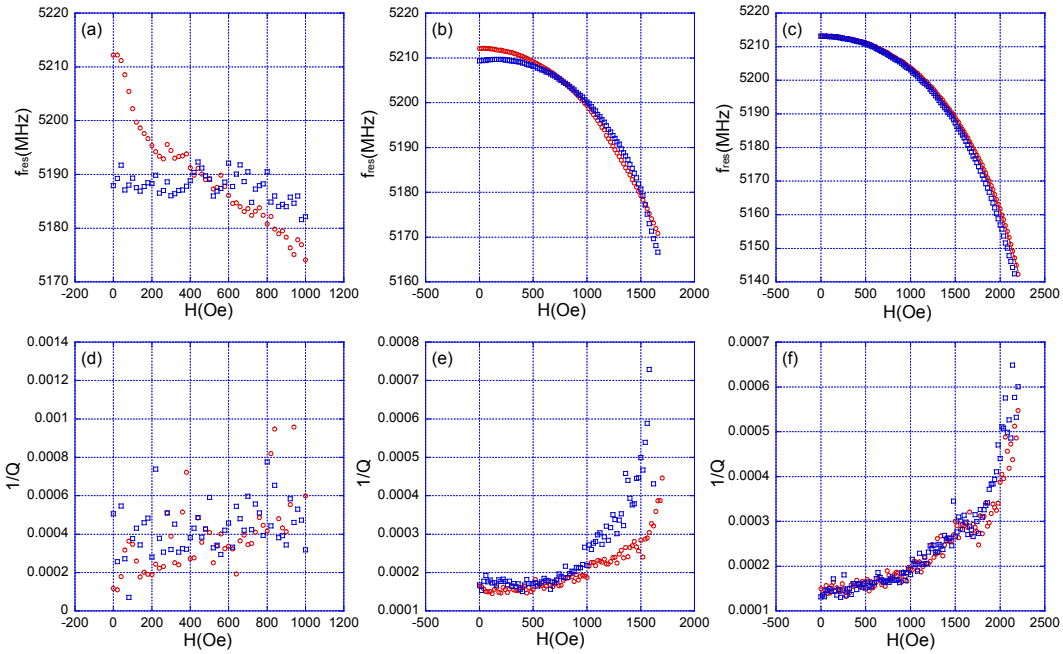


**Figure 4.7.** Resonance frequency and $1/Q$ as a function of magnetic field as the field is swept up (red) and down (blue) for three different CB orientations (a) $\alpha \sim 5°$, (b) $\alpha \lesssim 1°$, and (c) $\alpha \sim 0°$ and between resonator plane and applied field. The up sweep curve in (c) is fit to a model that incorporates the effect of the field dependence of the kinetic inductance. (d)-(f) show $1/Q$ as a function of field for the same orientations as in (a)-(c), respectively.

For good alignment (Figure 4.7(f)), the dependence is smooth with a minimal amount of hysteresis while for larger tilts (Figs. 4.7(d) and (e)), the behavior is degraded.

The data in Figure 4.7(c) (in the absence of flux trapping) can be understood using standard BCS theory in terms of a field-dependent kinetic inductance of the resonator $L_k$. The resonator can be modeled as an LC circuit with $f_{\text{res}} = \frac{1}{\sqrt{LC}}$, where $C$ is the resonator's distributed capacitance and $L$ is the sum of the field-independent geometric inductance $L_m$ and $L_k$ [71]. $L_k$ is associated with the magnetic field by [54]:

$$L_k(H) = \frac{L_k(0)}{\sqrt{1 - \frac{H^2}{H_{c||}{}^2}}}. \tag{4.4}$$

We fit the up-sweep data (red) in Figure 4.7(c) to $f_{\text{res}} = \frac{1}{\sqrt{(L_m + L_k(H))C}}$. The fit is quite good, being difficult to distinguish from the actual data. The fit yields a ratio $\frac{L_k(0)}{L_m} = .04$

and a critical field $H_{c||} = 3465$ Oe. Since $H_{c||} = 2\sqrt{6}\frac{H_c\lambda}{d}$, we determined that the zero-field effective penetration depth to be $\lambda = 35$ nm, using $H_c = 1980$ Oe for niobium and $d = 100$ nm for the thickness of the Nb film in our resonator. This compares well with the bulk value of the London penetration depth, $\lambda_L = 32$ nm, indicating that the superconducting film is of high quality.

Aligning the film of the resonator with the magnetic field *in situ* is challenging not only because the small inner diameter of the PPMS chamber limits the working space but also because of the extreme sensitivity of the resonator to an out-of-plane field component. The apparatus that we developed provides a reliable way of tuning the orientation of the resonator so that ESR experiments can be performed in fields up to $\sim 2$ kOe without trapping flux in the superconducting film. The upper limit of field appears to be a limitation imposed by the thickness of the Nb film used in the fabrication of the resonators and not of the apparatus. Using resonators made with thinner films, we would expect to be able to do reliable experiments at fields as high as $\sim 10$ kOe [66].

## 4.4 Conclusion

The goal of this project was to observe the magnetization tunneling of $Ni_4$ through ESR experiments. However the poor performance of the superconducting resonator hindered the process. We identified the issue to be magnetic flux trapping due to the perpendicular component of the static field that penetrates into the surface of the resonator. To align the resonator to be parallel to the field, we developed a gear mechanism that offers a precision of $\sim 0.2^\circ$. Despite the reliable characterization of the resonator, we have yet to observe signals from the sample. We have excluded some possible explanations such as the poor resonator performance and the degrading of the sample crystal. One possible reason is that when mounting the crystal sample, the surface of the crystal is not attaching tightly to the resonator surface. The strength of the microwave field decreases dramatically away from the surface such that only spins within a few microns of the surface see an appreciable field

from the transmission line [60]. To address this issue, grease should be avoided as a means of affixing the sample and a direct attachment of the sample to the surface should be used to guarantee a close contact.

# CHAPTER 5

# TUNNELING-ASSISTED FORBIDDEN TRANSITIONS OBSERVED IN A PERPENDICULAR-MODE ESR EXPERIMENT

## 5.1 Background

Using the anticrossing of energy states to mitigate the decoherence effect of environmental field fluctuations on a qubit has been proposed and implemented in various qubit systems [36, 37]. As has been discussed in Chapter 2, the off-diagonal elements in the Hamiltonian lift the degeneracy of the energy states. The energy levels at the anti-crossing are insensitive to the variation of the magnetic field to first order. Forbidden transitions, which occur between the superposition states can be implemented to create a robust qubit that is immune to environmental field noise. This strategy to extend the coherence time of qubits has been widely studied in ion-trap qubits [72, 73], silicon-based spin qubits [36], superconducting qubits [9], and recently an SMM qubit — the molecule $[Na^+]_9[Ho^{III}(W_5O_{18})_2]^{9-}$ studied in Steve Hill's group exhibits a coherence time as high as 8 μs when operating at the anti-crossing point [37]. The study of the forbidden transition in $Ni_4$ was first carried out by del Barco et al, where a large transverse field (2.4 T $\sim$ 3.6 T) is applied to create a large tunnel splitting between ground states near zero longitudinal field [44]. The energy splitting is immune to the variations of the longitudinal field to the first order. However it's questionable whether it will be affected by the transverse field. At low transverse fields, where the field acts as a perturbation, it's effect on the energy splitting is negligible. If the transverse field is large enough to totally suppress the anisotropy barrier, the system will enter the Zeeman regime, where the energy splitting will linearly depend on the transverse field. Quantitative analysis in this chapter shows that the high transverse field

applied in del Barco et al.'s experiment goes beyond the perturbation approximation and the tunnel splitting is still susceptible to the component of the environment field in the hard plane of the crystal. In contrast, we observed forbidden transitions in $Ni_4$ molecule at very low transverse fields. These transitions are dominated by the SMM's intrinsic anisotropy so that the transverse field acts as a small perturbation and its effect on the tunnel splitting is greatly reduced. The work presented in this chapter has been published in a recent Physics Review Letter [74] .

## 5.2 Measurement Results

### 5.2.1 Dispersive and absorption spectra

Figure 5.1 shows the dispersive and absorption spectra respectively taken at 1.8 K with the easy axis of the crystal tilted with an angle $\theta_H = 26.6^\circ$ to the $H$ field. Every point in the figure is derived with the method described in section 3.2.3. The absorption spectrum shows the quality factor of the cavity $Q$ as a function of magnetic field $H$. Here $\theta_H$ is deduced from simulations, as will be described below. When the field-dependent energy difference of the states matches the resonance frequency of the cavity, the sample is coupled to the resonator causing a reduction in resonator $Q$, which is manifested as a peak in the ESR absorption spectrum. In this figure, we observe multiple resonance peaks, including two large peaks (red arrows) that are each split. The splitting may be explained in terms of a weak static disorder associated with the dmb ligand that sets in below 46 K [47]. Lawrence et al. found that the heat capacity of $Ni_4$ shows a peak at this temperature and a similar temperature dependence with the diamagnetic Zn analog (Figure 5.2 (a)). This suggests that the peak is due to a structural change instead of an intermolecular magnetic-exchange interaction. Single-crystal X-ray diffraction data for $Ni_4$ at 12 K and 173 K collected in that study was used to generate a thermal-ellipsoid plot (Figure 5.2 (b)). That the thermal ellipsoids shrink at 12 K for all the atoms except for those in the t-butyl group suggests the

existence of two conformational states at low temperature. These two states have slightly different anisotropy parameters, which leads to the splitting of the peaks.

In addition to the large, split peaks, we see small peaks on the right shoulders of the large peaks. This suggests the transitions associated with these peaks have a very small matrix element, so that these transitions could be normally forbidden. Since all these peaks show up at the lowest measurement temperature (1.8 K), we can deduce that they are due to the transitions initiating from low-lying energy levels. Any transitions associated with high energy levels can be excluded from the identification of these peaks.

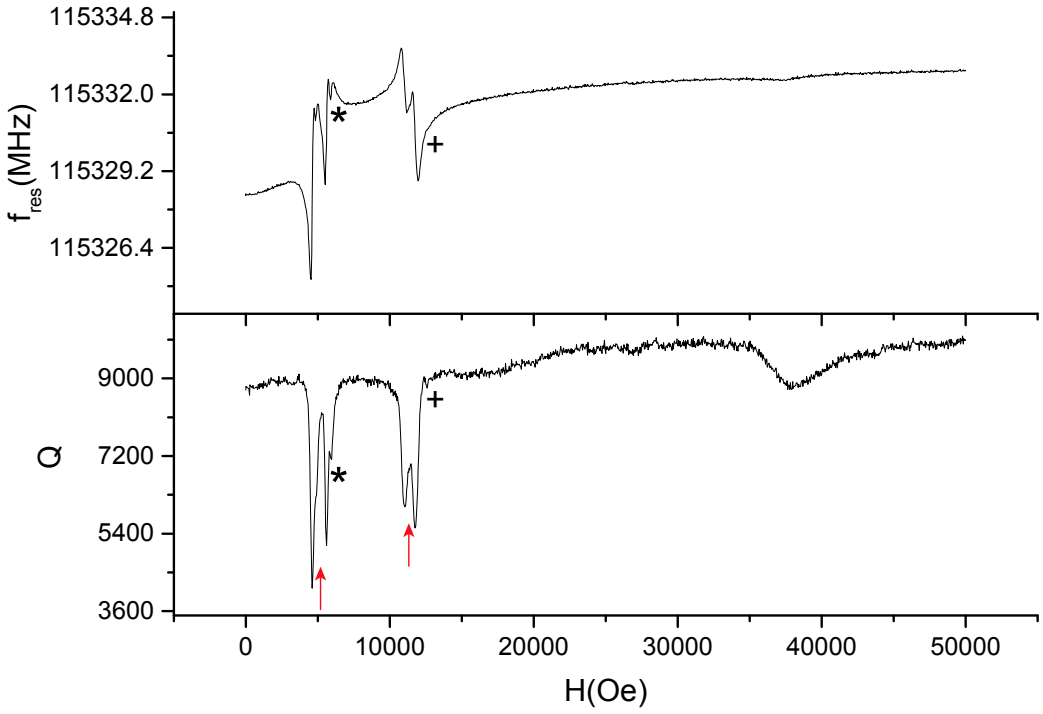


**Figure 5.1.** The frequency and $Q$ value of the cavity as a function of the applied field $H$. The bump at $\sim$ 40 kOe is an artifact that is present for all the spectra. The spectrum was measured with $\theta_H$ = 26.6° at 1.8 K.

The dispersive spectrum in Figure 5.1 gives us similar information about sample-cavity resonance fields. As expected, a sample resonance in this spectrum is characterized by an up-down swing in $f_{res}$, centered on the resonance field. Each peak in an absorption

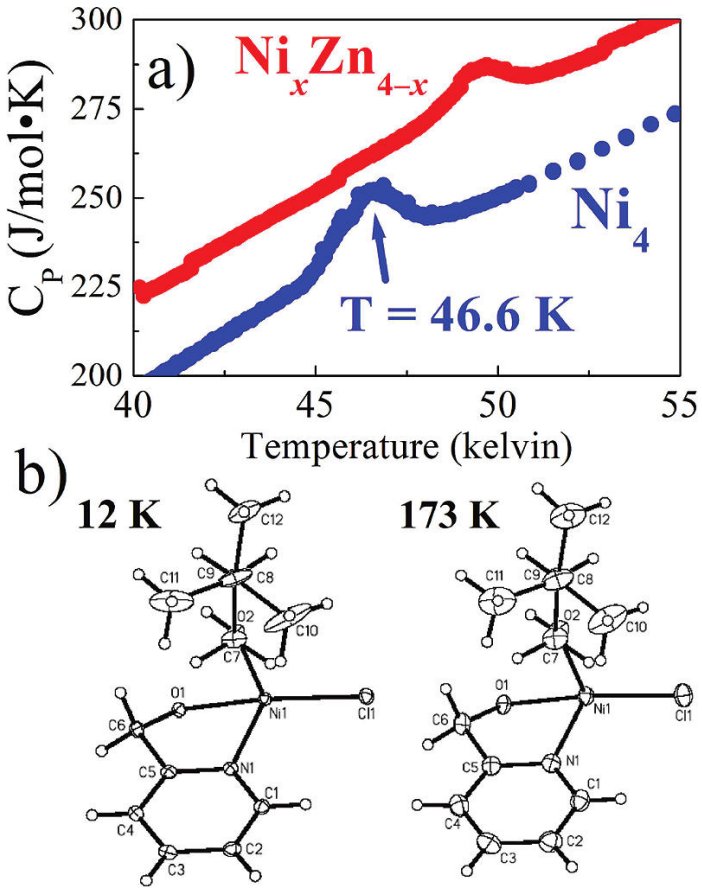


**Figure 5.2.** (a) Heat capacity at constant pressure (CP) versus temperature for [Ni(hmp)(t-BuEtOH)Cl]$_4$ (blue data) and the Ni doped Zn analog (red data) (b) The thermal ellipsoid plot comparison of symmetry independent parts of the molecule of [Ni(hmp)(t-BuEtOH)Cl]$_4$ at 12 and 173 K. (This figure is reproduced with permission from [47]. Copyright 2008 American Chemical Society).

spectrum corresponds to an up-down swing in the associated dispersive spectrum. In this example, one can discern five ESR transitions (in order of increasing field): two allowed transitions, followed by a small forbidden transition, then two more allowed transitions.

One interesting feature that can be discerned only in the dispersive spectrum is the sign of the $f_{res}$ dependence on field: most ESR transitions show $f_{res}$ first increase as the field is increased and then rapidly decrease when the field passes through the sample resonance field. This is a result of the Zeeman effect causing levels to move apart as the field is increased. The resonances in Figure 5.1 at $\sim$13 kOe show this typical behavior. In contrast,

the resonances in Figure 5.1 at ∼5 kOe have the opposite dispersive behavior, with $f_{res}$ first decreasing with $H$ and then rapidly increasing when resonance is reached. This unusual behavior indicates that the two levels involved in these transitions are in fact moving closer to each other as field increases. The left black arrow in Figure 5.3 shows the transition corresponds to levels exhibiting just that behavior.

Considering that all of these transitions are low-level transitions, we can deduce that the split peaks at $\sim$ 5 kOe are due to $-4 \rightarrow -3$ allowed transition and the split peaks at ∼13 kOe are due to $3 \rightarrow 2$ allowed transition (black arrows in Figure 5.3). As will be discussed below, a detailed study of the angular dependence of the spectra indicates that the small peaks have different dependence on the field and can be attributed to forbidden transitions from a state with well defined $m$ to a state that is a superposition of $m$ states.

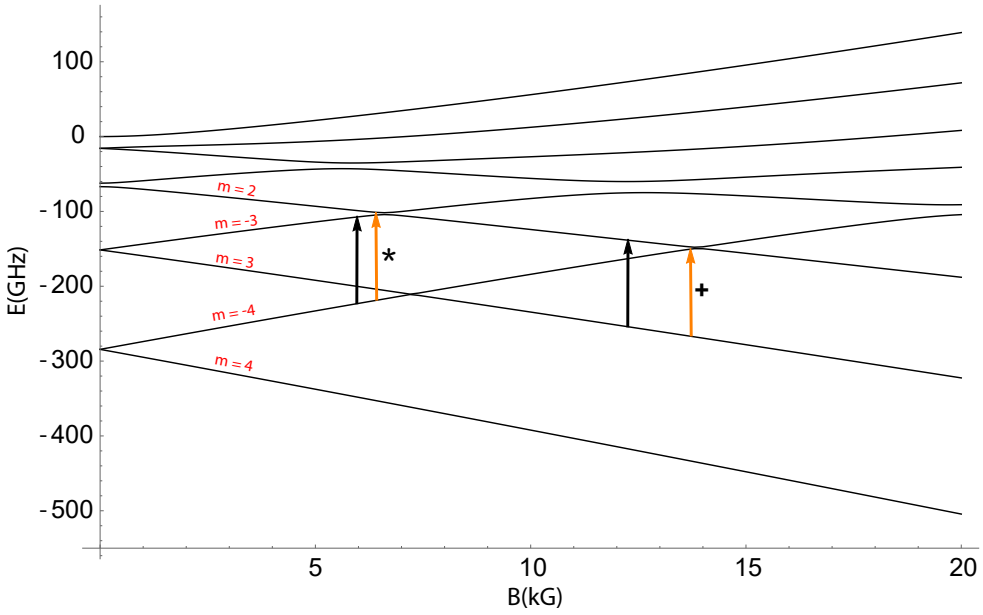


**Figure 5.3.** Spin-state energy-level diagram for $Ni_4$. Energies of various levels are shown as a function of magnetic field, calculated by diagonalizing the molecule's spin Hamiltonian. The diagram illustrates the levels' behavior when $\theta = 30°$. Arrows indicate the major transitions observed in this study. Black (orange) indicates allowed (forbidden) transitions. The two orange arrows are labeled with $\star$ and $+$.

### 5.2.2 Temperature dependence

Figure 5.4 shows the absorption spectrum for $\theta_H = 26.6^\circ$ at different temperatures ranging from 1.8 K to 9 K. Each curve is vertically spaced evenly for clarity. As expected, absorption peaks associated with higher energy levels start to show up as temperature increases. This happens because the higher energy levels get populated as temperature increases, leading to the increase in the amplitude of the peaks. The second finding is that the width of the peaks increases with temperature by a factor of roughly 3 from 1.8 K to 9 K, which indicates a decrease of $T_2$ at high temperature. This may correspond to a reduced lifetime of the excited states due to higher acoustic-phonon populations at higher temperature. Alternatively, larger dipole and hyperfine field fluctuations at increased temperature may promote decoherence since typically the Zeeman effect causes the states' energies to vary linearly with field. Lastly, we observe a shifting of the resonance peak position to higher fields as temperature increases. We attribute this to the dipolar field introduced by the neighboring spins. Each $Ni_4$ molecule sees not only the applied field, but the total field including the net dipolar field from all of its neighbors: $\vec{B} = \vec{H} + 4\pi\alpha\vec{M}$. Here, $\alpha$ is a parameter on the order of unity that takes into account lattice-structure and crystal-shape demagnetization effects and is treated as a free parameter. Since the magnitude and orientation of the magnetization is temperature dependent, the magnetic induction $\vec{B}$ (both magnitude and direction) is also temperature dependent. This issue will be addressed in the following section; it is concluded that dipolar interactions are significant in the system and this effect needs to be accounted for in the simulations.

### 5.2.3 Angle dependence

Figure 5.5 shows ESR spectra ($Q$ vs. $H$) at 1.8 K for multiple values of $\theta_H$, as indicated. The value of the angles are obtained through fitting each spectrum, as will be discussed later. For many values of $\theta_H$ (e.g. 32.0°), we observed large peaks accompanied with the small peaks that are on the left or right of the large peaks (marked as $\star$ and $+$ in the figure

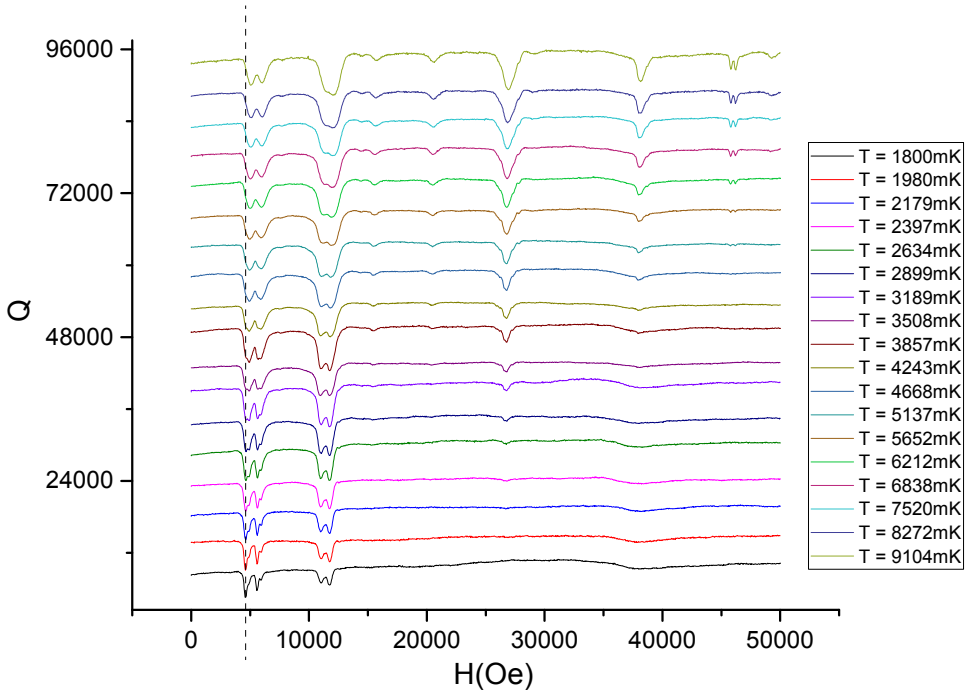


**Figure 5.4.** ESR spectra at $26.6°$ at different temperatures. The plot at 1.8 K shows the exact value of $Q$. All the other plots are shifted vertically for clarity. The dashed line is aligned with an allowed peak at 1.8K and serves to show the shifting of the peak with temperature.

). At some angles, the small peaks are not significant and can barely be seen. As $\theta_H$ increases, all the peaks shift to higher fields. The small peaks have different dependance on $\theta_H$ than their neighboring large peaks: The peak denoted by $\star$ moves faster than its neighboring peak, while the peak denoted by $+$ moves slower than its neighboring peak. The different $\theta_H$ dependences of the small peaks and large peaks confirmed the different nature of these transitions. By examining the energy-level diagram, these small peaks are attributed to inter-well transitions ($-4 \rightarrow 2$ and $3 \rightarrow -4$ ), which are normally forbidden (Figure 5.3). The general shifting of all peaks is due to the Zeeman splitting, which is roughly proportional to $B_{\|} = B\cos\theta$. As $\theta_H$ increases, a higher field is needed to attain

resonance. Increasing of $\theta_H$ also introduces a larger transverse $H$ field. This causes more mixing of energy levels that will lead to an increase of the intensity of the transition peaks.

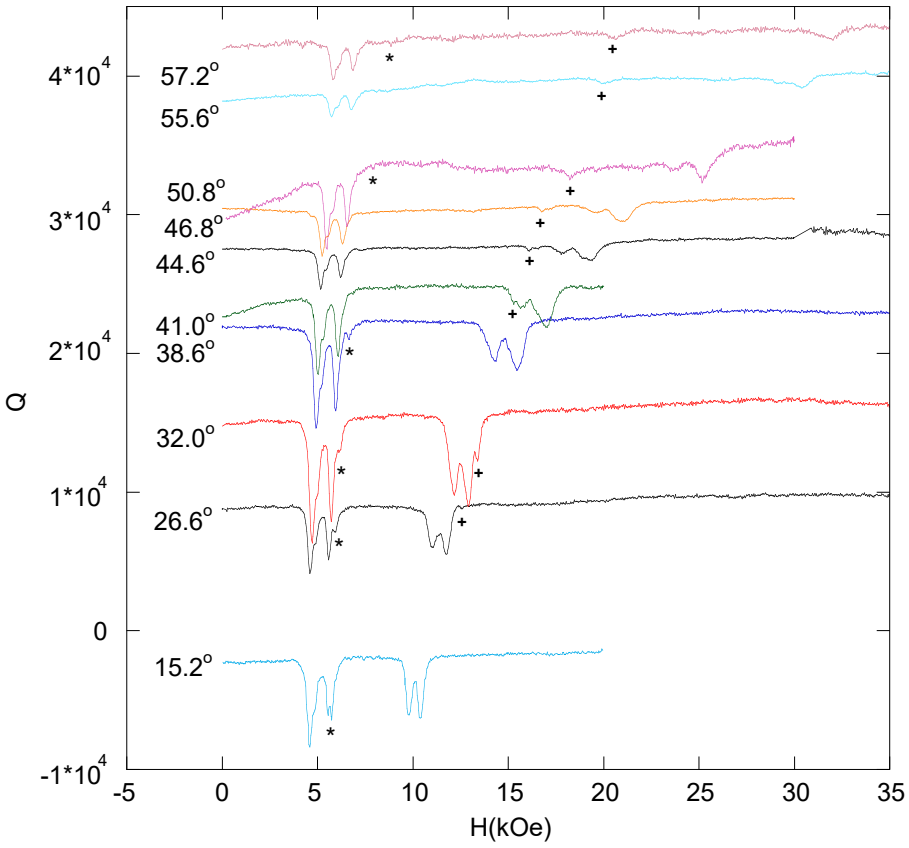


**Figure 5.5.** ESR spectra at 1.8 K for several angles $\theta_H$, the angle between the crystal easy axis and the applied field $\vec{H}$. Spectra were obtained by measuring the cavity-sample resonance to determine resonant frequency and quality factor $Q$. In this figure, $Q$ is plotted as a function of $H$. The spectrum for $\theta_{H,ref} = 26.6°$ shows actual $Q$ values. All other spectra were shifted vertically by an amount proportional to $\theta_H - \theta_{H,ref}$. Spectra from three different crystals are combined in this figure. Each spectrum has been shifted slightly horizontally to account for inductive effects due to sweeping $H$.

Let's summarize the results presented so far: (1) Dispersive and absorption spectra are presented. By studying the resonance 'swing' in the dispersive spectrum and with the knowledge of the Hamiltonian parameters previously reported, we attributed the two large split peaks to the intra-well allowed transitions $-4 \rightarrow -3$ and $3 \rightarrow 2$. (2) The temperature study demonstrated an increase of $T_2$ with temperature. The shifting of the resonance peaks

indicates a dipolar-field effect that we need to address in our fitting procedure. (3) The angular study gives us some clues on the nature of the potential forbidden transitions and their dependence on the angle. In the next section, I will discuss in detail about the fitting strategy we applied to these spectra to determine the parameters of the Hamiltonian, the tilting angles of the magnetic field ($\theta_H$) and the dipolar factor ($\alpha$). With these parameters known, more discussion on the nature of the observed transitions will be presented.

## 5.3 Simulation and analysis

### 5.3.1 Fitting of Spectral Peaks

We use the EasySpin package in MATLAB to reproduce the spectra at various $H$ orientations and temperatures. EasySpin is a MATLAB toolbox for simulating and fitting a wide range of ESR spectra [75]. The MATLAB scripts used for fitting can be found in Appendix B. Several fitting parameters need to be determined to simulate the spectrum:

1. The anisotropy parameters

   The typical Hamiltonian for $Ni_4$ (Eqn. 2.1) is up to fourth order in spin operators. We observed the splitting of the absorption peaks of the allowed transitions (Figure 5.1), which indicates the presence of two conformational states of $Ni_4$ in the crystal. Thus, two sets of anisotropy parameters are needed to account for the two components in the crystal.

2. The g factors

   The g-tensor is diagonal in the principal-axes basis:

$$\begin{bmatrix} \mathbf{g}_x & 0 & 0 \\ 0 & \mathbf{g_y} & 0 \\ 0 & 0 & \mathbf{g_z} \end{bmatrix}$$

The four-fold symmetry of the molecule in the x-y plane implies $g_x = g_y$, which leaves only two fitting degrees of freedom — $g_x$ and $g_z$.

3. The dipolar effect constant $\alpha$

   This determines the strength of the interaction of the dipolar fields with the molecule (see the discussion of Eqn. 5.1).

4. $\theta_H$ and $\phi_H$

   $\theta_H$ and $\phi_H$ define the orientation of the crystal with respect to the magnetic field within the cavity. The definition of these angles can be found in section 3.2.2.

There are also many factors that affect the accuracy of the fitting. The following factors that come from either the instrument or the $Ni_4$ crystal itself must be considered:

*1. Induced magnetic field*

When taking our spectra, the magnetic field $H$ is swept at a constant rate of 150 Oe/s. Since our sample chamber and cavity are metallic (mostly copper), the changing field produces an induced magnetic field that opposes $dH/dt$ (Lenz' law). Therefore, the actual H-field applied to the sample is less than the nominal value determined by the current in the magnet coils. To characterize this offset, we took a reference spectrum by sweeping $H$ from -20 kOe to 20 kOe (Figure 5.6). One can see that the spectrum is not symmetric about $H = 0$, indicating the effect of the induced field. By determining the symmetry point for the spectrum, we find the inductive field offset to be $H_{off}$ = 301 Oe. All the spectra need to be corrected from the raw data by shifting the spectra horizontally to lower $H$ by $H_{off}$.

*2. Impact from the dipolar fields*

Because our ESR spectra are obtained at low applied field and at substantial angles $\theta_H$ between the sample's easy (z) axis and applied field $\vec{H}$, the field experienced by a typical molecule, $\vec{B}$, is not collinear with $\vec{H}$. Thus, it is important to carefully transform $\vec{H}$ into $\vec{B}$ in performing our analysis and simulations.

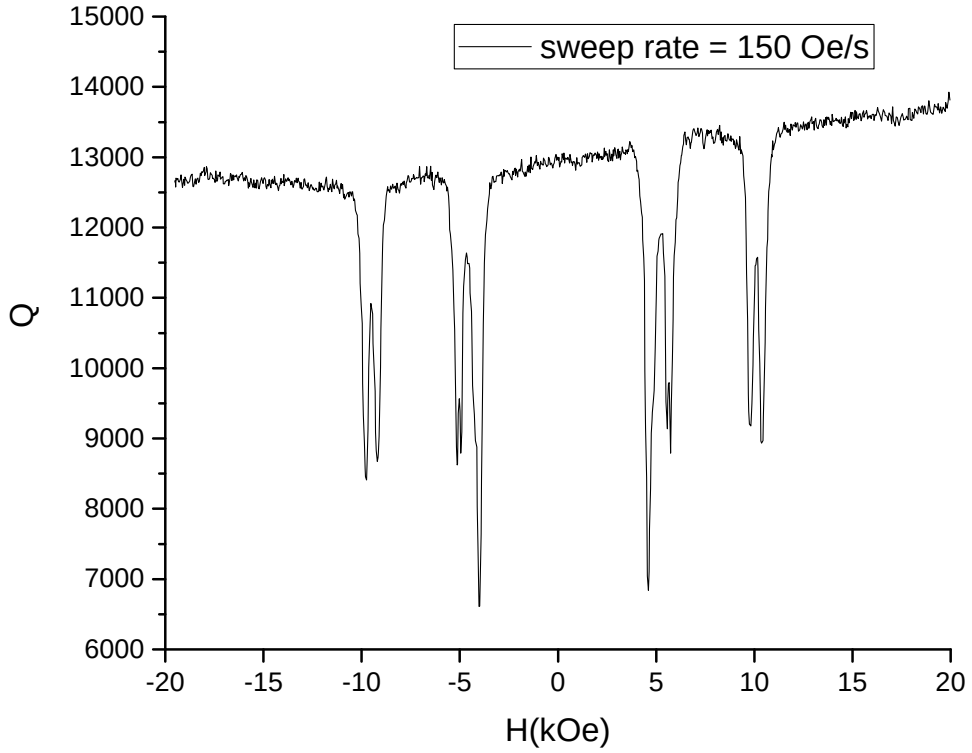


**Figure 5.6.** ESR spectrum for $\theta_H = 15.2°$ with $H$ swept from -20 kOe to 20 kOe.

While for any given spectrum, $\theta_H$ and $\phi_H$ is constant as the field is swept, the angle $\theta$ between $\vec{B}$ and the easy axis is changing as $H$ increases because of the spin's anisotropy. To account for this, we diagonalized the Hamiltonian with $\vec{B}$ along the x, y, and z directions. For each direction, we calculate the magnetization $M_i$ ($i = x, y, z$) as a function of $B_i$ and temperature $T$ using standard statistical mechanical techniques: The discrete magnetic energy levels were first obtained by diagonalizing the Hamiltonian at $B_i$. The probability $P_k$ ($k$ = 1,2,...,9) for the system to be found on the $k$th energy level at temperature $T$ follows Boltzmann statistics ($P_k = \frac{\exp(-E_k/k_BT)}{\sum_{1\leq j\leq 9}\exp(-E_j/k_BT)}$). The expectation value of $S_i$ can be calculated by $\langle S_i\rangle = \sum_k \langle k|\hat{S}_i|k\rangle \cdot P_k$. $M_i$ is then found to be $M_i = \frac{g_i\mu_B\langle S_i\rangle}{2v}$, where $v$ is the unit-cell volume the molecule. The molecule's symmetry implies that the susceptibility tensor is diagonal; this becomes only an approximation as $H$ increases. We then use the

relations

$$H_i = B_i - 4\pi\alpha M_i\left(B_i, T\right), \tag{5.1}$$

where $\alpha$ is a parameter on the order of unity that takes into account lattice-structure and crystal-shape (demagnetization) effects and is treated as a free parameter. For a given crystal orientation, we calculate $H_i$ using:

$$\begin{aligned} H_z &= H\cos\left(\theta_H\right) \\ H_x &= H\sin\left(\theta_H\right)\cos\left(\phi_H\right) \\ H_y &= H\sin\left(\theta_H\right)\sin\left(\phi_H\right), \end{aligned} \tag{5.2}$$

where $\theta_H$, $\phi_H$ are defined in section 3.2.2.. Using Eq. 5.2 and numerically inverting Eq. 5.1, we can calculate $B_i\left(H, \theta_H, \phi_H, T\right)$ and thereby calculate $B = \left|\vec{B}\right|$ and $\theta = \arccos\left(B_z/B\right)$. We could also get $\phi = \arctan(B_y/B_x)$. However, the small hard-plane anisotropy of $Ni_4$ means that the susceptibility is nearly isotropic within the plane, resulting in $\phi$ nearly indistinguishable from $\phi_H$. In simulating our spectra, $B$ and $\theta$ vary as a function of $H$ for fixed $\theta_H$. To account for the dipolar effect, all the $H$ values in the spectra are converted to $B$ values and the resonance-field positions and intensities are obtained from the corrected spectra. As $H$ is swept with a constant angle $\theta_H$, the $B$ field is changing in magnitude and orientation. A spectrum in $\{B, \theta\}$ and $\{H, \theta_H\}$ domains is displayed in Figure 5.7.

*3. Different $\phi_H$ for different sample*

Our data was collected from three different samples. Sample 1 was used for the spectrum labeled $15.2^\circ$ in Figure 5.5; the spectra labeled $26.6^\circ - 38.6^\circ$ were taken from Sample 2; the remaining spectra come from Sample 3. The angle $\phi_H$ was hard to control in mounting the sample. We assume that tilting the sample to change $\theta_H$ had minimal effect on $\phi_H$ for a given sample, so $\phi_{H,i}$ was taken to be constant for each sample $i$.

*4. Orientation of the crystal*

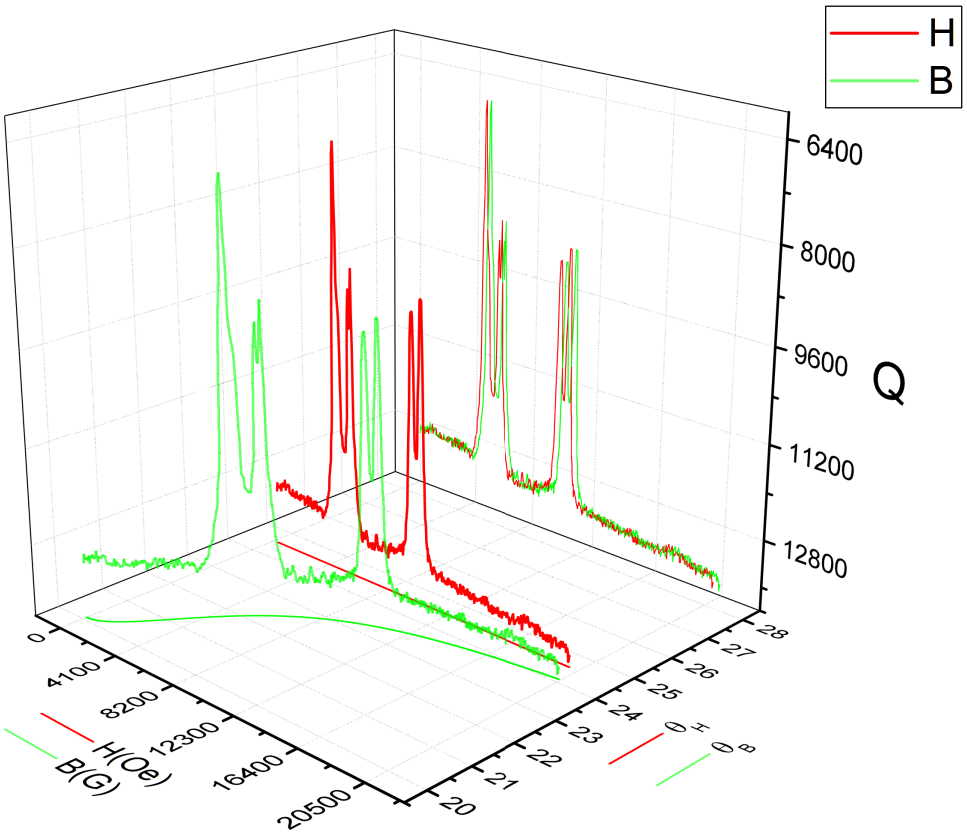


**Figure 5.7.** The measured $Q$ value of the cavity at $\theta_H = 15.2°$ and 1.8 K as a function of the $\{B, \theta\}$ (green) and $\{H, \theta_H\}$ (red).

To simulate ESR spectra, EasySpin needs to know about the relative orientations of the crystal within the laboratory frame. The lab frame is fixed in the laboratory with three unit vectors denoted as $\hat{X}$, $\hat{Y}$, $\hat{Z}$. $\hat{Z}$ is along the static magnetic field and in our case along the axis of the cavity. $\vec{X}$ is along the linearly oscillating microwave magnetic field which is along the radial direction. In our experiment, the crystal is placed in the cavity such that the $z$ axis of the molecule has an angle $\theta_H$ to $\vec{Z}$ and perpendicular to $\vec{X}$ at the same time (Figure 3.5). The three Euler angles describing the orientation of the molecule to the lab frame can be determined by the angles describing three successive rotations of the molecule coordinates $xyz$ initially aligned with the lab frame $XYZ$. By definition, rotations are around z axis, y axis and lastly z axis in the crystal frame ($zyz$ convention). Rotations from

the lab frame to the crystal frame is as follows: rotate xyz clockwise around $\vec{Z}$ by $90^\circ$ to get $\{x', y', z'\}$ , rotate clockwise around $y'$ by $\theta$ degrees to get $\{x'', y'', z''\}$, rotate clockwise around $z''$ by $\phi$ degrees to the final orientation (Figure 5.8). So {-90, -$\theta$, -$\phi$} describes the lab-to-crystal frame rotation where the negative sign indicates a clockwise rotation. Since the orientation definition used in EasySpin needs the crystal-to-lab frame transformation, we just invert the order and sign of the three Euler angles to get the parameter $\{\phi, \theta, 90\}$ that is taken as input for crystal orientation in the simulation.

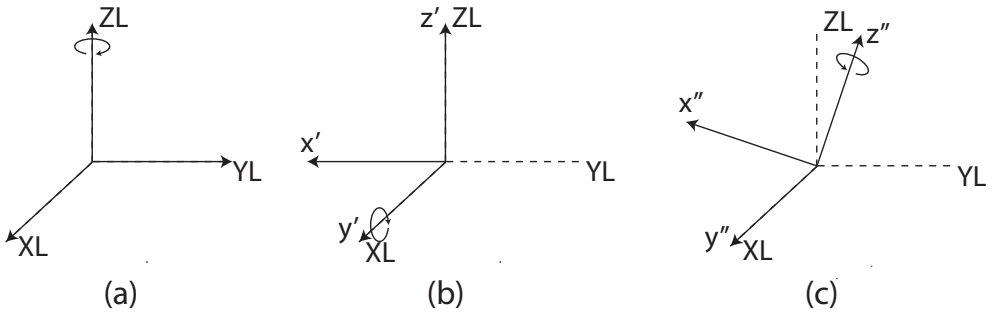


**Figure 5.8.** The procedure that rotates the crystal initially aligned with laboratory coordinates ($\hat{Z}$ points to the static magnetic field direction, $\hat{X}$ points to the oscillating magnetic field direction) to the crystal coordinates. (a),(b),(c) corresponds to the subsequent rotations around $Z$, $y'$, $z''$.

*5. $\vec{B}$ range*

It is very straightforward to simulate the spectrum by using EasySpin. With the sample information (Hamiltonian parameters, etc.) and experimental setup (the crystal orientation, etc.) well defined, the "pepper" function produces the continuous-wave ESR spectrum for a given $B$ range. However, the function requires a constant $\vec{B}$ orientation during the field sweep, which is not the case in our experiment since $\vec{B}$ changes in both magnitude and orientation. To simulate the spectrum with a varying $\theta$, we divided the full B range (typically $0 \sim 3.5$ T) into subranges (n = 20) and assume a constant $\theta$ for each range in the simulation. This constant $\theta$ is set as the average of the $\theta'$s corresponding to the starting

and ending $B$ field of the range. The full range spectrum is obtained by combining all the spectra together.

### 5.3.2 Fitting process

On the real data side, after subtracting the inductive field $H_{off}$ and then converting the $\vec{H}$ field into $\vec{B}$ field for a given value of $\alpha$, it can be compared with the simulated spectrum to do the fitting. The easiest way to fit the spectrum is to compare the spectrum with the simulation directly. However, this is complicated by the fact that the forbidden transitions are typically very small compared with the allowed transitions. Therefore, a least-squares minimization procedure that compares experimental and simulated spectra effectively ignores forbidden-transition peaks for most values of $\theta_H$. Instead, we adopted a different fitting procedure that treats all observed peaks with equal weight. By fitting the experimental spectral peaks to Lorentzian functions, we determined the field position, $B_{data,i}$, and area, $I_{data,i}$, for the $i$th peak. A least-squares fitting method is then applied to determine the anisotropy parameters $D$ and $B$ for both components and $\alpha$, as well as the angles $\theta_H$ and $\phi_H$. The anisotropy parameter $C$ is independently determined by low frequency (5 GHz) ESR experiment of zero field tunnel splitting of $\sim (|m=2\rangle + |m=-2\rangle)$ and $\sim (|m=2\rangle - |m=-2\rangle)$ for each component [76]. The $\chi_i^2$ for each peak is defined as:

$$\chi_i^2(\theta_H, \phi_H) = \left(\frac{B_{sim,i}(\theta_H, \phi_H) - B_{data,i}}{\Delta B_{data,i}}\right)^2 + \left(\frac{I_{sim,i}(\theta_H, \phi_H) - I_{data,i}}{\Delta I_{data,i}}\right)^2, \tag{5.3}$$

where $\Delta B_{data,i}$ and $\Delta I_{data,i}$ are the uncertainties in $B_{data,i}$ and $I_{data,i}$, respectively, as determined from the Lorentzian peak fitting. $B_{sim,i}(\theta_H, \phi_H)$ and $I_{sim,i}(\theta_H, \phi_H)$ are the values determined from simulations of the corresponding peaks for given anisotropy parameters, g, $\alpha$, $\theta_H$ and $\phi_H$. Here we used the "resfield" function in Easyspin to locate the resonance peak and calculate its intensity.

The total $\chi^2$ is calculated by summing over all the peaks from all spectra at temperatures 1.8 K and 9 K, as well as spectra taken at $\sim 5$ GHz both for a sample of $Ni_4$ and a dilute

sample consisting of 5% $Ni_4$ cocrystallized with 95% diamagnetic $Zn_4$.

$$\chi^2_{total} = \sum_i \sum_{\theta_H, \phi_H} \chi^2_i (\theta_H, \phi_H) \tag{5.4}$$

$\chi^2_{total}$ is minimized to obtain the optimal values of anisotropy parameters, g and $\alpha$ as well as all values of $\theta_H$ and $\phi_H$. Anisotropy parameters and $\alpha$ are taken to be the same for all peaks from all spectra except a different $\alpha$ value is assumed for the 5% $Ni_4$ sample. Peaks from the same spectra are forced to have the same value of $\theta_H$. Spectra from the same sample were forced to have the same value of $\phi_H$. For the + forbidden transitions, the peaks from the two components overlapped for many values of $\theta_H$. So, in calculating $\chi^2$ for those peaks, we included the mean position and the total area of the peaks. The resulting fitting parameters are then used to further correct the calculated values of $M_i$ (Eqn. 5.1). The above procedure is then iterated until it has converged.

### 5.3.3 Fitting results

Figure 5.9 shows the $B$ - $\theta$ resonance positions (points, determined from the spectra in Figure 5.5), where $\theta$ is the angle between the easy axis and the field $\vec{B}$ experienced by the molecules. The lines are the simulated result with the fitted parameters given below. Allowed (forbidden) transitions are shown using solid (dashed) curves. The agreement between the simulated resonance fields and the experimental data is very good. The red and black curves in the figure are the predicted resonance positions for the two conformational states of the molecule, which have somewhat different anisotropy constants, determined by fitting: $D = 15.13(4)$ GHz, $B = 0.136(2)$ GHz and $C = 5.3(2)$ MHz (red), and $D = 15.55(4)$ GHz, $B = 0138(2)$ GHz, $C = 6.45(3)$ MHz (black). Both components were taken to have identical $g$ factors, which were found to be $g_z = 2.157(7)$ and $g_x = g_y = 2.220(3)$. These numbers are in good agreement with those found by others [43, 77].

Figure 5.10 shows a comparison of the simulated and experimental spectra at $\theta_H = 26.6^\circ$ at 1.8 K and 9 K respectively. More fitting-comparison figures at different angles

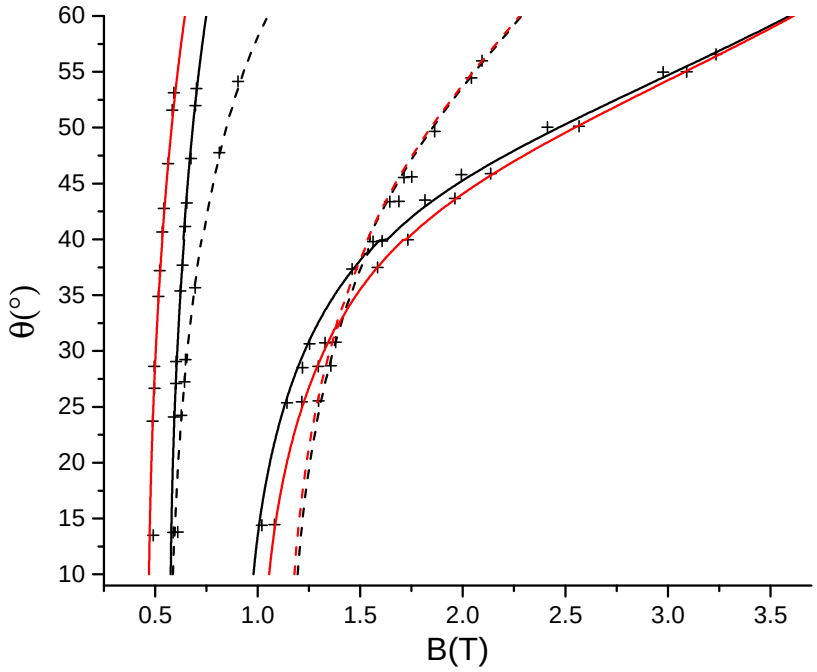


**Figure 5.9.** Resonance positions in $B - \theta$ space. The points are the peak positions from Figure 5.5 after correcting for the effects of dipole fields. The lines are the results of simulations after fitting the observed spectra. Black and red correspond to different conformational states of the molecule with correspondingly different anisotropy constants. Solid curves indicate allowed transitions and dashed curves correspond to forbidden transitions. The small shift seen in the calculated results at $\sim 40^\circ$ arises from use of different samples at angles above and below this value and consequent differences in the direction ($\phi_H$) of the transverse field in the samples' hard planes.

are given in Appendix C. The peak position as well as the peak intensity is faithfully reproduced except for some offsets of the weak peaks (dashed lines in Figure 5.10). These discrepancies cannot be eliminated by adjusting the fitting parameters since they are due to the transitions associated with high-lying energy levels and their positions are weakly affected by the anisotropy. Since our fit depends only on the peak positions and areas, it is insensitive to the peak widths, which we adjusted manually in the simulated spectra through the parameter HStrain in EasySpin to achieve reasonable agreement. We can see in Figure 5.10 that the width at 9 K is roughly a factor of three larger than at 1.8 K.

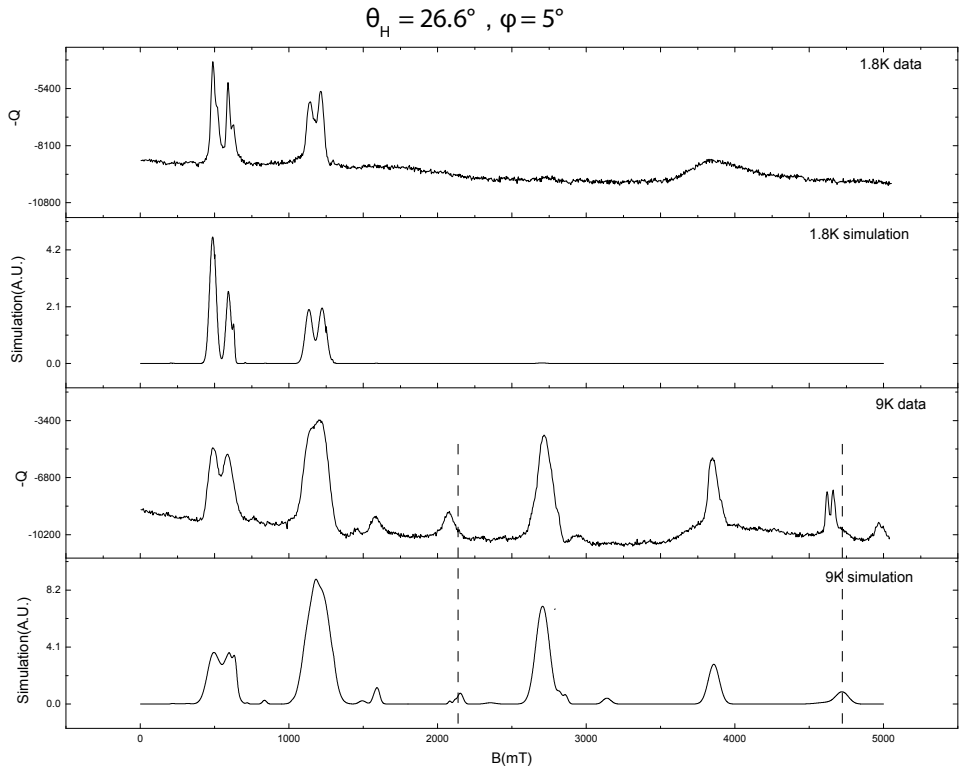


**Figure 5.10.** Comparison of experimental and simulated spectra at 1.8 K and 9 K, as indicated for $\theta_H = 26.6°$, $\phi_H = 5°$.

## 5.4 Discussion

### 5.4.1 Tunneling-assisted forbidden transitions

To understand how tunneling makes the forbidden transitions observable, we note that each forbidden transition (orange arrows in Figure 5.3) occurs at a field near an avoided level crossing, at which resonant tunneling takes place. Tunneling effects can be demonstrated by expanding the two energy eigenstates associated with each forbidden transition in the eigenbasis of $S_z$:

$$|E_i\rangle = \sum_m c_m^{(i)} |m\rangle \tag{5.5}$$

Figures 5.11(a) and 5.11(b) show the values of $c_m^{(i)}$ as a function of $m$ for the two states involved in the $\star$ and $+$ forbidden transitions, respectively, at $\theta = 30°$. For these calculations, the Hamiltonian parameters of the "black" component in Figure 5.9 were used.

For $\star$, the initial state is $|i\rangle \approx |m = -4\rangle$, while the final state $|f\rangle$ is a superposition of primarily $|m = 2\rangle$, $|m = -3\rangle$, and $|m = 1\rangle$. The proximity of the resonant field to the tunneling field is what leads to the small amplitude of $|m = -3\rangle$ in $|f\rangle$, giving rise to a $\Delta m = 1$ transition matrix element between the two energy eigenstates. Thus, the transition between states largely localized in separate wells can be viewed as a tunneling-assisted forbidden transition. Were the photon resonance (orange arrow in Figure 5.3) to occur far away from the avoided crossing, the forbidden transitions would be suppressed. When the photon resonance occurs close to the avoided crossing, the final state gets more mixed and transition becomes "less" forbidden. Equivalently, the forbidden transition can be viewed as tunneling from a single-photon dressed state $|i\rangle \approx |m = -4, n = 1\rangle$ state into the $|f\rangle \approx |m = 2, n = 0\rangle$ state, where $n$ indicates photon number. During this forbidden transition ($\star$), the change of $m$ is nominally 6. A more rigorous calculation to calculate the expectation value $\langle S_z \rangle$ is as follows:

$$\Delta\langle S_z \rangle = \langle f | \hat{S}_z | f \rangle - \langle i | \hat{S}_z | i \rangle \tag{5.6}$$

$\Delta\langle S_z \rangle$ is calculated to be as large as 6, indicating a large change in the spin's angular momentum with the absorption of a single photon. (cf. Figure 5.14)

A similar analysis can be made of the $+$ transition (Figure 5.11(b)), where the transition is associated with $|i\rangle \approx |m = 3\rangle$ and $|f\rangle$, a superposition of mostly the $|m = -4\rangle$, $|m = -3\rangle$, and $|m = 2\rangle$ states. Once again, the transition is enabled by the fact that the resonance field is close to a tunneling field, leading to a small, but appreciable amplitude of the $|m = 2\rangle$ state in $|f\rangle$. The calculation of the change in $\langle S_z \rangle$ indicates a value as high as $\sim 7$ for the values of $\theta$ used in our experiment. (cf. Figure 5.14)

### 5.4.2 Simulation of the forbidden transition intensity

As can be seen in Figure 5.5, the peaks associated with the forbidden transitions are stronger when they are close to the allowed transitions, confirming the delocalization of

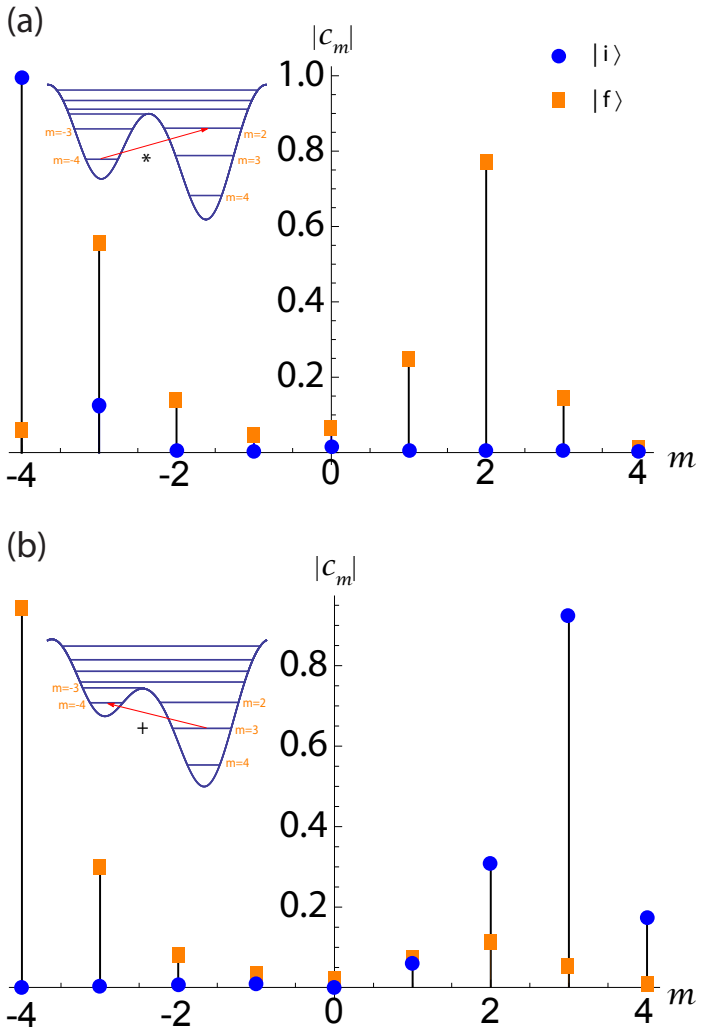


**Figure 5.11.** Decomposition of spin states involved in the forbidden transitions in the $m$ basis (Eqn. 5.5). Values of $c_m$ were calculated by diagonalizing the spin Hamiltonian at the fields corresponding to the (a) $\star$ and (b) $+$ transitions, setting $\theta = 30°$. Blue (orange) indicate the values of $|c_m|$ for the lower (upper) state involved in each transition. Insets schematically show the double-well potentials for the associated transitions, marked with red arrows.

$|f\rangle$ near the tunneling-resonance field. To quantify this observation, we determined the spectral intensity of each peak in each spectrum by measuring the total area of the peak after subtracting background. We compare this with the calculated transition intensity $|\langle f|\, S_T\, |i\rangle|^2 \cdot (P_i - P_f)$, where $S_T = \vec{S} \cdot \hat{B}_{rf}$, and $P_i$ and $P_f$ are the populations of the initial and final states. Each quantity is normalized so that the total intensity for all transitions in a

given spectrum is unity. Figures 5.12(a) and 5.12(b) shows a comparison of the experimental (points) and simulated (curves) spectral intensity of the $\star$ and $+$ forbidden transitions, respectively, as a function of $\theta$. Figure 5.12(a) contains the $\star$ transition intensity for the "black" component only since the corresponding transition for the "red" component is too small to be observed. For the $+$ transition, the peaks from the two components overlap (cf. Figure 5.9) and cannot be easily distinguished. So, Figure 5.12(b) shows the combined intensity for both components. Both panels show good agreement between experiment and simulation with the intensity growing near avoided crossings or at large transverse fields (large angles in Figure 5.12(b)), where tunneling is enhanced. There's some discrepancy at $\theta > 50^\circ$ for the $+$ transition.

### 5.4.3 $T_2$ measurement.

Another interesting feature of Figure 5.5 is that the linewidths of the peaks associated with forbidden transitions tend to be significantly smaller than for the allowed transitions. This suggests that these peaks are homogeneously broadened. Inhomogeneous broadening due to a distribution of dipolar fields would produce peaks of nearly the same width. On the other hand, homogeneously broadened lines should have a width that scales as $1/\Delta\langle S_z\rangle$, an effect we find to roughly hold. Figure 5.13 shows values of $T_2$ extracted from the measured linewidths as a function of $\theta$ for the four transitions (two allowed and two forbidden) examined in this study. To obtain this data, we fit the peaks in each spectra in Figure 5.5 to Lorentzians to determine the width $\Delta H$ (in Oersted). After converting to a width $\Delta B$ (in Gauss), we used the calculated field dependence of the transition frequency, $\partial f/\partial B$ to determine $T_2$: $T_2 = (\frac{\partial f}{\partial B}\frac{\partial B}{\partial H}\Delta H)^{-1}$. The analysis was done for the peaks associated with the "black" component (cf. Figure 5.9). The data is consistent with $T_2 \approx 1$ ns among all spectra. $T_2$ for forbidden transitions are mostly shorter than those for allowed transitions. This may be a manifestation of the fact that the forbidden-transition frequency is more affected by the dipolar field based on the strong dependence of the energy levels on field in

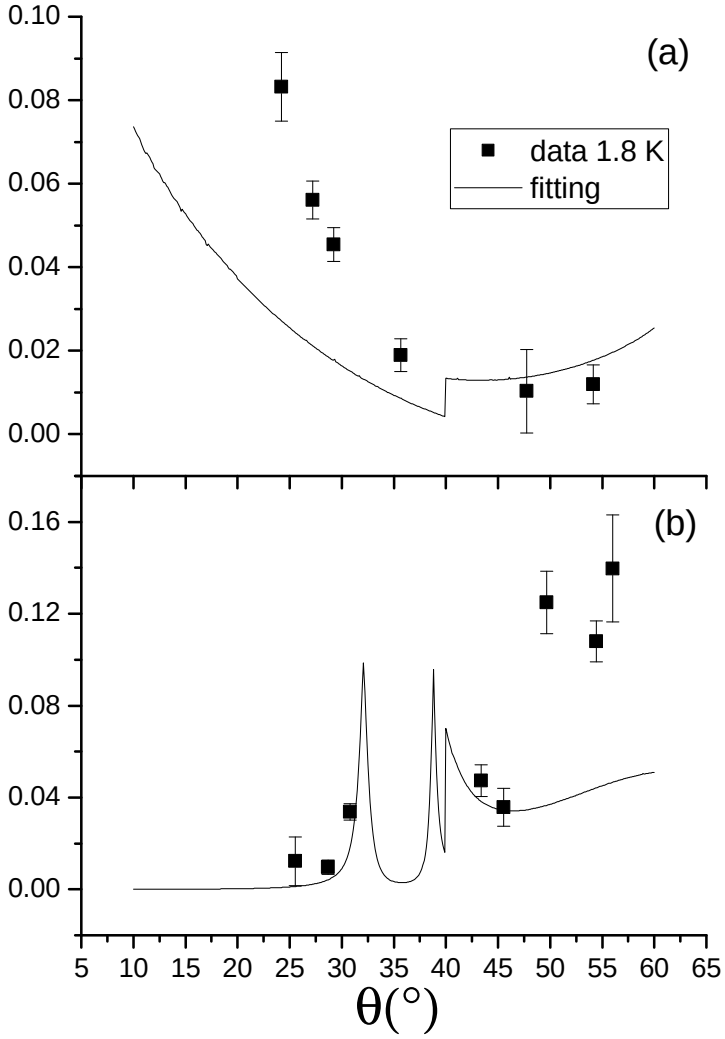


**Figure 5.12.** Spectral intensity as a function of $\theta$ for the (a) $\star$ and (b) $+$ forbidden transitions. Points are experimental data determined from the area of the associated peaks. Curves are simulation results based on calculated transition matrix elements. For (a), the data and simulations are for the "black" transitions only. In contrast, because the peaks for $+$ transitions substantially overlap, the experimental and calculated data in (b) is the combined intensity for both components.

the energy diagram. Our $T_2$ values are comparable to the measurements reported earlier for this molecule [44] . Long $T_2$ times have been achieved in a variety of molecular spin systems by various methods of dilution [31, 78, 79] to reduce dipole couplings and a similar approach is possible with $Ni_4$ by cocrystallizing it with the diamagnetic analog $Zn_4$. Even

in the absence of such techniques, the short $T_2$ found in this study may be compensated by the high density of $Ni_4$ molecules in a crystal that leads to an enhanced coupling to the radiation field [80].

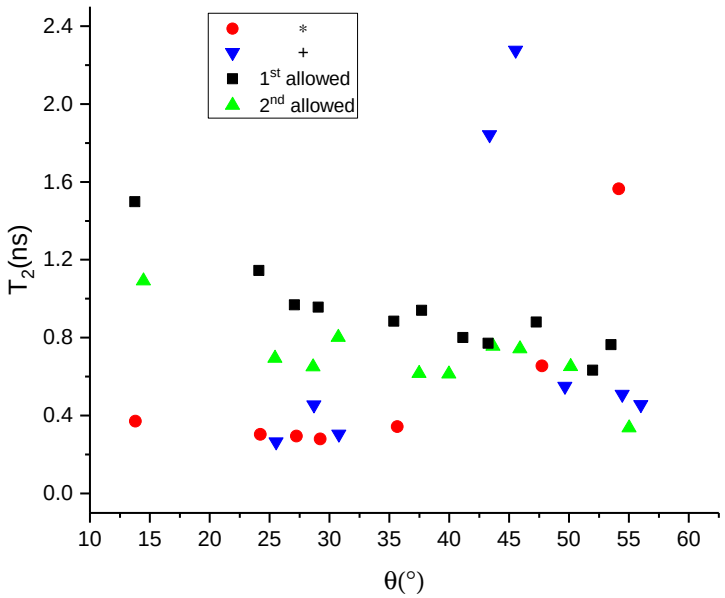


**Figure 5.13.** $T_2$ measurements for allowed and forbidden transitions, as indicated, as a function of $\theta$. Data was extracted from peak widths of spectra in Figure 5.5. Most of the data presented is for the "black" component only. For the $+$ transition, the peaks for the two components overlap at most values of $\theta$ and cannot be distinguished. Under those circumstances, $T_2$ values for that transition represent the width of the combined peak for both components.

### 5.4.4 Forbiddenness and Catness

One way to characterize the forbidden transitions observed in this study is to calculate the change of the expectation value of $S_z$ during the transition. For an allowed transition, $|\Delta\langle S_z\rangle| \approx 1$ while for forbidden transitions, this quantity is expected to be significantly larger. Figure 5.14 shows calculated values of $|\Delta\langle S_z\rangle|$ as a function of $\theta$ for the four transitions (two allowed and two forbidden) studied for the black component. For each transition in the figure, the value of $|\Delta\langle S_z\rangle|$ changes from $\sim 1$ to a much larger value, up

to $\sim 7$. This change occurs as the final energy eigenstate of the transition passes through an avoided crossing and the character of the transition switches from being allowed to forbidden or vice versa. The calculations were done for two values of the azimuthal angle $\phi_H$, corresponding to the values for samples 2 and 3. The arrows in the figure indicate experimental conditions for which forbidden transitions were observed, showing that some of these transitions have very large values of $|\Delta\langle S_z\rangle|$.

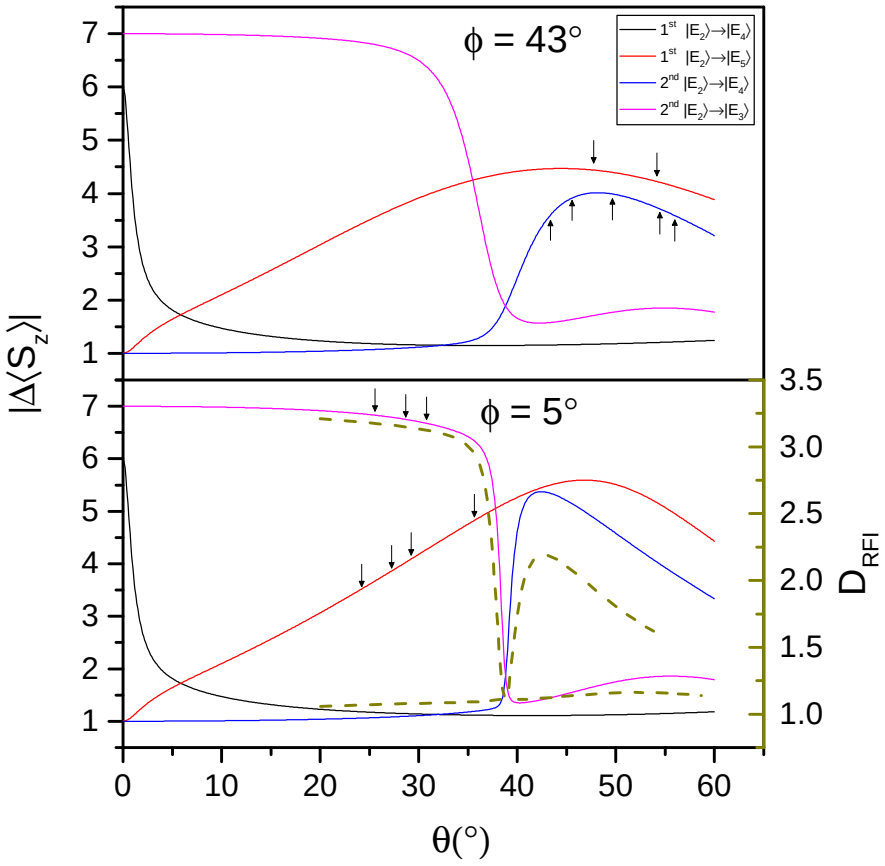


**Figure 5.14.** Calculated $|\Delta\langle S_z\rangle|$ as a function of $\theta$ for the transitions studied. Calculations were performed for $\phi_H = 5°$ and $43°$, as indicated, corresponding to the orientations of Samples 2 and 3, respectively. The labels "$1^{st}$" and "$2^{nd}$" refer to the transitions that occur at lower and higher fields, respectively. Note that for the $1^{st}$ transitions, $|E_2\rangle \approx |m = 4\rangle$ while for the 2nd transitions, $|E_2\rangle \approx |m = 3\rangle$. Arrows indicate experimental conditions where forbidden transitions were observed. For comparison, the dashed lines give calculated values of $D_{RFI}$ for superpositions that can be created using the states involved in the $2^{nd}$ allowed and forbidden transitions.

A more rigorous method to quantify the macroscopicity of the superposition states is the quantum Fisher information, $\mathcal{F}_\psi$ [81, 82]. Filippo Troiani, who is the main contributor to this part of the work in our paper [74], calculated the magnitude of this quantity for the superposition states involved in the observed forbidden transition. $\mathcal{F}_\psi$ is defined as:

$$\mathcal{F}_\psi = \max_X [\langle\psi| X^2 |\psi\rangle - \langle\psi| X |\psi\rangle^2] \tag{5.7}$$

$\mathcal{F}$ equals the variance of the operator $X = \sum_{i=1}^{4} \mathbf{n}_i \cdot \mathbf{s}_i$, where the $\mathbf{s}_i$ refers to the $i$th ionic spin of the molecule. $\mathcal{F}_\psi$ is maximized over all possible unit vectors $\mathbf{n}_i$. Here we consider states belonging to the maximal-spin multiplet (S = 4) of the $Ni_4$ molecule. One can show that in this case the maximum is always obtained with parallel vectors ($\mathbf{n}_i = \mathbf{n}$, $\forall i$). We calculate $\mathcal{F}_\psi$ for the linear superposition $|\psi\rangle = (|i\rangle + e^{i\eta} |f\rangle)/\sqrt{2}$ (maximized over $\eta$). We also determined the relative Fisher information:

$$D_{RFI} = \frac{\mathcal{F}_\psi}{\frac{1}{2}[\mathcal{F}_i + \mathcal{F}_f]} \tag{5.8}$$

where each $\mathcal{F}$ is independently determined. Figure 5.15 shows calculated oscillator strength (OS, transition matrix element squared) and $D_{RFI}$ for the + transition of the black component between $|i\rangle = |E_2\rangle \approx |m = 3\rangle$ and $|f\rangle = |E_3\rangle$, the second and third lowest energy eigenstate, respectively, as a function of field. $\theta$ is adjusted to maintain the resonance condition between the radiation frequency and the transition, following the right dashed black curve in Figure 5.9. At large fields, $|f\rangle \approx |m = 2\rangle$, the transition between these levels is allowed with a large OS and $D_{RFI} \approx 1$. At low fields, $|f\rangle \approx |m = -4\rangle$ and the transition is more catlike ($D_{RFI} \approx 3$) and forbidden (OS small). Near the anticrossing, where states with very different values of $m$ hybridize, relatively large values of $D_{RFI} \approx 3$ can persist, while the oscillator strength remains finite. The inset shows a parametric plot of $\mathcal{F}_\psi$ vs OS, illustrating how, near the anticrossing, one quantity rises as the other falls, but both can be substantial over some region. Complementary behavior is seen for the transition between states $|E_2\rangle$ and $|E_4\rangle$ (Figure 5.16). In this figure, we again see a correlation between OS and

$D_{RFI}$ where a large $D_{RFI}$ indicates a forbidden transition. We also found that the behavior of $D_{RFI}$ and $|\Delta\langle S_z\rangle|$ are qualitatively similar (dashed lines in Figure 5.14), indicating that $|\Delta\langle S_z\rangle|$ is a reasonable proxy for quantifying the catness of a transition.

Tunneling plays an important role in enabling the forbidden transitions with large $|\Delta\langle S_z\rangle|$ and a catlike quality. In addition, large tunnel splittings allow the tunneling effect to extend beyond the immediate vicinity of an anti-crossing. In our experiment, the forbidden transitions occur slightly away from the anticrossings, permitting direct single-photon transitions between states largely localized in opposite wells. When the tunnel splitting are much smaller, one enters the photon-assisted tunneling regime, where the process can be interpreted as an allowed ESR transition followed sequentially by tunneling between wells [83]. Tunnel splittings can be enhanced by applying large transverse fields. However, a field only acts as a perturbation when the Zeeman energy is small compared to molecule's anisotropy energy. In the large-field regime, the transitions become allowed and the catness of superposition states becomes suppressed. Furthermore, going beyond the perturbation regime undermines the advantages afforded by clock transitions. The tunnel splittings found intrinsically in $Ni_4$ ($\sim 1$ GHz) are sufficient to observe forbidden, catlike transitions without the need of applying significant transverse fields to enhance tunneling.

### 5.4.5 Perturbation regime and Zeeman regime

We compare our work with the ESR experiment by del Barco [44] where a strong transverse magnetic field was applied to open up the tunnel splitting between $|m = -4\rangle$ and $|m = 4\rangle$. Figure 5.17 shows the simulated tunnel splitting between $|m = -4\rangle$ and $|m = 4\rangle$ as a function of the transverse field $B_T = B\sin(\theta)$. At $B_T = 0$, the tunnel splitting is only tens of MHz, which is due to the intrinsic anisotropy of $Ni_4$. As $B_T$ increases, the transverse Zeeman term $\mu_B B_T(g_x S_x \cos\phi + g_y S_y \sin\phi)$ comes into effect and leads to a 4th-order dependence of the tunnel splitting to $B_T$: $\Delta E \propto B_T^4$. An even larger $B_T$ will bring the transition into the Zeeman regime so that $\Delta E$ depends on $B_T$ linearly.

To illustrate this, the order of dependence, $\frac{d(\ln \Delta E)}{d(\ln B_T)}$, as a function of $B_T$ is plotted in Figure 5.18(a). As can be discerned, starting from $B_T = 0$, the dependence of $\Delta E$ on $B_T$ is negligible because the intrinsic anisotropy couples the two states in second-order perturbation theory ($\langle 4|C(S_+^4 + S_-^4)|0\rangle \langle 0|C(S_+^4 + S_-^4)| - 4\rangle$) in the absence of the Zeeman term. When the field is brought up to $\sim 500$ mT, the perturbation of 4th order from $B_T$ and first order from the anisotropy connects states $|4\rangle$ and $|-4\rangle$. One of the perturbation term can be $\langle 4|C(S_+^4 + S_-^4)|0\rangle \langle 0|B_T S_+| - 1\rangle \langle -1|B_T S_+| - 2\rangle \langle -2|B_T S_+| - 3\rangle \langle -3|B_T S_+| - 4\rangle$. Therefore $\Delta E$ depends on $B_T$ to the power of four or $\frac{d(\ln \Delta E)}{d(\ln B_T)} = 4$. As $B_T$ increases further, even higher order perturbation from Zeeman term (e.g. 6th order) comes in and the curve peaks at $B_T \sim 2100$ mT. Beyond this point, one begins to enter the non-perturbative Zeeman regime and the order of dependence starts to decrease to unity slowly. The arrows in the figure depict the experimental conditions in del Barco et al.'s experiment. All the points are beyond the perturbation regime. In Figure 5.18 (b) and (c), the perturbation order of the tunnel splittings studied in our experiment ($|m = 2\rangle \leftrightarrow |m = -3\rangle$ and $|m = -4\rangle \leftrightarrow |m = 2\rangle$ in Figure 5.3) are plotted as a function of field: As shown in (b), to mix state $|m = 2\rangle$ and state $|m = -3\rangle$, a first order perturbation from Zeeman term is needed to get a non-zero coupling at low fields: e.g. $\langle 2|C(S_+^4 + S_-^4)| - 2\rangle \langle -2|B_T S_+| - 3\rangle$. As the transverse field increases, the Zeeman effect prevails the anisotropy and the higher order of perturbation from the Zeeman effect comes in. When the field is too large that the perturbation condition is not satisfied, the perturbation order starts to drop slowly to unity. A similar analysis applies to the energy splitting between $|m = -4\rangle$ and $|m = 2\rangle$ as well, shown in Figure 5.18(c). Initially a second-order perturbation from the Zeeman term is required for a finite coupling: e.g. $\langle 2|C(S_+^4 + S_-^4)| - 2\rangle \langle -2|B_T S_+| - 3\rangle \langle -3|B_T S_+| - 4\rangle$, resulting in a plateau at $\sim 2$. As the field is brought up, the order of Zeeman perturbation increases and peaks at $\sim 1200$ mT. When the field increases further, it enters the Zeeman regime that the order of field dependance slowly drop down to unity. The arrows shown in (b) and (c)

indicate the conditions for the actual experiments and are mostly located in the perturbation regime, indicating that the transverse field usually acts as a perturbation in our experiment.

## 5.5 Summary

In this experiment, we observed highly forbidden transitions in $Ni_4$ that involves a change of spin by several times $\hbar$, nearly reversing the direction of the spin. Study of the linear superposition of the two states associated with the transition shows that Schrödinger cat states can be obtained in the $Ni_4$ molecule, which is unusual for magnetic dipole transitions. To observe such a forbidden transition, a significant tunnel splitting is necessary and in $Ni_4$ it is mainly enabled by the intrinsic anisotropy of the molecule and the transverse magnetic field only contributes as a perturbation. In achieving this, the resonance field needs to be slightly detuned from the tunneling field so that the two states involved in transition are substantially localized. Such forbidden transitions may be exploited in quantum information processing since the transitions are less affected by fluctuations of local magnetic fields, and thus may have longer coherence times.

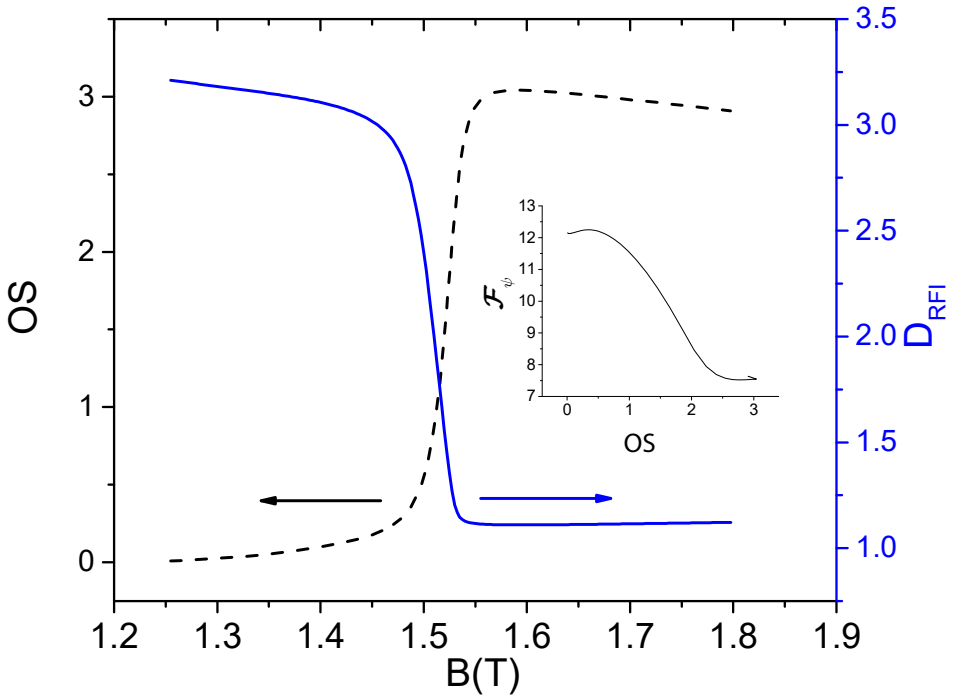


**Figure 5.15.** Oscillator strength (OS) and $D_{RFI}$ for one of the transitions studied as a function of field. Here $|i\rangle \approx |m = 3\rangle$ and $|f\rangle = |E_3\rangle$ are the second- and third-lowest energy eigenstates, respectively. As the field increases, the angle $\theta$ is adjusted to maintain resonance of the transition with the radiation frequency. For this pair of levels, the transition is forbidden (allowed) at small (large) fields with a crossover at the field of the anticrossing. The inset shows a parametric plot of $\mathcal{F}_\psi$ vs. OS. Near the anticrossing, one quantity rises as the other falls, and both are substantial over some region. Calculations were done using the parameters for the black component and $\phi_H = 5°$, corresponding to Sample 2.

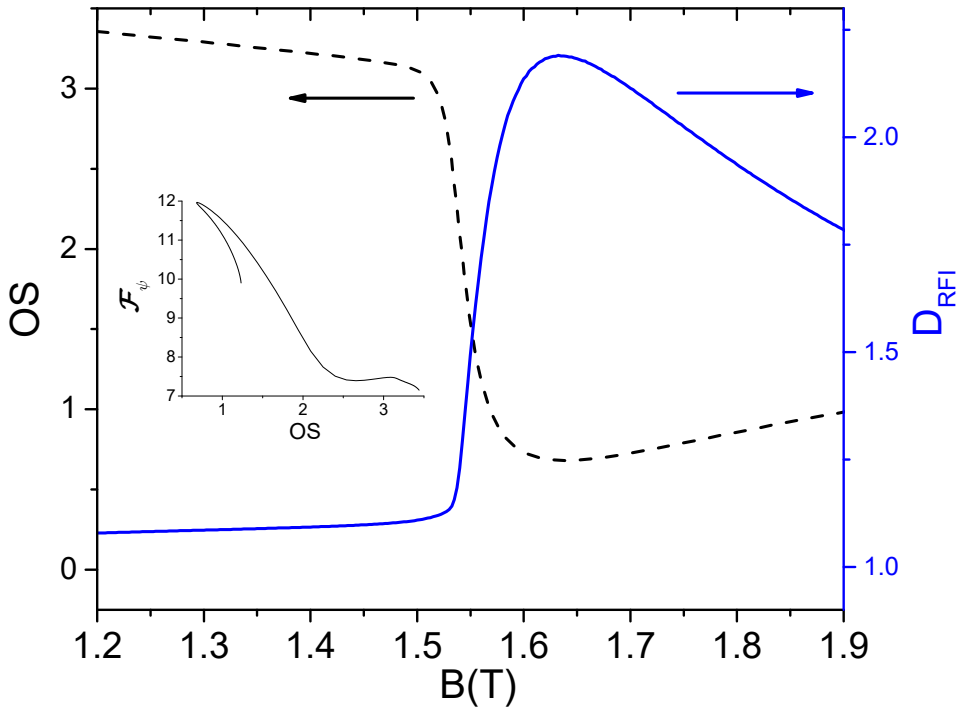


**Figure 5.16.** Calculated oscillator strength (OS) and $D_{RFI}$ for the transition between $|E_2\rangle$ and $|E_4\rangle$, the second- and fourth-lowest energy eigenstates, respectively, as a function of $B$. The angle $\theta$ is adjusted to maintain resonance of the transition with the radiation frequency. The inset shows a parametric plot of $\mathcal{F}_\psi$ vs. OS. Calculations were done using the parameters for the black component and $\phi_H = 5°$, corresponding to Sample 2.

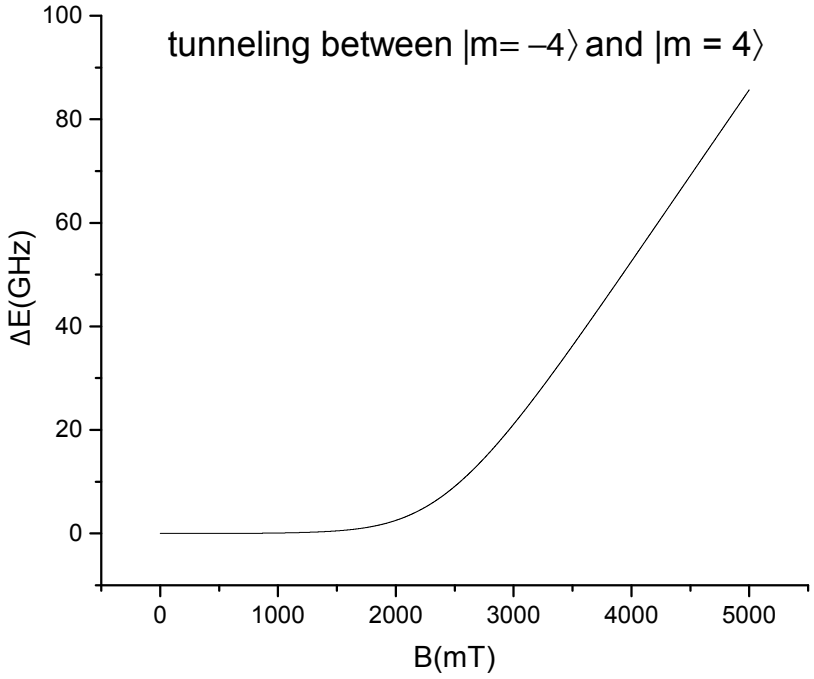


**Figure 5.17.** Tunnel splitting energy between $|m = -4\rangle$ and $|m = 4\rangle$ as a function of transverse field.

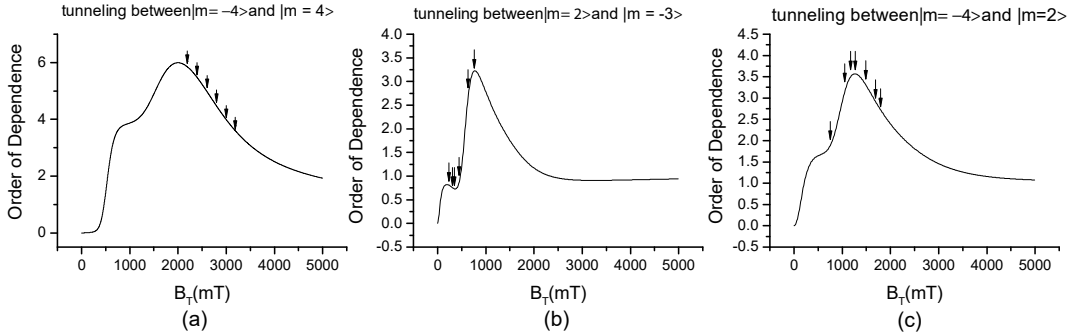


**Figure 5.18.** Perturbation order $\frac{d(\ln \Delta E)}{d(\ln B_T)}$ due to the off-diagonal terms in the Hamiltonian matrix as a function of the transverse field. (a) shows the perturbation order for the tunnel splitting between states $|m = 4\rangle$ and $|m = -4\rangle$ in del Barco et al.'s experiment [44]. (b),(c) shows the perturbation order for the tunnel splitting between states $|m = 2\rangle \leftrightarrow |m = -3\rangle$ and $|m = -4\rangle \leftrightarrow |m = 2\rangle$ respectively. The arrows shown on the curve marked the actual fields used in the experiments.

# CHAPTER 6

# AHARONOV-CASHER EFFECT EXPERIMENT.

## 6.1 Introduction

In this chapter, I will discuss the effort we've made toward observing another macroscopic quantum phenomenon in superconducting circuits — interference of the quantized units of magnetic flux as they tunnel out of a superconducting ring. This effect can be seen as a two-dimensional analog of the Aharonov-Casher effect, which is similar to the well known Aharonov-Bohm effect. In the latter, a particle with electric charge $q$ traveling along some path $P$ in a region with zero magnetic field $\mathbf{B}$, but non-zero $\mathbf{A}$ (by $\mathbf{B} = 0 = \nabla \times \mathbf{A}$), acquires a geometric phase $\varphi$ [84], given by:

$$\varphi = \frac{q}{\hbar} \int_P \mathbf{A} \cdot d\mathbf{x} \tag{6.1}$$

Therefore particles, with the same start and end points, but traveling along two different routes will acquire a phase difference $\Delta\varphi$ determined by the magnetic flux $\Phi_B$ through the area between the paths (via Stokes' theorem and $\nabla \times \mathbf{A} = \mathbf{B}$) (Figure 6.1(a)), given by:

$$\Delta\varphi = \frac{q\Phi_B}{\hbar} \tag{6.2}$$

Closely related to the Aharonov-Bohm effect is the Aharonov-Casher effect [85], in which an uncharged magnetic dipole $\mu$ travelling around an infinitely long charged line will pick up a phase difference $\Delta\varphi$ (Figure 6.1(b)) :

$$\Delta\varphi = \frac{\mu\lambda}{h} \tag{6.3}$$

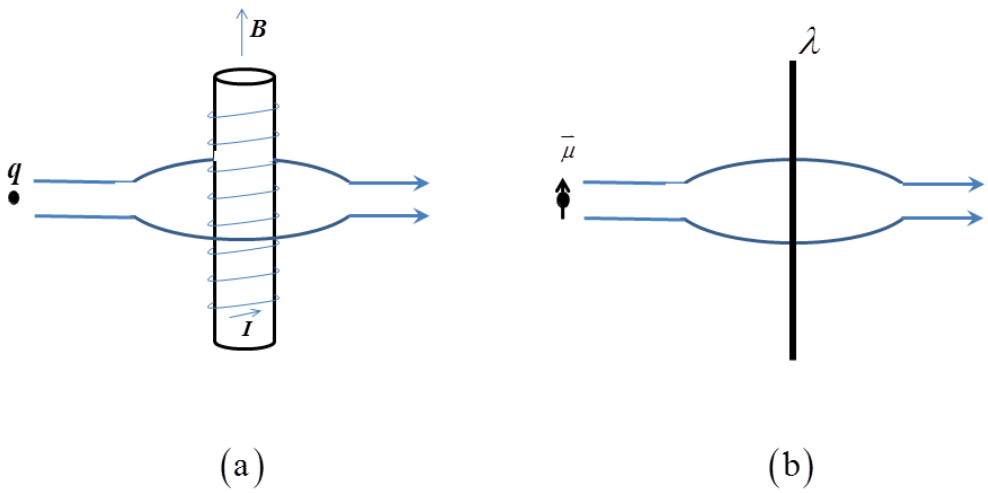


**Figure 6.1.** (a) Aharonov-Bohm effect (b) Aharonov-Casher effect.

where $\lambda$ is the charge density of the line.

### 6.1.1 Flux Tunneling

The same phase effect in the Aharonov-Bohm effect is responsible for the quantized-flux requirement in a superconductor having a hole through it [86]. This quantization occurs because the superconducting wave function (order parameter) must be single valued, so that the line integral of the phase change around any closed contour must be equal to $2n\pi$, where $n$ is an integer. In a single piece of superconductor without any holes through it, $n$ must be 0. Because in the limit that the integrated path is chosen to have vanishing length, the total phase change must be 0. Then any infinitesimal increase in path length cannot produce a phase change of $2\pi$. However, this continuity argument cannot be applied to a superconductor with a hole through it. Thus the phase change around the hole is determined by the magnetic flux through that hole:

$$\Delta\varphi = \frac{2e\Phi}{\hbar} = 2n\pi, \quad n \in \mathbb{Z} \tag{6.4}$$

so that the flux trapped in the hole must be quantized:

$$\Phi = nh/2e = n\Phi_0, \quad n \in \mathbb{Z} \tag{6.5}$$

Magnetic flux may generally be treated as a classical variable, capable of smooth changes between any limits. However, in the case of a superconducting ring (Figure 6.2(a)), in order to screen out the magnetic fields from the interior of a bulk superconductor, surface currents must flow. It is the sum of the externally applied flux $\Phi_x$ plus this internally generated flux that must be quantized:

$$\Phi_i = \Phi_x + Li_s = n\Phi_0 \tag{6.6}$$

where $L$ is the ring inductance around which the supercurrent $i_s$ flows. Thus the ring of superconductor responds to any change in external flux $\Delta\Phi_x$ by setting up an equal but opposite change in flux. As long as the specimen remains superconducting, the total flux linking the ring will remain constant, and quantized, at the same value. Only by applying a huge external flux can a transition from one flux state to another happen. This can only be achieved by the destruction of superconductivity in the material so that the order parameter goes everywhere to zero before re-establishing itself at a new value of internal flux, which is very unpredictable [86].

If the superconducting loop is interrupted by a small gap (Figure 6.2(b)), which forms the so-called Josephson junction, internal flux may tunnel out of the loop when there are relatively small changes in external flux.

### 6.1.2 RCSJ Model of a Josephson junction

The Josephson junction is the most fundamental element in superconducting devices. It consists of two pieces of superconducting material separated by a very thin layer of insulator that is normally one or two nanometers thick [87]. These devices show two important

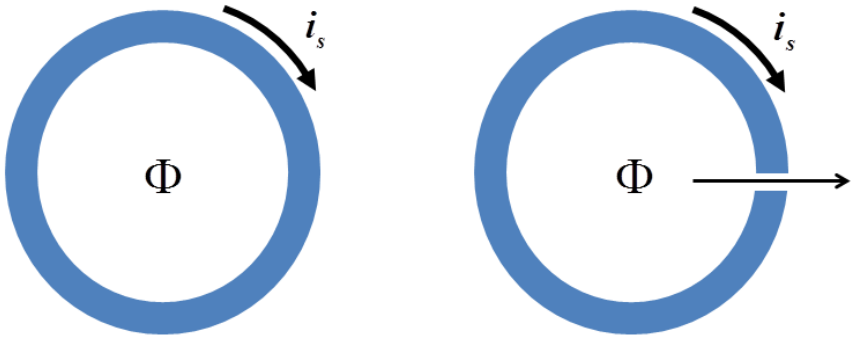


(a) A closed superconducting ring (b) A superconducting ring with a gap

**Figure 6.2.** Superconducting rings trapping magnetic flux.

effects. The first, known as the dc Josephson effect, is that a supercurrent can flow across the junction, with the magnitude determined by the phase difference in the two electrodes:

$$I_s = I_c \sin \phi, \tag{6.7}$$

where the critical current $I_c$ is the maximum supercurrent that the junction can support. Here we use the gauge invariant phase $\phi = \varphi - \frac{2\pi}{\Phi_0} \int \vec{A} \cdot ds$ to guarantee the single valuedness of current. The second effect is that, if a voltage difference $V$ is maintained across the junction, then the phase difference $\phi$ will evolve according to:

$$d\phi/dt = 2eV/\hbar \tag{6.8}$$

so that the current will be an alternating current of amplitude $I_c$ and frequency $\nu = 2eV/h$. This second Josephson effect is known as the ac Josephson effect.

A physical junction is modeled as a resistively and capacitively shunted junction, i.e. as an ideal junction shunted by a resistance $R$ and a capacitance $C$ (Figure 6.3). The resistance $R$ builds in dissipation in the finite voltage regime, without affecting the lossless dc regime, while $C$ reflects the geometric shunting capacitance between the two electrodes.

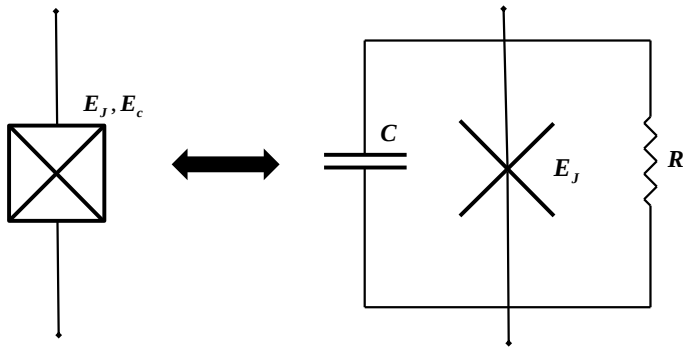


**Figure 6.3.** RCSJ model for a real Josephson junction.

The current $I$ entering the junction splits into three branches, passing through the ideal junction, the resistance and the capacitor:

$$I = I_c \sin\phi + V/R + CdV/dt \tag{6.9}$$

If we eliminate $V$ in Eq. 6.9 using Eq. 6.8 and rearrange the equation, we get:

$$(\frac{\hbar}{2e})^2 C\ddot{\phi} = \frac{\hbar}{2e} I - E_J \sin\phi - \frac{\hbar}{4e^2 R}\dot{\phi} \tag{6.10}$$

where $E_J = (\hbar/2e)I_c$ is the Josephson coupling energy. From a dynamical standpoint, this differential equation describes the motion of a particle of mass $(\hbar/2e)^2 C$ moving along the $\phi$ axis in a potential:

$$U(\phi) = -E_J \cos\phi - (\hbar I/2e)\phi \tag{6.11}$$

subjected to a viscous drag force $(\hbar/2e)^2(1/R)d\phi/dt$. Qualitatively, the potential is a line with some sinusoidal oscillations that form local wells along the $\phi$ axis (Figure 6.4). The

biasing current $I$, essentially controls the tilt of this 'washboard potential'. When $I$ is below $I_c$, the particle can be stuck in one of the local wells and its average velocity is then zero. So the voltage across the junction, which is proportional to $\dot{\phi}$, is zero as well. If $I = I_c$, the local minima of the tilted cosine disappear. The particle starts sliding down the inclined washboard and results in a finite voltage $V$, corresponding to a 'running state' in which $\phi$ increases at the average rate $2eV/\hbar$.

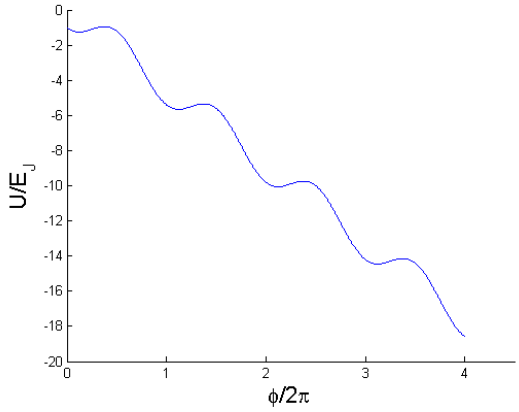


**Figure 6.4.** Tilted washboard potential for a single junction.

### 6.1.3 rf SQUID (Super-conducting Quantum Interference Device)

Now consider an rf SQUID consisting of a superconducting loop of inductance $L$ interrupted by a Josephson junction with critical current $I_c$ (Figure 6.5). When an external flux $\Phi_x$ is applied, a screening current, $I_s = (\Phi - \Phi_x)/L$, is induced in the loop. The classical equation of motion for $\phi$ can be derived using the RCSJ model which is analogous to that of particle in a potential

$$U(\phi) = -E_J \cos\phi + \frac{(\Phi - \Phi_0)^2}{2L}. \tag{6.12}$$

If the equation is expressed in terms of the flux trapped in the loop by using the relationship $\phi = 2\pi\Phi/\Phi_0$, this can be written as [7]:

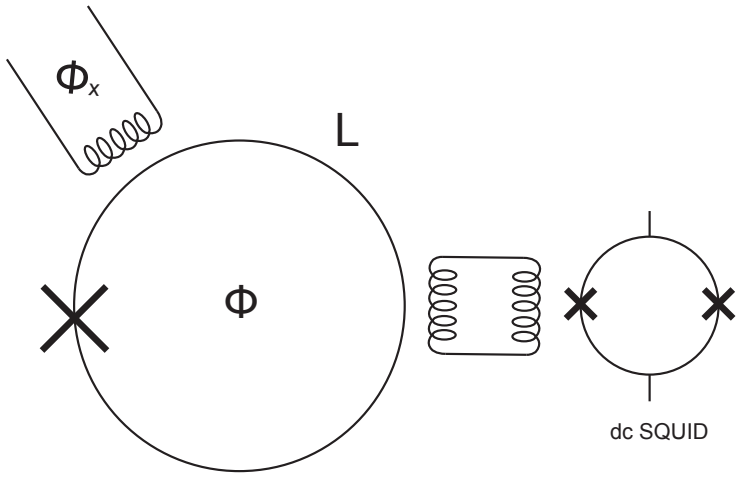


**Figure 6.5.** Experimental setup to measure flux tunneling out of the rf SQUID.

$$U = U_0 \left[ \frac{1}{2} \left( \frac{2\pi \left( \Phi - \Phi_x \right)}{\Phi_0} \right)^2 - \beta \cos(2\pi\Phi/\Phi_0) \right], \tag{6.13}$$

where $U_0 = \frac{\Phi_0^2}{4\pi^2 L}$ and $\beta \equiv 2\pi L I_c/\Phi_0$. This is a double-well potential if $\beta <\sim 4.6$ and its barrier height depends on $I_c$. For $\Phi_x$ close to half a flux quantum, the potential forms a double well about $\Phi = \Phi_0/2$. Each well represents distinct macroscopic flux states of the SQUID: the induced flux points either up or down. Equivalently, the two wells correspond to two distinct persistent current states, anticlockwise or clockwise (Figure 6.6).

Any change in $\Phi_x$ then tilts the potential. Quantum mechanically, the system can tunnel from one well to the adjacent well through the barrier. For weak damping, the system has quantized energy levels localized in each well. By adjusting $\Phi_x$ carefully, levels in each well will align and give rise to resonant tunneling [7]. One flux quantum is conceptually tunneling out of the loop through the Josephson junction and the change of flux state can be detected by a dc SQUID magnetometer.

If the Josephson junction in the loop is replaced by a Bloch transistor—two junctions separated by a small superconducting island on which the charge can be induced by an ex-

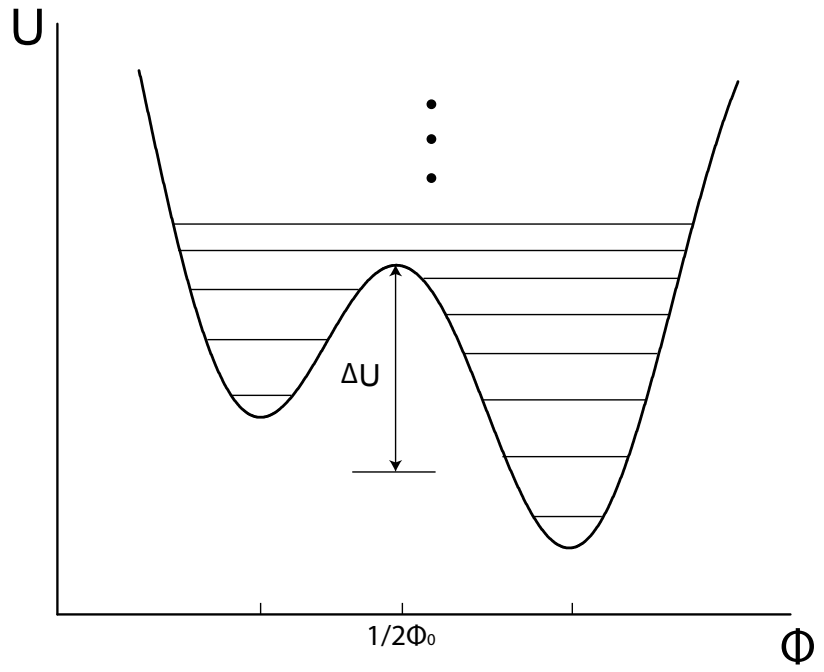


**Figure 6.6.** Double-well potential tilted with $\Phi_x = 0.7\Phi_0$. Left (right) well corresponds to the persistent current state circulating clockwise (counter-clockwise).

ternal gate voltage (Figure 6.7(a)), the flux inside the loop can theoretically tunnel through either of the two Josephson junctions. Because of the charge induced on the island, the flux tunneling through different junctions will pick up different geometric phases allowing interference when recombining [88]. The Hamiltonian for this system is:

$$H = \frac{Q^2}{2C} + \frac{(2en - q)^2}{2C_\Sigma} + \frac{(\Phi - \Phi_x)^2}{2L} - E_{J1}\cos\phi_1 - E_{J2}\cos\phi_2, \qquad (6.14)$$

where $n$ is the number of Cooper pairs charging the island, $q = C_g V_g$ is the gate-voltage-induced charge, and $C_\Sigma$ is the total capacitance of the island relative to all other electrodes. The flux $\Phi$ in the SQUID is related to the total phase differences across the two junctions by $2\pi\Phi/\Phi_0 = \phi_1 + \phi_2 = \phi$. $\Phi$ is conjugate to the charge $Q$ on the capacitance $C$ between the ends of the SQUID loop: $[\Phi, Q] = i\hbar$. The phase of the island $\theta = (\phi_1 - \phi_2)/2$ is conjugate to $n$: $[\theta, n] = i$. The first two terms in the Hamiltonian represent the kinetic energy and the

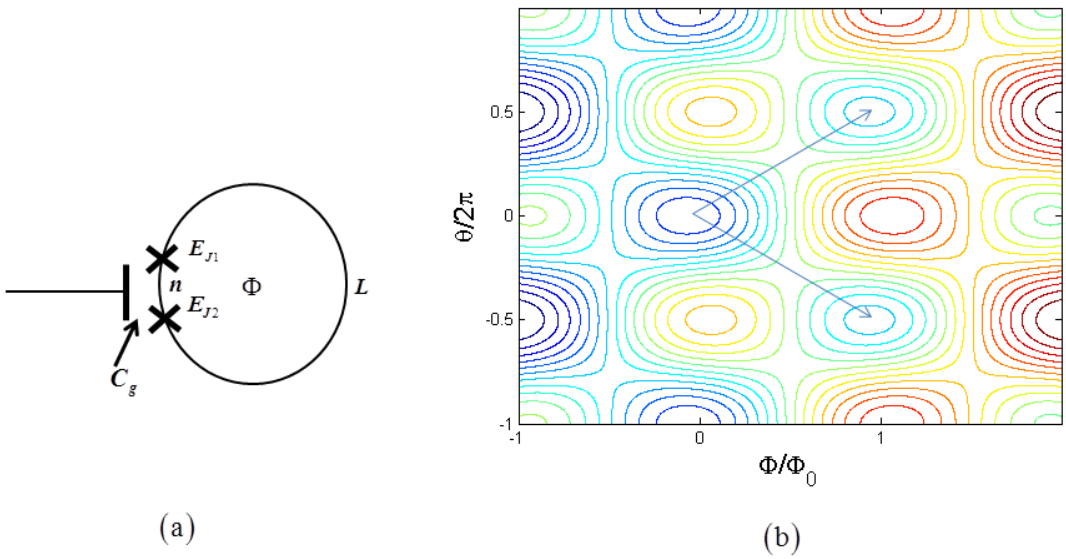


**Figure 6.7.** (a) An rf SQUID with the single junction replaced by a single Cooper pair transistor. (b) Two-dimensional potential described by Eq. 6.14.

remaining terms represent the potential energy. Figure 6.7(b) shows the two-dimensional potential for the case $\Phi_x = \Phi_0/2$ and $E_{J1} = E_{J2}$. The particle that starts at the minimum $\theta = 0, \Phi/\Phi_0 = 0$ initially can tunnel to the two neighboring minima $\theta = 0.5, \Phi/\Phi_0 = 1$ and $\theta = -0.5, \Phi/\Phi_0 = 1$. Given that the two junctions are identical, the tunnel splitting is related to the voltage induced charge $q$ by [88]:

$$\Delta = 2\Delta_0 \cos(q\pi/2e), \tag{6.15}$$

where $\Delta_0$ is the tunnel splitting associated with one path. When $q = e$, the relative phase of the two paths is $\pi$, the interference is destructive and the tunneling rate goes to zero.

The goal of this project is to observe this flux-tunneling-interference effect. However, because of the experimental challenges associated with the above experiment, we started with another system — the single Cooper-pair transistor (SCPT) (Figure 6.9), where one flux quantum tunneling through a junction corresponds to the change of $2\pi$ of the phase difference of that junction. In the SCPT system, where no loop is responsible for trapping

flux, the change of $\phi$ across two junctions by $2\pi$ is an indication that one flux quantum tunnels from one side of the SCPT to the other through the junction. Then flux-tunneling suppression can be indirectly demonstrated as the elimination of $2\pi$ phase change in the SCPT. However, a phase change of an integer multiple of $4\pi$ is still allowed since two-flux-quantum tunneling can take place in that case. This can be achieved by driving the SCPT with microwave radiation and examining the Shapiro steps in the $I$-$V$ curve of the device.

### 6.1.4 Microwave-driven single Josephson junction

When a current-biased single junction is irradiated with microwaves of angular frequency $\omega$, the response of the supercurrent gives rise to constant-voltage Shapiro steps in the $I$-$V$ curve at voltages $V_n = n\hbar\omega/e$ [89]. In our semi-classical model, the microwave radiation has the effect of exerting an oscillatory force on our particle in the washboard (Figure 6.4). When the bias current is sufficiently small, the particle is effectively stuck in a well in the potential. However, if there is a driving force, the particle may be knocked out of the well, but won't speed up down the washboard because of the oscillatory force. It just slides down one well at a time with every cycle of the radiation. Correspondingly, the mean velocity $\dot{\phi}$ is $\omega$. Moreover, the radiation has the phase-lock effect that even when the washboard potential is tilted a little more, the particle maintains this velocity, which gives the first Shapiro step on the $I$-$V$ plot:

$$V_1 = \frac{\hbar}{2e}\dot{\phi} = \frac{\hbar}{2e}\omega \tag{6.16}$$

Once the potential is tilted to the point that the particle slides down two wells with every cycle, $\dot{\phi}$ jumps discontinuously to $2\omega$. The $n_{th}$ voltage step in the $I$-$V$ curve corresponds to the particle rolling down $n$ wells each period (Figure 6.8):

$$V_n = \frac{n\hbar}{2e}\omega \tag{6.17}$$

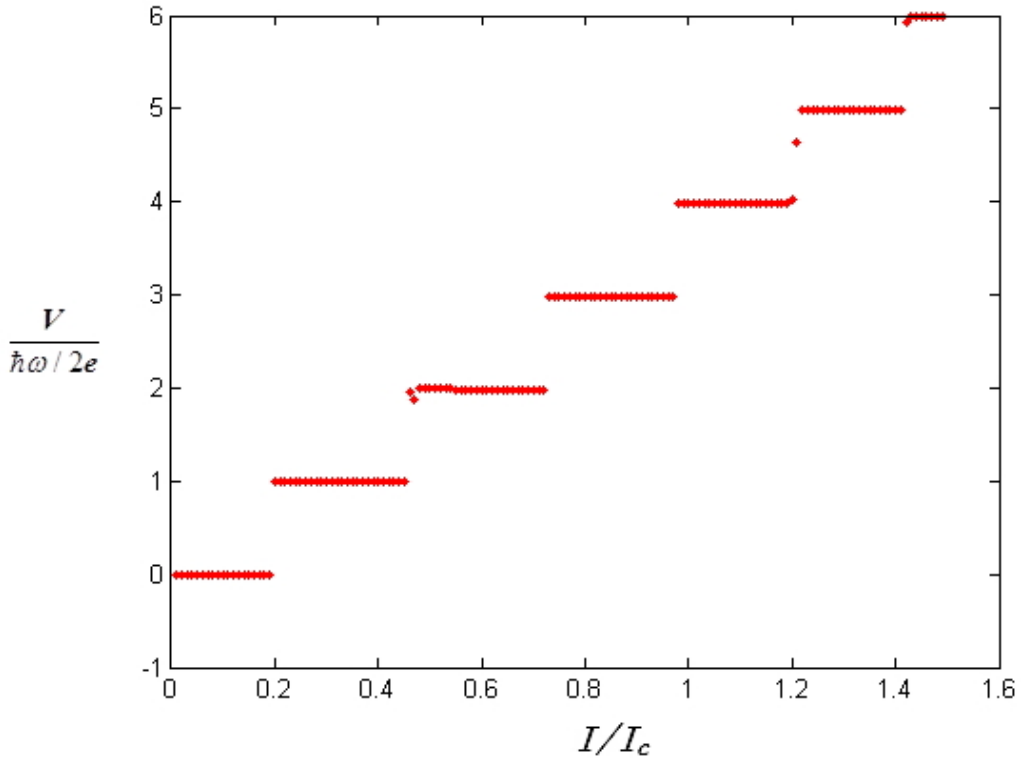


**Figure 6.8.** Calculated $I$-$V$ curve of a single Josephson junction subject to an rf drive, showing Shapiro steps.

### 6.1.5 Microwave-driven Single Cooper-pair Transistor

The single Cooper-pair transistor is composed of two Josephson junctions connected in series, leaving a center 'island' that is isolated by the junction capacitances (Figure 6.9). The Hamiltonian for the device is :

$$\widehat{H}_0 = E_c(\widehat{n} - n_g)^2 + \frac{(2e\widehat{N})^2}{2C_{ds}} - E_{J1}\cos(\widehat{\phi}_1) - E_{J2}\cos(\widehat{\phi}_2), \tag{6.18}$$

where $C_{ds}$ is the total capacitance across the two junctions and $E_c = \frac{(2e)^2}{2C_\Sigma}$ is the charging energy of the island and $C_\Sigma$ is the capacitance of the island. We will consider the $E_{J1} = E_{J2} = E_J$ case. Then the second term of $H_0$ becomes:

$$-2E_J \cos\widehat{\theta} \cos\frac{\widehat{\phi}}{2} \tag{6.19}$$

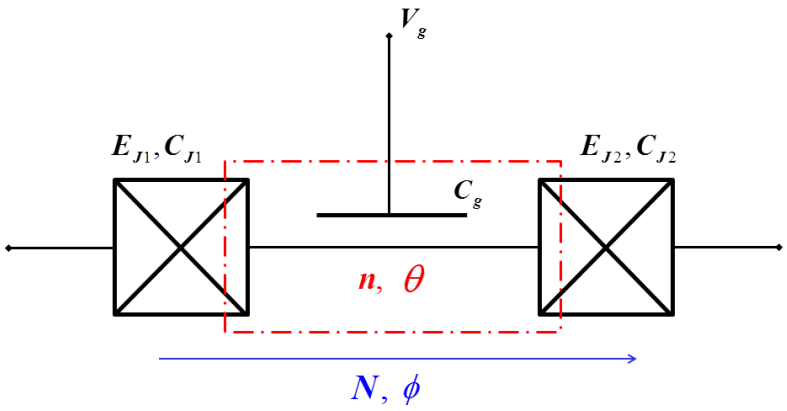


**Figure 6.9.** The single Cooper-pair transistor.

Because $\widehat{\theta}$ and $\widehat{n}$ are conjugate, the $\cos\widehat{\theta}$ term can be expressed in the basis of charge eigenstates as:

$$\cos\widehat{\theta} = \frac{1}{2}\sum_{n\in\mathbb{Z}}(|n+1\rangle\langle n| + |n-1\rangle\langle n|) \tag{6.20}$$

The full Hamiltonian of the isolated SCPT expanded in the $n$ basis becomes:

$$\widehat{H} = \sum_{n\in\mathbb{Z}}\left[E_c(n-n_g)^2|n\rangle\langle n| - (E_J\cos\frac{\widehat{\phi}}{2})(|n+1\rangle\langle n| + |n-1\rangle\langle n|)\right] + \frac{(2e\widehat{N})^2}{2C_{ds}} \tag{6.21}$$

This Hamiltonian includes the common elements of electrostatic charging and an effective coherent coupling given by $E_J{}^{eff} = E_J\cos\frac{\widehat{\phi}}{2}$. This is the basic prescription for studying the competition between the charging effect, which favors in discrete charge states, and the Josephson effect, which creates coherent charge-state mixing and modifies the energy levels. This competition is characterized by the dimensionless ratio $\alpha = E_J/E_c$.

Because of the existence of stray capacitance, $C_{ds}$ is large and the 'kinetic energy' term $\frac{(2eN)^2}{2C_{ds}}$ can be ignored. Thus the quantum fluctuation of $\phi$ can be neglected and $\phi$ can

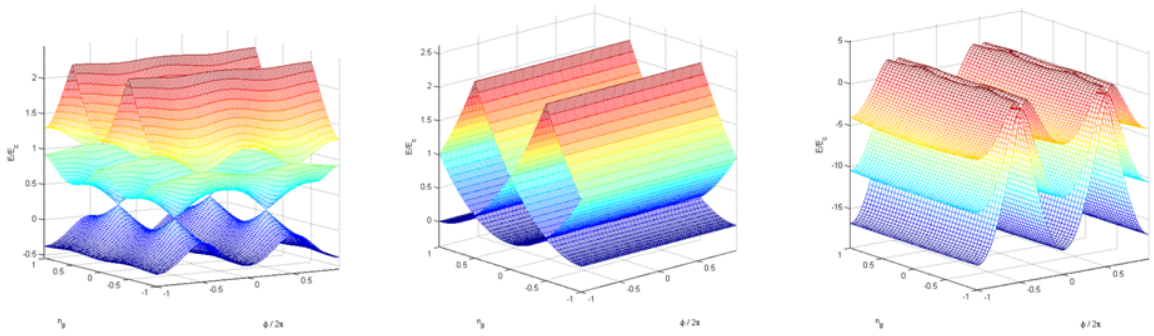

(a) (b) (c)

**Figure 6.10.** Energy-band structure of SCPT: (a) $\alpha = 0.5$ (b) $\alpha = 0.01$ (c) $\alpha = 10$.

be treated as a classical variable. The matrix given by Eqn. 6.21 then can be efficiently diagonalized to give an accurate determination of the eigenvalues and eigenvectors within a diagonalization subspace. The eigenvalues at different $\phi, n_g$ values form energy bands $E_m(\phi, n_g)$, where $m$ is the band index representing different charge states. Figure 6.10(a) shows that when $\alpha \simeq 1$, the energies are 1-periodic in $n_g$, and are also $2\pi$-periodic in $\phi$. The charging effects controlled by $n_g$ influence the dynamics of the system. When $\alpha << 1$, then the Josephson effect is unimportant. The term containing $\phi$ in the Hamiltonian is negligible and charge dynamics dominate. However, charge states are not coupled with each other because of the absence of Josephson coupling. On the other hand, if $\alpha >> 1$, charging effects are unimportant, indicating that the number of charges induced on the island plays no role in the dynamics of the system. The SCPT degrades to a single junction. We are more interested in the regime $\alpha \simeq 1$, where the transport properties related to Cooper-pair tunneling are significantly affected by the number of charges induced on the island.

At fixed $n_g$, each energy band is analogous to the Josephson washboard potential used to describe the behavior of a 'classical' Josephson junction. The minimum energy separation between the bands is given by: $E_G(n_g) = E_c(1 - 2|n_g| \bmod 2)$. Biasing the SCPT with current is like adding a biasing-energy term $\frac{\hbar}{2e} I\phi$ to the Hamiltonian, which produces a tilting of the energy bands along the $\phi$ axis (Figure 6.11). Because the gap between the

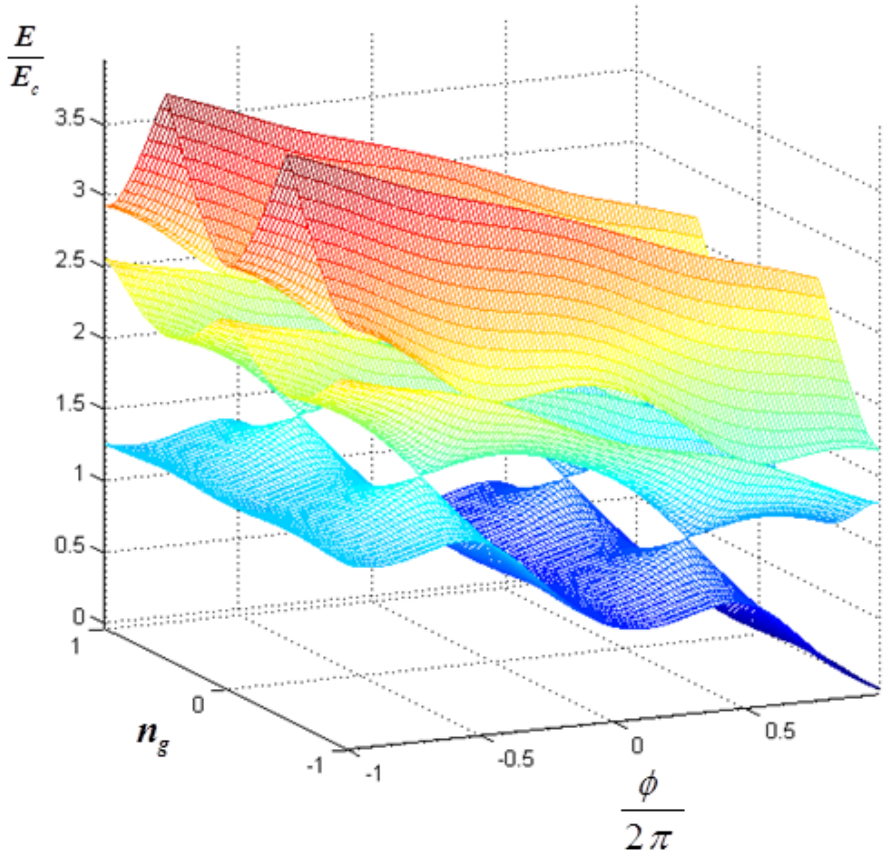


**Figure 6.11.** Energy landscape of the current-biased SCPT with $I_{bias} = 0.1I_c$.

first two energy bands reaches a minimum at $\phi$ mod $2\pi = \pi$, the system can make transitions between the bands while sweeping through these anticrossings, which is known as a Landau-Zener (LZ) transition. The probability that the transition happens is given by [90]:

$$P_{LZ} = \exp\left[-\frac{2\pi(\Delta E/2)^2}{\hbar v}\right] \tag{6.22}$$

where $v$ is the time rate of change of the energy difference between the levels, and $\Delta E$ is the minimum energy splitting. Figure 6.12 shows that when $n_g = 1/2$, $\Delta E = 0$, and an LZ transition happens every time the system passes the anticrossing. Then the particle will roll down the washboard potential two wells at a time. If the SCPT is driven by microwaves, it is straightforward to show that the odd Shapiro steps, which correspond to moving one

well every cycle, will disappear. Only even steps remain, meaning there is a doubling of Shapiro-steps period. This is indirect evidence that the flux tunneling is totally suppressed.

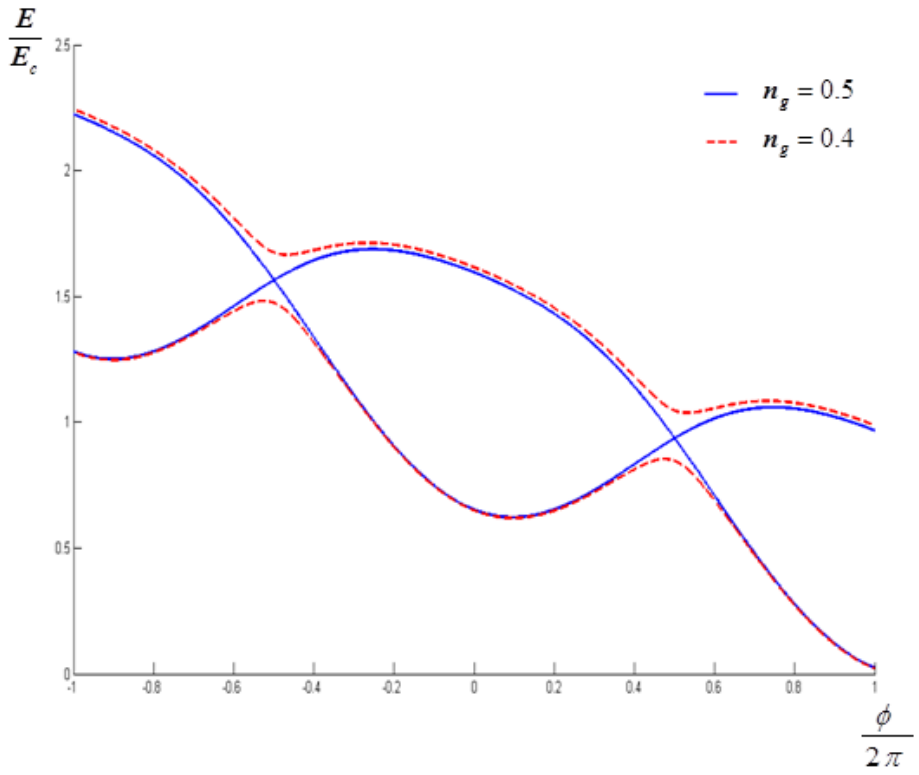


**Figure 6.12.** Slice of the SCPT energy landscape with $n_g = 0.5$ and $n_g = 0.4$.

Any asymmetry of the two junctions in the SCPT will lift the band degeneracy, which will lower the LZ transition rate. In our device, we make one of the junctions 'tunable' by replacing it with a dc SQUID whose total critical current can be tuned by the magnetic flux $\Phi_{dc}$ through it [54]:

$$I_{cSQUID} = 2I_{c1} \cos \left| \frac{\pi \Phi_{dc}}{\Phi_0} \right| \tag{6.23}$$

where $I_{c1}$ is the critical current of each junction of the SQUID and $I_{cSQUID}$ is the critical current of the SQUID. $I_{cSQUID}$ can be tuned to any value between 0 and $2I_{c1}$ through $\Phi_{dc}$. By carefully choosing the parameter $\Phi_{dc}$, we expect to have $I_{cSQUID}$ equal the critical

current of the other junction of the SCPT so that a LZ transition happens every time it passes through the degeneracy point.

The Landau Zener transition between the energy bands of SCPT has also been studied by R. Deblock's group [91]. In their experimental setup, the SCPT is voltage biased to produce an AC supercurrent. When a LZ transition happens, the current-phase relationship doubles because the energy-phase relationship doubles. As a result, the frequency of the AC supercurrent with constant voltage biasing will double and can be detected by another Josephson junction capacitively coupled to the SCPT. Our project involves studying the LZ transition in SCPT by applying microwave radiation and observing the Shapiro step spacing doubling. Moreover, we replace one junction of the SCPT with a SQUID so that we can control the asymmetry of the SCPT and thus control the LZ transition probability. We expect to study the LZ effect more quantitively this way.

In a recent experiment done by Bell et al. [92], they observed the effect of the Aharonov-Casher (AC) interference on the spectrum of a superconducting system containing a symmetric Cooper pair box (CPB) and a large inductance. The dependence of the device's resonant frequency on the loop flux oscillates with the period 2e of the charge induced on the CPB island.

## 6.2 Experiment

The experiment consists of a single Cooper-pair transistor with one junction replaced by a dc SQUID. All these elements are thin-film superconducting circuits that were fabricated in a clean room at UMass and an electron-beam evaporator at Amherst College. They were measured at very low temperatures in a top-loading dilution refrigerator. Measurements can be performed with nearly fully automated electronics that were designed especially for ultra-low-noise measurements.

### 6.2.1 Fabrication of Al/AlO$_x$/Al Tunnel Junction Circuits

Advances in thin-film nanofabrication in the past three decades have made possible a new class of circuits in which the motion of individual charge carriers can be manipulated and controlled at the single-electron level. The circuit described here is based on the transport channel provided by a thin insulating tunnel barrier separating superconducting electrodes. The size of the junction is designed to fulfill several requirements: First, the junction area should be small enough, so that the charging energy, $E_c$, is much larger than the thermal energy ($k_bT$) at temperatures that can be routinely obtained in a dilution refrigerator. Second, in order to avoid quasiparticle poisoning, in which an unpaired electron will tunnel onto the island and will destroy the 2e-periodicity in the gate charge, the charging energy must be less than the superconductor energy gap $\Delta$. Finally, we want $E_c$ to be close to $E_J$: On the one hand, $E_c$ should be large enough so that the gate charge modulation can be observed. On the other hand, $E_c$ shouldn't be too large otherwise we will lose the Josephson coupling between different charge states.

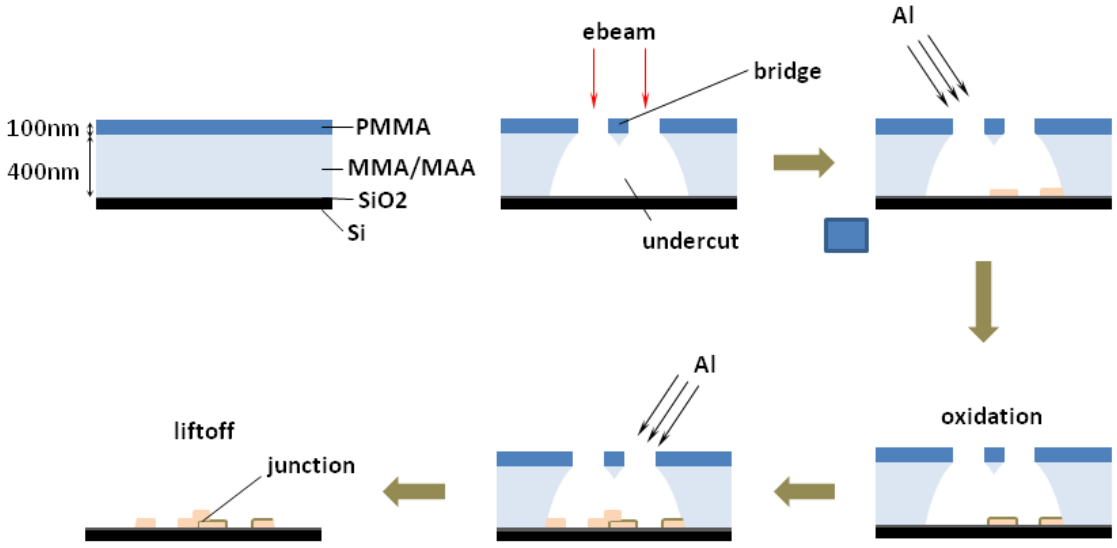


**Figure 6.13.** Fabrication process for a Josephson junction using the 2-angle shadow evaporation technique.

The circuits used in this work are based on Al/$AlO_x$/Al tunnel junctions fabricated using the standard 2-angle shadow evaporation technique (Figure 6.13). Nanometer size Josephson junctions are fabricated using a bi-layer electron-sensitive resist. The thick high-sensitivity bottom resist layer provides the substantial undercut necessary for forming the overlap of two deposited layers of Al. This layer is 10% (MMA,MAA) coplolymer in 2-ethoxyethanol spun at 4500 rpm (400 nm thick) for 1 minute and baked on the hotplate at 180 °C for 1 minute. The thin higher-resolution top layer allows pattern transfer using electron-beam lithography. This layer consists of 2% PMMA in chlorobenzene spun at 1500 rpm for 1 minute (100 nm thick) and baked on a hotplate at 180 °C for 30 minutes. After eletron-beam exposure and resist development, the patterned resist serves as a stencil mask for the lift-off of self-aligned tunnel junctions. The junctions are formed by the overlap of two aluminum depositions carried out at oblique angles. An oxidation after the first metal deposition forms the thin oxide tunnel barrier. The transparency of the barrier is controlled by the oxygen exposure, which is defined as the oxygen pressure multiplied by the oxidation time.

The e-beam lithography is performed using accelerating voltage of 15 kV. Polygon writing with a typical dose of 650 μC/cm$^2$ is used to define the device geometries. Development of the device patterns is done in a 3:1 solution of methly-isobutly-ketone (MIBK):isopropyl alcohol (IPA) for 60 sec at room temperature. Two-angle depositions of high-purity aluminum (99.999%) from $+25^\circ$ and $-25^\circ$, 30 nm and 50 nm thick, respectively, are made in an e-beam evaporator with a background pressure of $\sim 1\times10^{-7}$ mBar. An in-situ oxidation performed between the two aluminum depositions forms the tunnel barrier. In this step, the sample is exposed to a mixture of $O_2$ and Ar ($O_2$ 15%, Ar 85%) of 10 mbar for 5 minutes, which gives the critical-current density of the junction around 150 A/cm$^2$.

Figure 6.14 shows the geometries of the circuit imaged with SEM. The left junction size is 100 nm × 200 nm and each junction of the dc SQUID on the right is 100 nm × 180 nm. Thus the critical current of the left junction $I_{c1}$ is expected to be 27 nA. One other

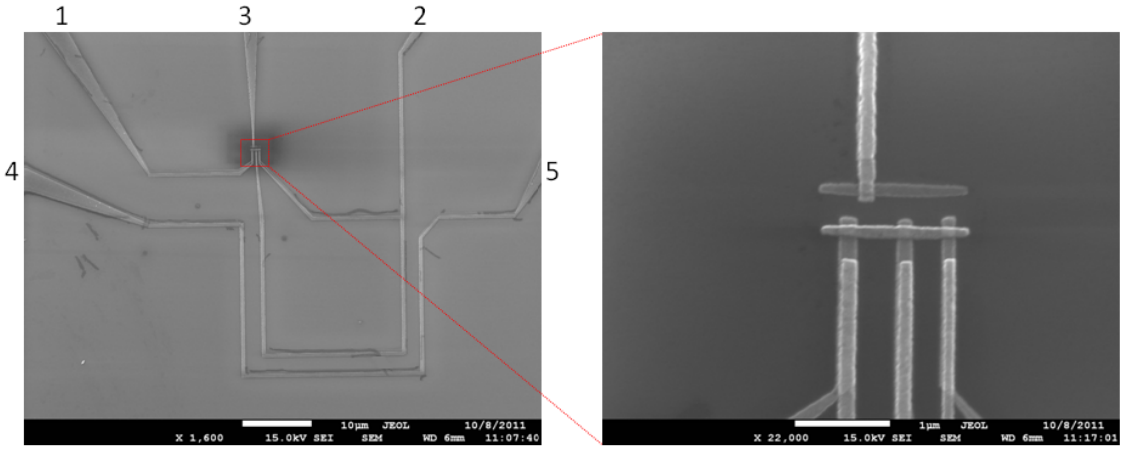


**Figure 6.14.** SEM image of the single Cooper-pair transistor with one junction replaced by a dc SQUID.

important length scale in Figure 6.14 is the size of the dc SQUID loop, which determines its inductive coupling to the flux-bias line. The dc SQUID is used as a tunable Josephson junction with the critical current modulated by the applied flux. In order to be able to use it as such, we must operate in a regime in which the total flux through the loop and the applied flux are nearly the same. This condition is met when $\beta = 2\pi L I_c/\Phi_0 << 1$ [54], which indicates that $L << 10$ nH. On the other hand, the cooling power of the fridge at 100 mK is 250 μW, which imposes an upper limit of 1mA for the current flowing in the biasing line. So in order to tune the flux in the loop to around $1\Phi_0$, the mutual inductance $M$ should be larger than $\frac{\Phi_0}{I_{max}} = 2$ pH. Based on these requirement, the size of the dc SQUID loop in the experiment is designed to be 25 μm $\times$ 25 μm. The self inductance of the loop and the mutual inductance are calculated using FastHenry to be $21.7$ pH and $6.19$ pH, respectively [93].

### 6.2.2 Sample Cell

The whole experiment is carried out using KelvinoxTLM top-loading dilution refrigerator manufactured by Oxford Instruments; it is capable of achieving a base temperature of

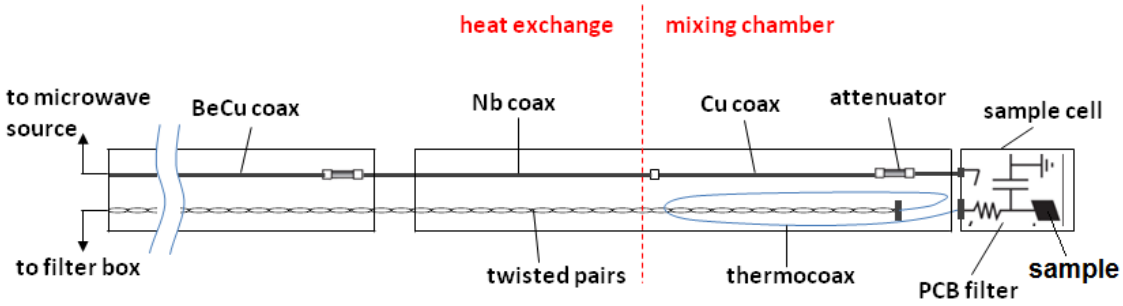


**Figure 6.15.** Schematic diagram of the probe.

$\sim$ 37 mK. The sample is mounted at the end of the probe (2.6 m) (Figure 6.15), which is lowered into the refrigerator.

The silicon chip on which the circuit is fabricated is glued to a printed circuit board (PCB) whose pads are connected to male pins on the board via low-pass RC filters. The leads written on the chip are wire-bonded to the pads of the PCB. The PCB pins mate with female sockets on a stage made of Delrin, which is screwed on to the cell cap at the end of the probe (Figure 6.16). A can made of high-purity aluminum (99.999%) is attached to the cell cap to cover the assembly. The sample cell formed by the can and the cap shield the sample from the ambient magnetic field. There are two small waveguide holes drilled in the cell cap that allows superfluid-helium to flow over the sample. The waveguide holes are $0.0292''$ in diameter, permitting a first-mode frequency of approximately 40 GHz and sheilding all frequencies below 40 GHz out.

### 6.2.3 Filtering

In the base-temperature stage (37 mK) the leads were RC filtered. The filters were standard RC low-pass filters. The capacitors were off-the-shelf 10 nF COG ceramics and the resistors are 1 k$\Omega$ thin metal-film resistors, which gives a cutoff frequency of 630 kHz. Both elements have very low temperature coefficients that are quite stable even in the mK range. Thermocoax cable is used to connect the twisted wires, which lead up to the con-

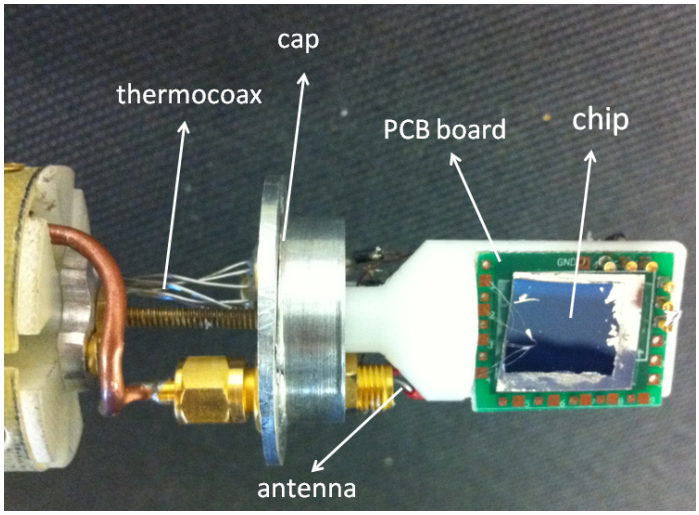


**Figure 6.16.** The bottom of the probe: The PCB board with the sample chip is mounted onto a Delrin stage. The antenna is capacitively coupled to the junction. The ensemble is encapsulated inside an Aluminum can (Only the cap is shown).

nector at the top of the fridge, with the copper wires that go into the sample cell; this acts as an efficient high-frequency filter (Figure 6.15). This gives an attenuation of as much as 200 dB/m for a 20 GHz signal [94]. The length of thermocoax cable we used is 60 cm. Besides this, a low-pass Butterworth filter with 130 kHz cutoff frequency is used at room temperature to filter extraneous high-frequency noise. To apply more filtering of high-frequency noise, we added homemade metal-powder filters in series with the thermal coaxial cables. We followed the steps in A. Lukashenko's recipe [95] for making powder filters with embedded capacitors (Figure 6.17). We use stainless steel as the filling powder and expected to obtain an attenuation of $> 100$ dB for signals above 1 GHz.

### 6.2.4 Microwave Signal

The microwave signal, supplied by an Agilent 83650B signal generator, cannot pass through the above filters due to their heavy attenuation of high-frequency signals. To thermally isolate the sample while still admitting high-frequency signals, a niobium ($T_c$ = 9.3 K) coaxial cable was installed in the probe. Superconductors conduct very little heat despite their perfect electrical conductivity. The microwave signal enters the top of the probe

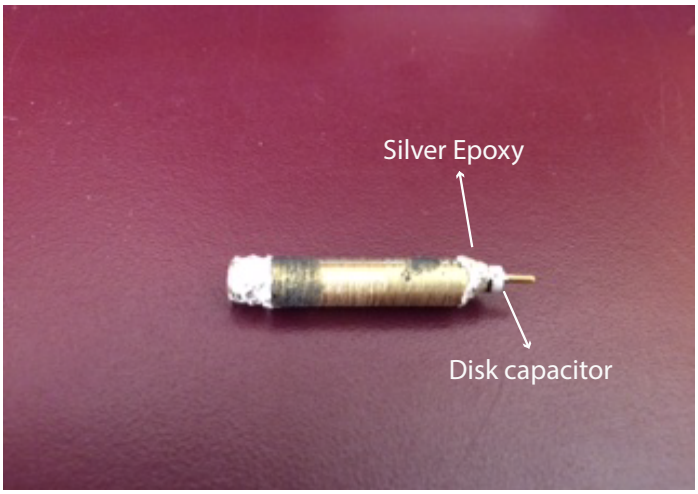


**Figure 6.17.** The metal-powder filter used in our experiment. Silver epoxy is used on each side of the filter to cover the gap between the copper tube and the connector.

through a BeCu coaxial cable, which carries the signal from room temperature to 1 K. This cable is resistive to minimize the heat conducted down to the colder stages of the probe. At the bottom of the BeCu coaxial cable is a 50 $\Omega$, 30 dB attenuator, thermally anchored to the 1K stage of the probe with conductive copper tape. This attenuates all electrical noise by a factor of 1000, dumping the energy to the 1K stage of the refrigerator. The attenuator prevents room-temperature noise from reaching the niobium superconducting cable, which runs from the 1K stage of the probe to the 37 mK mixing chamber. A copper coax cable then brings the signal into the sample cell. Another 10 dB attenuator is placed at $\sim$ 37 mK to attenuate Johnson noise produced by the 50 $\Omega$ attenuator at the 1 K stage. A 1 cm long lead sticking out parallel with the sample chip at the end inside the sample cell acts as an antenna that delivers the microwave radiation.

### 6.2.5 Electronics

Figure 6.18 shows schematically the connections between the external apparatus and the circuit on the sample chip. The room-temperature apparatus consists primarily of three voltage sources (two digitally controlled and one hand-tuned), four amplifiers and a DAQ unit.

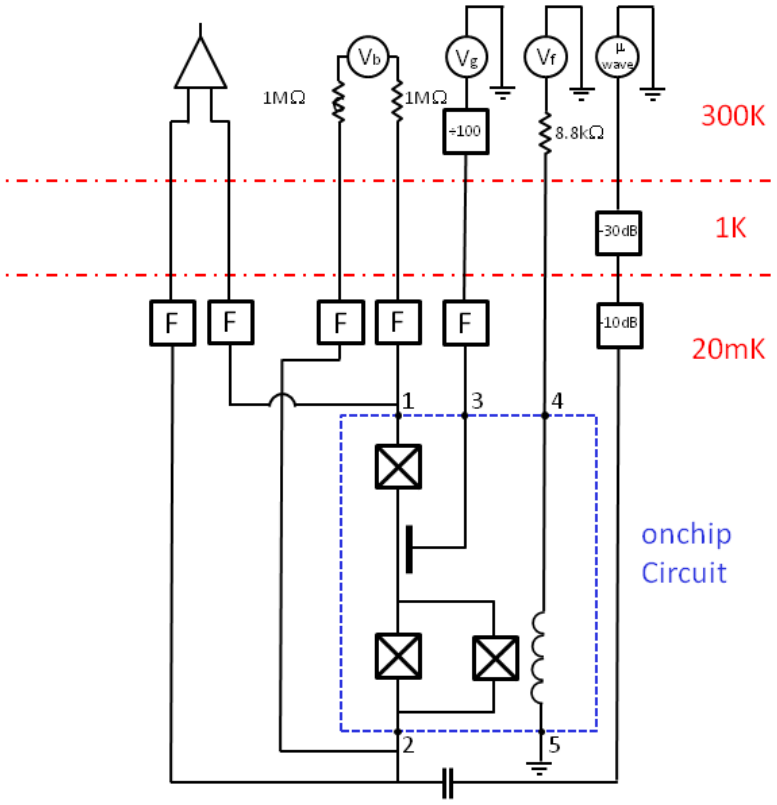


**Figure 6.18.** Schematic diagram of the electrical wiring of the experiment inside of the dilution refrigerator. The square elements marked F are the combination of the thermocoax cables and metal-powder filters.

The voltage sources are digitally programmable, and can be controlled from within a LabVIEW program; they were built following a published design [96]. The key component of the circuit is the AD5235 integrated circuit (IC) which is essentially a dual-channel, digitally-controlled potentiometer whose divider can be swept to vary the output voltage. An AD586 chip provides a monolithic voltage reference of $5$ V for the AD5235. To reduce the $60$ Hz noise, all the ICs and transistors on the board are powered by a set of 18-V rechargeable batteries.

The SCPT in the experiment is current-biased. So a voltage divider and a resistor of $1$ MΩ is used to create a current source with maximum output current $40$ nA. Also, to ensure that the island is referenced to ground so that the change of voltage won't influence the potential of the island, the voltage source is modified to have 'symmetric' outputs ($+5$ V

and $-5$ V) on the two output pins. The supply for the gate voltage is digitally controlled as well. A voltage divider is also needed here to cut the maximum output of the source to $50$ mV, which will induce a maximum number of Cooper pairs on the island: $n_g = C_g V_{max}/2e = 3$. Another (hand-tuned) voltage source is used to supply the flux biasing for the dc SQUID. A current on the order of about $100$ μA is needed to apply a quantum of flux through the dc SQUID loop. This current is much greater than the bias current through the main part of the circuit (40 nA), which raises the issue of Joule heating in the dilution refrigerator. An RC filter is not allowed here since the $1$ kΩ resistor will produce Joule heat of 200 μW, which is comparable to the cooling power of the fridge. However, the resistance of the thermocoax will dissipate 80 μW. So great care must be taken when manually adjust the flux-biasing current.

All the DC signals are amplified with low-noise differential amplifiers before measuring. The signals coming out of the amplifiers are recorded using 16-bit, 250 kS/s multifunction DAQ that has a maximum voltage range of $-10$ V to $10$ V and accuracy of $2.69$ mV .

## 6.3 Numeric Simulation

A physical Josephson junction can be treated by the RCSJ model as a system that obeys the relatively simple dynamical Eqn. 6.9. This second-order differential equation can be easily solved numerically, and the system's $I$-$V$ characteristics may be obtained by solving this equation at different values of $I$, and using Josephson's Eqn. 6.8 to find the voltage from the average 'velocity' of phase $\phi$. Modeling the SCPT is similar. The dynamics of the phase are like a particle moving in the potential shown in Figure. 6.11. At fixed gate voltage, the phase is just moving along a washboard potential with multiple bands (Figure. 6.12). So the particle starting from the ground band has a certain probability to transit to the second band at the crossing points. We attempt to include this Landau-Zener transition into the numerical model, which should give us results relevant to the experiment.

### 6.3.1 Single Josephson junction

Eqn. 6.9 can be transformed to a dimensionless form:

$$d^2\phi/d\tau^2 + Q^{-1}d\phi/d\tau + \sin\phi = i \tag{6.24}$$

in which a dimensionless time variable $\tau = \omega_p t$ is introduced, with

$$\omega_p = (2eI_c/\hbar C)^{1/2} \tag{6.25}$$

being the so-called *plasma frequency* of the junction, and the 'quality factor' Q is defined by $Q = \omega_p RC$. If $C$ is small and $Q \ll 1$, the junction is over-damped. Viscous drag dominates inertia so that the instantaneous velocity of the mass point is proportional to the local force, i.e., proportional to the local slope of the washboard. When C is large so that $Q > 1$, the junction becomes underdamped. The particle slides down the washboard steadily when $I$ exceeds $I_c$. Due to inertia, it is not trapped in a local minimum when $I$ is reduced below $I_c$ until a "retrapping current" is reached. So due to the inertia of the mass, the $I-V$ curve becomes hysteretic. We choose $Q = 1$ in the simulation which corresponds to a light damping regime. The phase-locking effect of the microwaves is more apparent under this regime.

A microwave drive term is added to Eqn. 6.24:

$$\ddot{\phi} = i - \sin\phi - \frac{\dot{\phi}}{Q} + A\sin\omega\tau \tag{6.26}$$

The value of $\omega$ here is also dimensionless and is defined as the ratio of the actual microwave frequency to $\omega_p$. $\omega_p$ is calculated to be 300 rad/s for an 200 nm $\times$ 200 nm junction. Since in the actual experiment, the applied radiation has frequency $\sim$10 GHz, then it is appropriate to set $\omega$ = 0.2 in the simulation. This differential equation is solved with the ODE45 function in matlab. The range $\tau <$ 3Q is cut off to eliminate transients.

For a given value of $i$, the voltage drop across the junction is found using Josephson's equation,

$$V = \frac{\hbar}{2e}\left\langle \dot{\phi} \right\rangle \tag{6.27}$$

In our simulation the average is taken over 32 cycls of the driving radiation. The average $\left\langle \dot{\phi} \right\rangle$ is taken after the system has settled down to its steady state by:

$$\left\langle \dot{\phi} \right\rangle = \frac{1}{64\pi/\omega}\int_0^{64\pi/\omega} \dot{\phi}(t)dt = \frac{\phi(64\pi/\omega) - \phi(0)}{64\pi/\omega} \tag{6.28}$$

In this way, the average velocity $\left\langle \dot{\phi} \right\rangle$ is calculated from the solution to the differential equation. Note that the value of $\left\langle \dot{\phi} \right\rangle$ that corresponds to the Shapiro step voltage $\hbar\omega/2e$ is just $\omega$. An $I$-$V$ curve calculated using the method described above is plotted earlier (Figure 6.8).

### 6.3.2 Modelling the SCPT

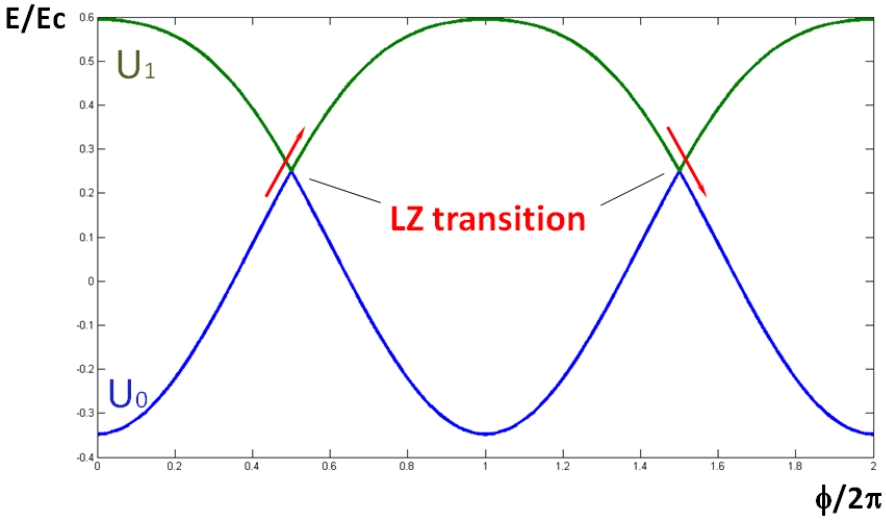


**Figure 6.19.** First two energy bands with $n_g = 0.5$. The 'particle' tunnels to the second band at $\phi/2\pi = 0.5$ and tunnels back to the first band at $\phi/2\pi = 1.5$.

The semi-classical model of the RCSJ model can be extended to the SCPT with the potential energy $U$ that the particle is experiencing replaced by $U_j(\phi, n_g)$, which is the $j_{\text{th}}$ solution of the Hamiltonian:

$$H = \sum_{n\in\mathbb{Z}} \left[ E_c(n-n_g)^2 |n\rangle\langle n| - E_J \cos\frac{\phi}{2}(|n+1\rangle\langle n| + |n-1\rangle\langle n|) \right] \tag{6.29}$$

If a slice of the energy band is taken at constant $n_g$, we obtain washborad potentials for different energy levels. For $E_J$ close to $E_c$, $n_g$ close to $0.5$ and low temperature, only the lowest two energy levels are significantly involved in the paths that the particle will take. Intuitively, the 'force' is calculated by taking the derivative of $U_j$ with respect to $\phi$:

$$f_j(\phi, n_g) = -\frac{\partial}{\partial\phi} U_j(\phi, n_g), \tag{6.30}$$

where $U_j$ are the potential energy of the ground level ($j = 0$) and the first level ($j = 1$). The dynamic equation for the microwave-driven SCPT is then:

$$\ddot{\phi} = i - f(\phi, n_g) - \frac{\dot{\phi}}{Q} + A\sin\omega\tau \tag{6.31}$$

To plot the energy landscapes in Figure 6.11, the eigenvalues for the representation of the Hamiltonian are calculated in the subspace $\{|n\rangle : -3 \le n \le 3\}$. The derivative of the eigenenergies is computed numerically as a centered difference:

$$f(\phi_m) = \frac{U_j(\phi_{m+1}) - U_j(\phi_{m-1})}{2h_\phi}, \tag{6.32}$$

where the domain $0 \le \phi \le 2\pi$ is discretized in steps of $h_\phi$ ($h_\phi = 2\pi/16$ ) to produce the points $\{\phi_m\}$. Since $f(\phi, n_g)$ is $2\pi$-periodic in $\phi$, we use these values to calculate $f(\phi)$ for any $\phi$.

Figure 6.19 shows the first two energy bands for $E_J = E_c$ at $n_g = 0.5$. There are degeneracies at $\phi$ mod $2\pi = \pi$ and therefore $P_{LZ} = 1$ when the particle reaches this point. The particle makes a transition every time it arrives at the degeneracy point. Then the path the particle takes is $4\pi$-periodic in $\phi$. Because of this effective doubling of periodicity, we obtain the doubling of the Shapiro-steps voltage spacing (Figure 6.20).

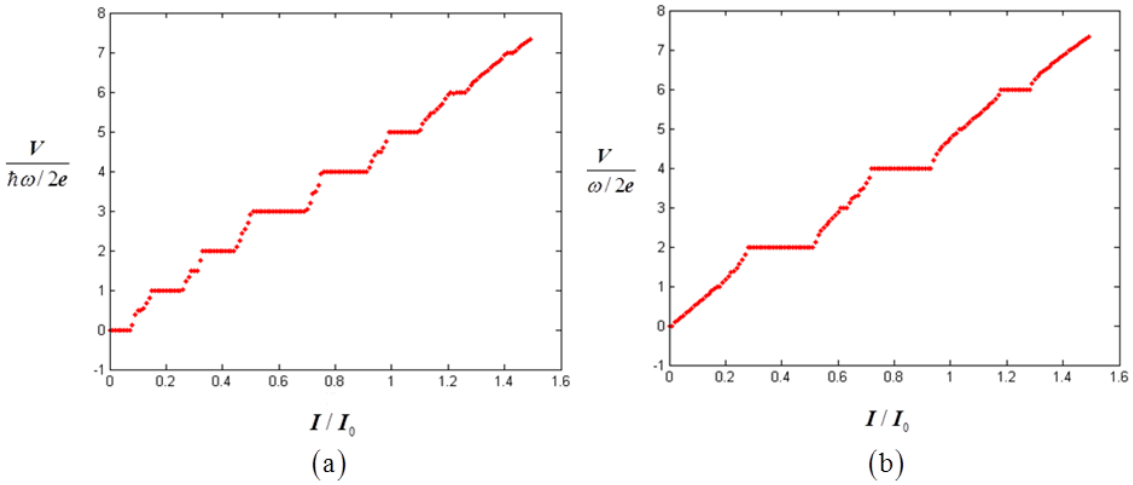


**Figure 6.20.** Simulated $I$-$V$ curve with (a) and without (b) LZ transistion. Here $Q = 1$, $\omega$=0.2 (10 GHz), $A = 1$.

## 6.4 Current results

### 6.4.1 Supercurrent modulation

The most striking consequence of the single Cooper-pair transistor energy bands is the $2e$-periodic modulation of the critical current and this is also the prerequisite for any experimental study of the band structure in the transistor. Fabricating tunnel junctions with low enough capacitance and cooling them down to mK temperature by no means guarantees success. Inadequate noise filtering on the leads connecting the device at low temperature to high temperature noise sources can bring a significant phase-diffusion resistance[1] and

[1]In terms of the tilted-washboard model, the high frequency noise will add to the driving current that brings the phase out of the local minimum before reaching the critical current.

suppressed supercurrent. Quasiparticles and charge noise can effectively destroy the 2e period. In our situation, the supercurrent branch will only show up after leaving the chip at base temperature ($\sim$ 37 mK) for over 24 hours until the charge noise has quieted down.

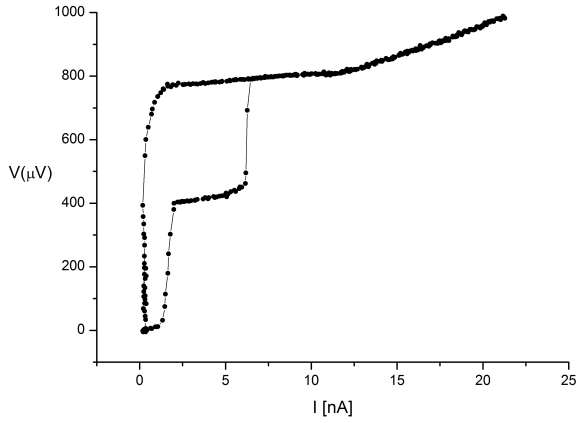


**Figure 6.21.** Measured $I$-$V$ plot of the SCPT at T.

Figure 6.21 shows the typical $I$-$V$ plot of our SCPT device. Switching from the supercurrent branch occurs at $\sim$2 nA. The branch occurring at $V = 2\Delta/e$ ($\sim$400 μV) in the $I$-$V$ curve is caused by the Josephson-plus-Quasiparticle (JQP) cyclical transport process [97]. In this process a Cooper pair tunneling through one junction splits up into two unpaired electrons that then tunnel out the other junction.

As discussed in the end of first section, in order to maximize the LZ tunneling rate, two parameters — gate voltage ($n_g$) and flux biasing current ($\Phi_{dc}$) — are tuned so that the phase passes the degeneracy points every cycle of microwave radiation when it rolls down the washboard potential. The transistor's gate modulation of critical current is measured by ramping the bias current at each gate voltage and recording the current at which the voltage switches irreversibly from one state to another. 1000 raw data points over several modulation periods can be collected in less than 5 minutes. Figure 6.22 shows the measured gate modulation of the critical current branch and the JQP branch at a flux-biasing current of 60 μA. Referring to Figure 6.11, the washboard potential on which the phase is rolling down

is 2e periodic in $n_g$, which leads to the 2e-periodicity in the critical-current modulation. On the other hand, single-electron tunneling is responsible for the JQP branch, which leads to the 1e-periodicity in the JQP modulation.

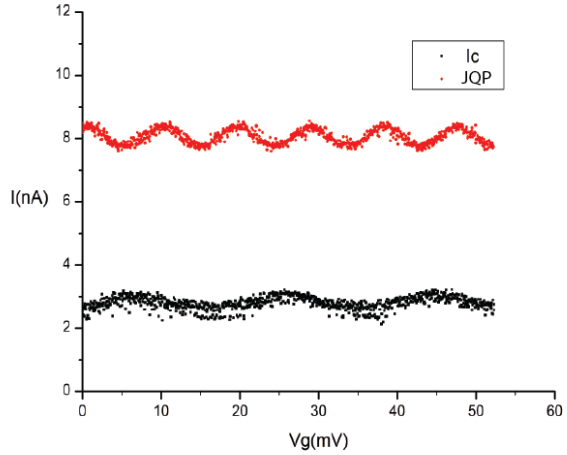


**Figure 6.22.** Gate modulation of $I_c$ and JQP at T = $\sim$ 60 K.

Figure 6.23 shows the flux-biasing modulation of both the supercurrent branch and JQP branch at zero gate voltage, demonstrating the expected periodicities. The critical current of the 'tunable' junction (dc SQUID) is $\Phi_0$ periodic with the magnetic flux through its loop, which results in the $\Phi_0$ periodicity in the critical current and JQP current of the whole SCPT. The mutual inductance between the bias line and the SQUID is deduced[2] to be 17 pH, which is larger than the designed value 6.19 pH.

## 6.5 Conclusions.

We have not yet achieved the goals of the experiment. However we have finished building the whole experimental set up, which includes all the wiring inside the probe, the controlling circuits at room temperature and all the Labview programs sending signals and

[2]M = $\Phi_0/\Delta I$ = 2.0678 $\times$ $10^{-15}$ Wb / 0.121 $\times$ $10^{-3}$ A

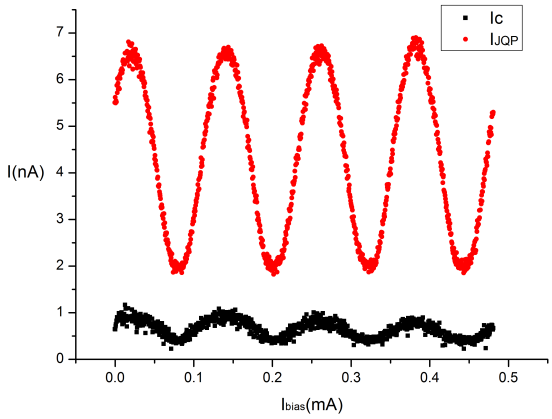


**Figure 6.23.** Flux-bias modulation of $I_c$ and JQP at T = $\sim 60K$.

recording data. We have observed the gate modulation and flux modulation of the SCPT, although the amplitude of the gate modulation effect is still quite small (0.5 nA) compared to the results in the literature (3 nA). This is partly due to the suppression of the critical current.

Our next goal is to observe the Shapiro steps and once we reach this point, we expect to observe the doubling of the Shapiro-step spacing by carefully tuning the gate voltage and flux bias to the degeneracy point. There are two issues that need to be addressed — the suppression of the critical current and the absence of Shapiro steps. It is possible the $I_c$ suppression is due to the unwanted radiation leaking into the sample cell. To apply more filtering, we connected our homemade metal-powder filters [95] in series with the thermal coaxial cable. In addition, we suspected the low quality of the Al might also cause radiation leakage. We replaced the Al shielding can by a high-conductivity copper can. Instead of measuring a SCPT device, we measured the critical current of a single junction with size 100nm $\times$ 100nm. The improvement is obvious (Figure 6.24). The critical current of the junction is measured to be $\sim 14$ nA at 57 mK, which is comparable to the expected value[3]

[3] $I_c$ = 150 nA/cm$^2$ $\times$ (100nm)$^2$

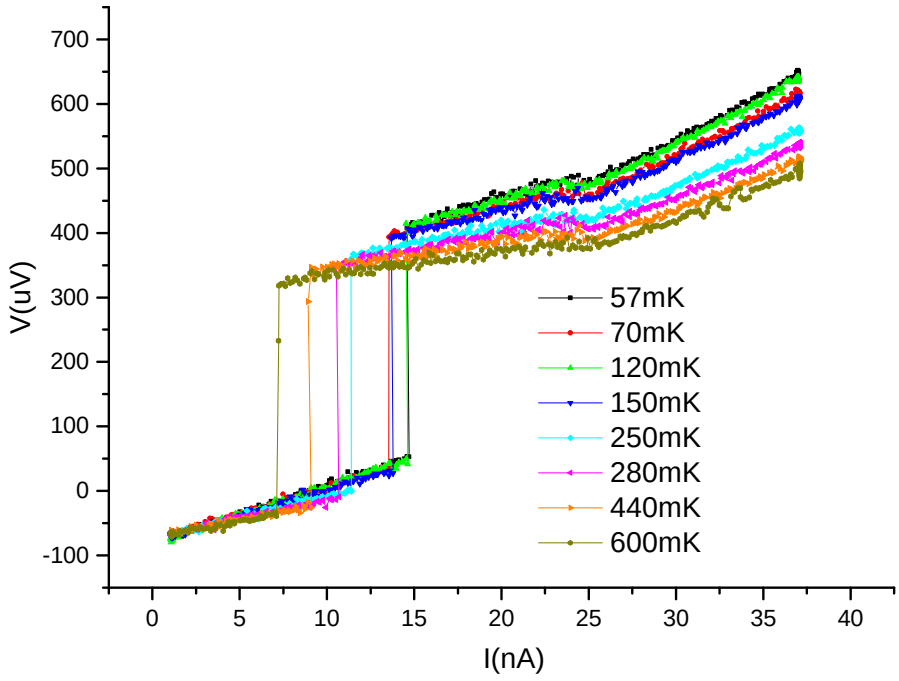


**Figure 6.24.** $I$-$V$ plot of a single junction at different temperature.

15 nA. The fact that the critical current decreases with increasing temperature suggests that the heating effect can be excluded from the sources of the current suppression.

To address the issue of detecting the Shapiro steps, we replaced the antenna by a current loop on a circuit board (Figure 6.25): the oscillating current is flowing right beneath the Josephson junction. Instead of a capacitive coupling by the antenna, an inductive coupling is implemented to ensure a stronger coupling. The improvement is apparent. When the single junction is radiated by microwaves of $f = 13.7$ GHz during current sweeping, Shapiro steps show up. As illustrated in Figure 6.26, higher-order Shapiro steps show up as the radiation power increases. We can clearly see one step at input power of 5 dBm, two steps at 10 dBm and the third one starts to show up at 15 dBm. The gap between neighboring steps agrees well with the calculated value: $\Delta V = \frac{\hbar\omega}{2e} = 29$ μV.

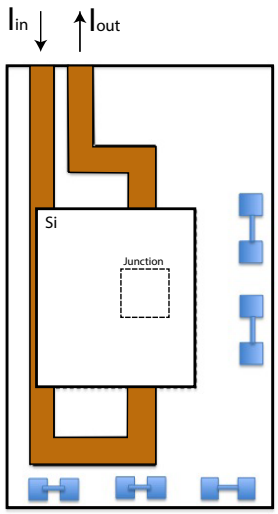


**Figure 6.25.** New design of the chipboard: Microwave current line made out of copper is running right beneath the Si chip where the junction is located.

At this point, both a significant increase of critical current and Shapiro steps had been achieved for a single junction. When replacing the single junction with the SCPT, however, the critical current was largely suppressed to below 5 nA. This made us doubt whether the measurement environment is really improved. At such a low critical current, no Shapiro steps were observed. The suppression of the critical current may due to the charge noise on the island between the two junctions. The flux control line may also introduce radiation leakage and the gate lead can bring down low frequency noises. Currently we haven't resolved the issue of critical-current suppression.

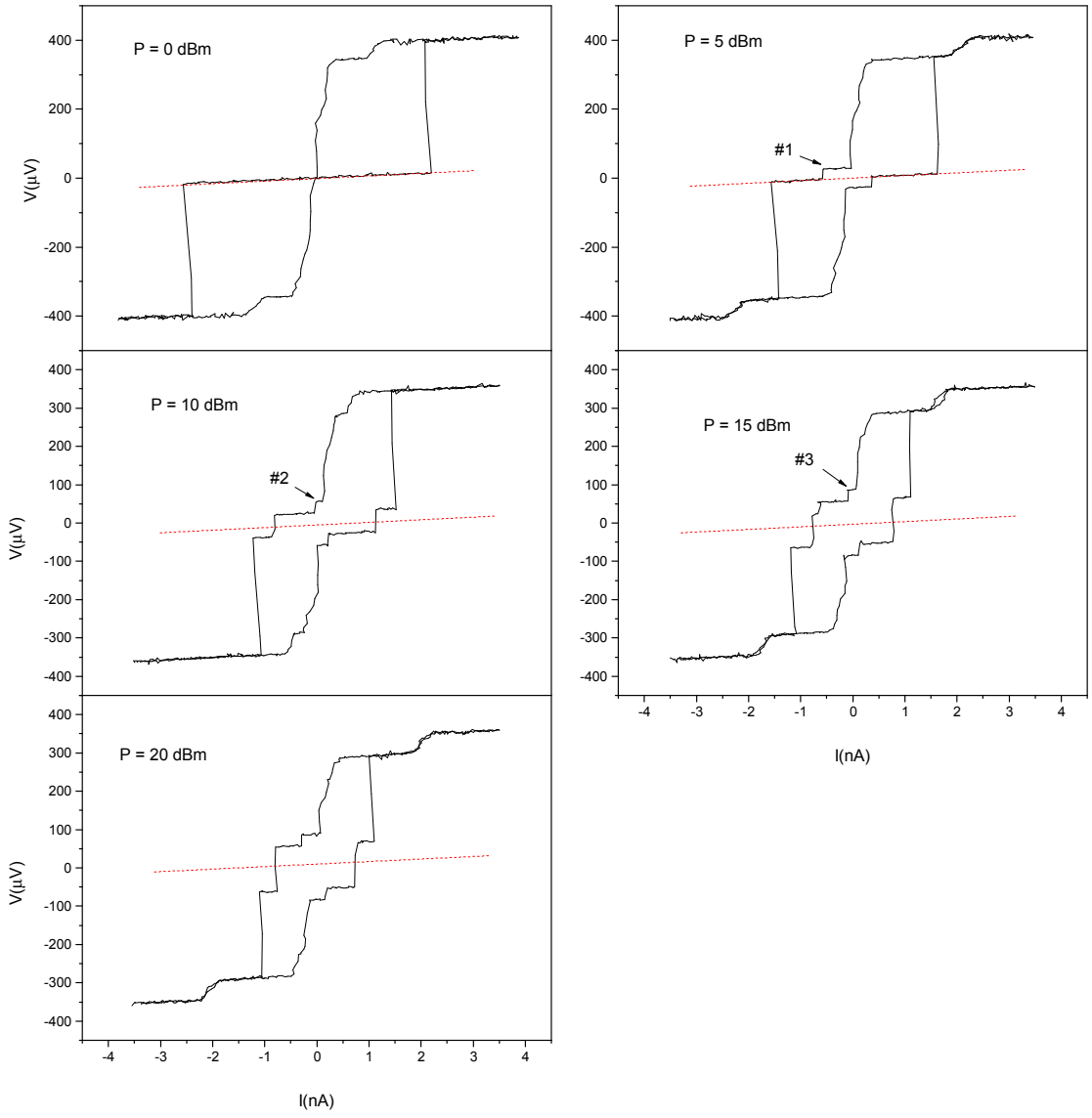


**Figure 6.26.** Observation of Shapiro steps of a single junction at $f = 13.7$ GHz with various levels of radiation power. The red lines roughly corresponding to the supercurrent branch at low power. The finite slope of the red line is attributed to the Cu leads inside the can which are in series with the device.

# CHAPTER 7

# CONCLUDING REMARKS

This dissertation is focused on the effort we have made in studying quantum phenomena in the single-molecule magnets and the single Cooper-pair transistor.

From Chapter 2 to Chapter 5, I presented the results obtained from the studies on the single-molecule magnet $Ni_4$. Current progress in the coupling of the single molecule to the superconducting thin-film resonator was first discussed. We identified the source of the degrading of the on-chip resonator to be magnetic-flux trapping. To minimize the flux penetration effect, we developed a gear mechanism that enables fine control of the orientation of the resonator so that the flux trapping introduced by the perpendicular field component can be suppressed. By careful alignment, the resonator quality can be maintained up to a field of 2000 Oe. We expect a even higher workable field by decreasing the thickness of the resonator (50 nm). However, we haven't detected the coupling of the resonator to the molecular spins so far. Since the simulation shows that only spins within a few microns above the surface of the resonator can see an appreciable field from the transmission line, we may need to come up with better strategies to attach the sample to the resonator surface.

In the experiment that couples the molecular magnet to the cylindrical cavity, we successfully observed highly forbidden transitions of the projection states of the magnetic moment. These transitions are assisted by the tunneling between states in different potential wells and demonstrate a reversal of the magnetic spin orientation. These transitions might find application in implementing Grover's algorithm, where transitions among numerous states are a prerequisite. Our next step is to study the coherence time of these transitions. Since dipolar interactions are the major source of decoherence in SMMs, dilution of $Ni_4$ in

a crystal can be achieved by cocrystallizating it with the diamagnetic analog $Zn_4$. Through this method we expect to see an improvement of $T_2$.

In a separate experiment on a superconducting circuit, we are working on a single Cooper-pair transistor where flux tunneling through the Josephson junction is manifested by a phase change across the junction. Simulations show that we could see the period of the Shapiro steps in the IV curve of the SCPT double when the flux tunneling through the two junctions is suppressed by interference. We've made great progress in eliminating the radiation noise and a critical current of 15 nA is achieved for a single Josephson junction. By applying a different strategy to couple the microwave to the device, Shapiro steps are also detected for a single junction. When turning to the single Cooper-pair transistor, the critical current dropped to below 5 nA and we are not be able to observe the Shapiro steps with such a low critical current. Besides the low critical current, we also observed the gate modulation and magnetic flux modulation of the critical current, which is a first step towards controlling flux tunneling. More study on the source of the suppression of the critical current of the SCPT is our next research direction. The suppression of critical current could either be due to the asymmetry of the SCPT or the introduction of more feed-in electrical lines, e.g. the gate- and flux-control ports. The first issue can be addressed by carefully adjusting the flux of the tunable junction in the SCPT. For the second issue, we don't have a feasible solution for now, but coming up with better filtering strategies is our next goal.

# APPENDIX A

# RECIPE FOR $Ni_4$ SYNTHESIS

(Recipe provided by Rafael Cassaro in the Chemistry Department at University of Massachusetts )

All reagents and solvents were purchased from commercial sources and used without further purification. The synthesis procedure is as follows: To a solution of $NiCl_2.4H_2O$ (0.475 g,2 mmol), 2-hydroxymethylpyridine (hmpH) (0.218 g, 2 mmol) dissolved in 15 mL of methanol was added a solution of NaOMe (0.108 g, 2 mmol) dissolved in 2 mL of methanol. The reaction medium was refluxed for 30 min. The resulting solution was filtered when it was still hot, and green crystals were obtained from the solution after cooling slowly to room temperature. The crystallization was obtained dissolving these crystals in a mixture of 5 g of 3,3-dimethyl-1-butanol (dmb) and 6 mL of dichloromethane. Green crystals were obtained by keeping the solution at room temperature for two days. The unit cell and face index were obtained using a Bruker Kappa-CCD diffractometer.

# APPENDIX B

# MATLAB SCRIPTS

loadsys.m: This function sets up the Hamiltonian using different models as input into the Pepper function in Easyspin.

```
% Set up molecule parameters needed in Easyspin.
% model specify different models we used in simulation.
% Gs,GB: Giant spin model, treat the whole molecule as a S=4 spin
function Sys = loadsys(model,T,para,gx,gz)
    if T == 1.8
        cH = 15;
    else
        cH = 30;
    end

    gy = gx;


    if model == 'GB'  % Hamiltonian in terms of extended Stevens ...
       operators
          d = para(1);
          B40 = para(2);
          B44 = para(3);
          B60 = para(4);
          B62 = para(5);
        Sys = struct('S',4,'g',[gx,gy,gz]);
        Sys.B2 = -(d/3)*10^3;
        Sys.B4 = [B44*10^3,0,0,0,-B40*10^3 ,0,0,0,0];
        Sys.B6 = [0,0,0,0,0,0,B60*10^3,0,B62*10^3,0,0,0,0];
        Sys.HStrain = cH *[100 100 100];

    elseif model == 'Gs'  % Hamiltonian in terms of anisotropy ...
       terms.
          d = para(1);
          c = para(2);
          b = para(3);
          h = para(4);
        Sys = struct('S',4,'g',[gx,gy,gz]);
        Sys.B2 = -(d/3+575*b/105+1807*h/21)*10^3;
        Sys.B4 = [2*10^3*c,0,0,0,(-b/35-53*h/77)*10^3 ,0,0,0,0];
```

```
        Sys.B6 = [0,0,0,0,0,0,-h/231*10^3,0,0,0,0,0,0];
        Sys.HStrain = cH *[100 100 100];
    end
end
```

loadexp.m: This function loads the experiment setup as input into the Pepper function in Easyspin

```
% Set up experimental parameters needed in Easyspin.
function Exp = loadexp(fmw, Bmin, Bmax,theta,phi,psi,T)
    Exp.mwFreq = fmw;  %115.54
    Exp.Range =[Bmin Bmax];
    Exp.Harmonic = 0;
    Exp.Mode = 'perpendicular';
    angle_matrix = [ones(length(theta),1)*phi/180*pi theta/180*pi ...
       ones(length(theta),1)*psi/180*pi];
    Exp.CrystalOrientation = [angle_matrix];
    Exp.Temperature = T;
    Exp.nPoints = Bmax;
end
```

HtoB: This function converts $\{\mathrm{H}, \theta_H\}$ in the experiment setup into $\{\mathrm{B}, \theta\}$ considering the dipolar effect.

```
%  This function conver [H,theta_H] into [B,theta_B] based on the ...
    relation:
%  H = B-4*pi*f*M.  f is in the order of unity, H_induc is ...
    inductive
%  field modification.

%  Input H: single value, thetaH single value
%        H: n*m ,   thetaH n*1 , phi n*1
function [B, thetaB, phiB] = HtoB(H,thetaH,phi,Tmk,f,H_induc)
load('Magnetization'); %Load the M vs H relation calculated.
if Tmk == 1800
    Mx = Mx_low';
    Mz = Mz_low';
    My = My_low';
else
    Mx = Mx_high';
    Mz = Mz_high';
    My = My_high';
end

Bx = Blist';
By = Blist';
```

```
Bz = Blist';

Mx(Mx<1e-10) = 0;
My(My<1e-10) = 0;
Mz(Mz<1e-10) = 0;

Hx = Bx - Mx*f;
Hy = By - My*f;
Hz = By - Mz*f;

% Calculate Hx,Hy,Hz
H_after_induc = H - H_induc;
thetaH = repmat(thetaH,1,size(H,2));
phi = repmat(phi,1,size(H,2));
Hxdata = sin(thetaH*pi/180).*H_after_induc.*cos(phi*pi/180);
Hydata = sin(thetaH*pi/180).*H_after_induc.*sin(phi*pi/180);
Hzdata = cos(thetaH*pi/180).*H_after_induc;

% Get Bx, By, Bz through interpolation.
Bxdata = interp1(Hx,Bx,Hxdata);
Bydata = interp1(Hy,By,Hydata);
Bzdata = interp1(Hz,Bz,Hzdata);

% Calculate B & theta_B of data
B = sqrt(Bxdata.^2+Bydata.^2 +Bzdata.^2);
Theta_B_data_cos =  Bzdata./B;
Theta_B_data_tan =  Bydata./Bxdata;
thetaB = acos(Theta_B_data_cos)/pi*180;
phiB = atan(Theta_B_data_tan)/pi*180;
phiB(thetaB == 0) = 0;
end
```

LoadPar.m: This function loads the optimized parameters (anisotropy paramters, **g** , $\alpha$, $\theta_H$, $\phi_H$ ) to update MvsB, draw spectrum, etc.

```
function [d1 c1 b1 h1 d c b h f f1 gx  gz theta phi1 phi2 phi3] = ...
    LoadPar()
    % the optimatized parameters
    parlist = [15.126713, 0.005326, 0.135751, 0.000000,15.551456, 0...
        .006446, 0.137871,0.000000, 0.335384, 0.096909, 2.220401, 2...
        .157266, 15.220975,26.581967, 29.779073, 31.930342, 38...
        .615929, 41.038095,44.628856, 46.801521,50.880062,55.640962...
        ,57.177235,24.997268,4.926289,42.837219];
    d1 = parlist(1);
    c1 = parlist(2);
    b1 = parlist(3);
    h1 = parlist(4);
    d  = parlist(5);
    c  = parlist(6);
    b  = parlist(7);
```

```
    h  = parlist(8);
    f  = parlist(9);
    f1 = parlist(10);
    gx = parlist(11);
    gz = parlist(12);
    theta = [ parlist(13) parlist(14) parlist(15) parlist(16) ...
        parlist(17) parlist(18) parlist(19) parlist(20) parlist(21) ...
        parlist(22) parlist(23) 20] ;
    phi1 = parlist(24);
    phi2 = parlist(25);
    phi3 = parlist(26);
end
```

MvsB.m: This script generates the magnetization as a function of B along $x, y, z$ of the crystal. The result is saved in magnetization.mat which is loaded in the HtoB.m to account for the dipolar effect.

```
% This script simulates the magnetization as a function of H ...
    field.
clear;
s = 4;
hbar = 1.054571628*10^-34;
h = hbar*2*pi;
kB = 1.3806503*10^-23;

a = repmat(-4:1:4,9,1);
sz = eye(9).*a;  % Sz matrix

% Sx matrix
for i = -s:s
    for j = -s:s
        sx(i+5,j+5) = 0.5*( sqrt((s-i)*(s+i+1))*(j==i+1) + sqrt((s...
            +i)*(s-i+1))*(j==i-1));
    end
end

% Sy matrix
for i = -s:s
    for j = -s:s
        sy(i+5,j+5) = 0.5/complex(0,1)*( sqrt((s-i)*(s+i+1))*(j==i...
            +1) - sqrt((s+i)*(s-i+1))*(j==i-1));
    end
end

[d1 c1 b1 h1 d c b a f f1 gx gz theta phi1 phi2 phi3] = LoadPar();
para = [d c b a];
T = 1.8;
model = 'Gs';
fprintf('T = %f\n', T);
```

```
% calculate Mz as a function of B at 1.8 K
theta = 0;
phi=0;
psi = 0;
fprintf('theta = %f,phi = %f\n', theta, phi);
Sys = loadsys(model,T,para,gx , gz);
Blist = 0:100:50000;
for i = 1:length(Blist)
    B = Blist(i)/10;
    Bvec = [B*sin(theta/180*pi)*cos(phi/180*pi), B*sin(theta/180*...
       pi)*sin(phi/180*pi), B*cos(theta/180*pi)];
    H = sham(Sys, Bvec);
    [V,E] = eig(H);
    energy = diag(E);
    Boltz  = exp(-h*energy*10^6/kB/T);
    Boltznorm = Boltz/sum(Boltz);
    for j = 1:9
        sz_expect(j) = real(V(:,j)'*sz * V(:,j));
    end
    Mz_low(i) = 9.27*4*pi/216*10^3*sz_expect*Boltznorm*gz/2;
end
% calculate Mx as a function of B at 1.8 K
theta = 90;
phi=0;
psi = 0;
fprintf('theta = %f,phi = %f\n', theta, phi);
Sys = loadsys(model,T,para,gx,gz);
Blist = 0:100:50000;
for i = 1:length(Blist)
    B = Blist(i)/10;
    Bvec = [B*sin(theta/180*pi)*cos(phi/180*pi), B*sin(theta/180*...
       pi)*sin(phi/180*pi), B*cos(theta/180*pi)];
    H = sham(Sys, Bvec);
    [V,E] = eig(H);
    energy = diag(E);
    Boltz  = exp(-h*energy*10^6/kB/T);
    Boltznorm = Boltz/sum(Boltz);

    for j = 1:9
        sx_expect(j) = real(V(:,j)'*sx * V(:,j));
    end
    Mx_low(i) = -9.27*4*pi/216*10^3*sx_expect*Boltznorm*gx/2;
end
% calculate My as a function of B at 1.8 K
theta = 90;
phi= 90;
psi = 0;
fprintf('theta = %f,phi = %f\n', theta, phi);
Sys = loadsys(model,T,para,gx,gz);
Blist = 0:100:50000;
for i = 1:length(Blist)
    B = Blist(i)/10;
    Bvec = [B*sin(theta/180*pi)*cos(phi/180*pi), B*sin(theta/180*...
       pi)*sin(phi/180*pi), B*cos(theta/180*pi)];
```

```
    H = sham(Sys, Bvec);
    [V,E] = eig(H);
    energy = diag(E);
    Boltz  = exp(-h*energy*10^6/kB/T);
    Boltznorm = Boltz/sum(Boltz);
    for j = 1:9
        sy_expect(j) = real(V(:,j)'*sy * V(:,j));
    end
    My_low(i) = -9.27*4*pi/216*10^3*sy_expect*Boltznorm*gx/2;
end

T = 9;
model = 'Gs';
% calculate Mz as a function of B at 9 K
theta = 0;
phi = 0;
psi = 0;
fprintf('T = %f\n', T);
fprintf('theta = %f,phi = %f\n', theta, phi);

Sys = loadsys(model,T,para,gx,gz);
Blist = 0:100:50000;
for i = 1:length(Blist)
    B = Blist(i)/10;
    Bvec = [B*sin(theta/180*pi)*cos(phi/180*pi), B*sin(theta/180*...
       pi)*sin(phi/180*pi), B*cos(theta/180*pi)];
    H = sham(Sys, Bvec);
    [V,E] = eig(H);
    energy = diag(E);
    Boltz  = exp(-h*energy*10^6/kB/T);
    Boltznorm = Boltz/sum(Boltz);
    for j = 1:9
        sz_expect(j) = real(V(:,j)'*sz * V(:,j));
    end
    Mz_high(i) = 9.27*4*pi/216*10^3*sz_expect*Boltznorm*gz/2;
end

% calculate Mx as a function of B at 9 K
theta = 90;
phi = 0;
psi = 0;
fprintf('theta = %f,phi = %f\n', theta, phi);

Sys = loadsys(model,T,para,gx,gz);
Blist = 0:100:50000;
for i = 1:length(Blist)
    B = Blist(i)/10;
    Bvec = [B*sin(theta/180*pi)*cos(phi/180*pi), B*sin(theta/180*...
       pi)*sin(phi/180*pi), B*cos(theta/180*pi)];
    H = sham(Sys, Bvec);
    [V,E] = eig(H);
    energy = diag(E);
    Boltz  = exp(-h*energy*10^6/kB/T);
    Boltznorm = Boltz/sum(Boltz);
```

```
133
134     for j = 1:9
135         sx_expect(j) = real(V(:,j)'*sx * V(:,j));
136     end
137     Mx_high(i) = -9.27*4*pi/216*10^3*sx_expect*Boltznorm*gx/2;
138 end
139
140 % calculate My as a function of B at 9 K
141 theta = 90;
142 phi= 90;
143 psi = 0;
144 fprintf('theta = %f,phi = %f\n', theta, phi);
145 Sys = loadsys(model,T,para,gx,gz);
146 Blist = 0:100:50000;
147 for i = 1:length(Blist)
148     B = Blist(i)/10;
149     Bvec = [B*sin(theta/180*pi)*cos(phi/180*pi), B*sin(theta/180*...
        pi)*sin(phi/180*pi), B*cos(theta/180*pi)];
150     H = sham(Sys, Bvec);
151     [V,E] = eig(H);
152     energy = diag(E);
153     Boltz  = exp(-h*energy*10^6/kB/T);
154     Boltznorm = Boltz/sum(Boltz);
155     for j = 1:9
156         sy_expect(j) = real(V(:,j)'*sy * V(:,j));
157     end
158     My_high(i) = -9.27*4*pi/216*10^3*sy_expect*Boltznorm*gx/2;
159 end
160 save('Magnetization','Blist','Mx_low','Mz_low','Mx_high','Mz_high'...
    ,'My_low','My_high');
```

optimize_peak.m: This script runs the optimization using fmincon function in Matlab to fit the spectrum (detailed discussion in section 5.3.2).

```
1  clear;
2  apple =  @(x)peak_fit(x(1), x(2),x(3),x(4),x(5),x(6),x(7),x(8),x...
       (9),x(10),x(11),x(12),x(13),x(14),x(15),x(16),x(17),x(18),x(19)...
       ,x(20),x(21),x(22),x(23),x(24),x(25),x(26));%,x(4));
3  pre = strcat(datestr(clock),'0.005326 c2=0.006445');
4  % c1 and c2 are determined directly from zero filed transition ...
       between
5  % |2>+|-2> and |2>-|-2> states
6  c1 = 0.005326;
7  c2 = 0.006445;
8  % set the parameter fitting boundary
9   lb = [15.0, c1,   0,  0, 15.4, c2,   0,  0,   0,   0, 2.1, 2.1, ...
        10, 25, 28, 30, 37, 40, 43, 43, 45, 50, 55, 25.000036, 0, 0];
10  ub = [15.4, c1, 0.2,  0,  16 , c2, 0.2,  0, 0.6, 0.3, 2.3, 2.3, ...
        27, 33, 37, 37, 45, 46, 50, 52, 56, 58, 59, 25.000036,45,45];
11
```

```
% set the initial guess
init = [15.179759, 0.005326, 0.133285, 0.000000,15.599936, 0...
    .006445, 0.135603,0.000000, 0.326304, 0.089922, 2.219813, 2...
    .161869, 15.658786,26.791408, 29.967666, 32.103702, 38.751116, ...
    41.199593,44.756287, 46.918787,50.959339,55.688469,57.224512,25...
    .000036,4.980550,42.938240];

nonlcon = @mycon;
options = optimoptions(@fmincon,'TolCon',1e-10,'TolFun',1e-10,'...
    PlotFcns',@optimplotfval);
options.Algorithm = 'active-set';
[x,fval,flag,output,lambda,grad,hessian]  = fmincon(apple , init...
    ,[],[],[],[],lb,ub,[],options);
```

peak_fit.m: This script calculates the $\chi^2$ by comparing the peak position and peak area of the simulated spectrum to the data (detailed discussion in section 5.3.2).

```
 function [chi] = peak_fit(d1,c1,b1,a1,d2,c2,b2,a2,f,f1,gx,gz, t1,...
     t2 ,t3, t4, t5, t6,t7 ,t8, t9, t10, t11, phi1, phi2, phi3)
T = 1.8;
fmw = 115.54;
psi = 90;
Bmax = 4000;
Opt.Transitions = [2 4 ; 2 5 ; 2 3 ; 3 5];
Opt.Threshold = 0;
fprintf('[phi1 phi2 phi3] = %f %f %f \n', phi1, phi2, phi3);
fprintf('[d1 c1 b1 h1] =  %f %f %f %f\n', d1, c1, b1,a1);
fprintf('[d c b h f f1 gx gz] =  %f %f %f %f %f %f %f\n', d2, c2, ...
    b2, a2, f,gx, gz);
fprintf('thetas: %f, %f, %f, %f, %f, %f, %f, %f, %f, %f, %f  \n', ...
    t1, t2 ,t3, t4, t5, t6,t7 ,t8, t9, t10, t11);
fprintf('peak_fit(%f, %f, %f, %f,%f, %f, %f,%f, %f, %f, %f, %f, %f...
    ,%f, %f, %f, %f, %f,%f, %f,%f,%f,%f,%f,%f,%f) \n', d1, c1, b1,...
    a1, d2, c2, b2,a2,f,f1,gx,gz,t1, t2 ,t3, t4, t5, t6,t7 ,t8, t9,...
     t10, t11,phi1,phi2,phi3);
fprintf('-----------------------------------------------------\n...
    ');
chi_lowfreq = search_db_lowf(d1,c1,b1,a1,d2,c2,b2,a2,f,f1,gx,gz);
chi_highfreq_highT = search_db_highf_highT(d1,c1,b1,a1,d2,c2,b2,a2...
    ,f,gx,gz, t1, t2 ,t3, t4, t5, t6,t7 ,t8, t9, t10, t11, phi1, ...
    phi2, phi3);
chi_highfreq_lowT = search_db_highf_lowT(d1,c1,b1,a1,d2,c2,b2,a2,f...
    ,gx,gz, t1, t2 ,t3, t4, t5, t6,t7 ,t8, t9, t10, t11, phi1, phi2...
    , phi3);
chi = (chi_highfreq_lowT + chi_highfreq_highT + chi_lowfreq)...
    /(22*12-25);
fprintf('-----------------------------------------------------\n...
    ');
fprintf('chi_lowfreq = %f chi_highF_highT = %f chi_highF_lowT = %f...
     \n',chi_lowfreq, chi_highfreq_highT,chi_highfreq_lowT);
```

```
fprintf('chi = %f\n', chi);
end
```

Peak_fit.m: This function calculates the $\chi^2$, which is minimized to obtain optimal fitting.

```
 function [chi] = peak_fit(d1,c1,b1,a1,d2,c2,b2,a2,f,f1,gx,gz, t1,...
     t2 ,t3, t4, t5, t6,t7 ,t8, t9, t10, t11, phi1, phi2, phi3)
T = 1.8;
fmw = 115.54;
psi = 90;
Bmax = 4000;
Opt.Transitions = [2 4 ; 2 5 ; 2 3 ; 3 5];
Opt.Threshold = 0;
fprintf('[phi1 phi2 phi3] = %f %f %f \n', phi1, phi2, phi3);
fprintf('[d1 c1 b1 h1] =  %f %f %f %f\n', d1, c1, b1,a1);
fprintf('[d c b h f f1 gx gz] =  %f %f %f %f %f %f %f\n', d2, c2, ...
   b2, a2, f,gx, gz);
fprintf('thetas: %f, %f, %f, %f, %f, %f, %f, %f, %f, %f, %f  \n', ...
   t1, t2 ,t3, t4, t5, t6,t7 ,t8, t9, t10, t11);
fprintf('peak_fit(%f, %f, %f, %f,%f, %f, %f,%f, %f, %f, %f, %f, %f...
   ,%f, %f, %f, %f, %f,%f, %f,%f,%f,%f,%f,%f,%f) \n', d1, c1, b1,...
   a1, d2, c2, b2,a2,f,f1,gx,gz,t1, t2 ,t3, t4, t5, t6,t7 ,t8, t9,...
    t10, t11,phi1,phi2,phi3);
fprintf('-------------------------------------------------------\n...
   ');
chi_lowfreq = search_db_lowf(d1,c1,b1,a1,d2,c2,b2,a2,f,f1,gx,gz);
chi_highfreq_highT = search_db_highf_highT(d1,c1,b1,a1,d2,c2,b2,a2...
   ,f,gx,gz, t1, t2 ,t3, t4, t5, t6,t7 ,t8, t9, t10, t11, phi1, ...
   phi2, phi3);
chi_highfreq_lowT = search_db_highf_lowT(d1,c1,b1,a1,d2,c2,b2,a2,f...
   ,gx,gz, t1, t2 ,t3, t4, t5, t6,t7 ,t8, t9, t10, t11, phi1, phi2...
   , phi3);
chi = (chi_highfreq_lowT + chi_highfreq_highT + chi_lowfreq)...
   /(22*12-25);
fprintf('-------------------------------------------------------\n...
   ');
fprintf('chi_lowfreq = %f chi_highF_highT = %f chi_highF_lowT = %f...
    \n',chi_lowfreq, chi_highfreq_highT,chi_highfreq_lowT);
fprintf('chi = %f\n', chi);

end
```

SzExpectedVsTheta.m : This script calculates $\Delta\langle S_z\rangle$ of the transitions of the second component as a function of $\theta$.

```
% Simulation of Δ<S_z> as a function of the angle
clear;
i = 1;
sz = eye(9).*repmat(-4:1:4,9,1);
model = 'Gs';
[d1 c1 b1 h1 d c b h f f1 gx gz theta phi1 phi2 phi3] = LoadPar();
para = [d c b h]; % anisotropy parameter for component 2
step = 0.1;
start = 0;
stop = 60;
for theta =start:step:stop
fprintf('theta = %f\n', theta);
phi = 43;
psi = 90;
Bmax=4000;
angles = [phi theta psi];
fmw = 115.54;
T = 1.8;
Exp = loadexp(fmw, 0, Bmax,theta,phi,psi,T);
Sys = loadsys(model,T,para,gx,gz);
Opt.Transitions = [2 4 ; 2 5 ; 2 3];
Opt.Threshold = 0;
[Pos,Amp,Wid,Trans,Grad] = resfields(Sys,Exp,Opt); % use the ...
    resfield function in Easyspin to get the interested transition ...
    info
index = [1 3 2 6];

for j = 1:4
B = Pos(index(j));
res_f(i,j) = B;
Bvec = [B*sin(theta/180*pi)*cos(phi/180*pi), B*sin(theta/180*pi)*...
    sin(phi/180*pi), B*cos(theta/180*pi)];
H = sham(Sys, Bvec);  % build the hamiltonian matrix using sham ...
    function
[V,E] = eig(H);
Vi = V(:,Trans(index(j),1));
Vf = V(:,Trans(index(j),2));
sz_expect_i(i,j) = real(Vi'*sz * Vi);
sz_expect_f(i,j) = real(Vf'*sz * Vf);

end
i = i+1;
end
theta = start:step:stop;
theta = theta';
sz_dif = abs(sz_expect_f - sz_expect_i);
forbid1 = sz_dif(:,2);
forbid2 = max(sz_dif(:,3),sz_dif(:,4));
figure
subplot(3,1,1)
plot(res_f(:,1), sz_dif(:,1),res_f(:,2), sz_dif(:,2),res_f(:,3), ...
    sz_dif(:,3),res_f(:,4), sz_dif(:,4)
subplot(3,1,2)
plot(theta, res_f)
```

```
subplot(3,1,3)
plot(theta, sz_dif)
```

SpectrumPlotBothT.m : This script plots the simulated and measured spectra at 1.8 K and 9 K.

```
clear;
[d1 c1 b1 h1 d c b h f f1 gx gz theta phi1 phi2 phi3] = LoadPar();
theta_index = 7;  %0-10

switch(theta_index)
   case 0
      phi = phi1
   case {1,2,3,4}
      phi = phi2
   case {5,6,7,8,9,10}
      phi = phi3
end


para1 = [d1 c1 b1 h1]; % anisotropy parameter for component 1
para2 = [d c b h]; % anisotropy parameter for component 2
f1 = f;
f2 = f1;
H_induc = 300.8;
load('Magnetization');

% Experiment setup
psi = 90;
chi_square = 0;
weight = 0.5;
Bmax=4000;
n = 20;
fmw = 115.54;
T = 1.8;

Tmk  = T*1000;
if Tmk == 1800
    gs =2;
else
    gs = 5;
end

theta1 = theta(theta_index+1);

[Hdata,Spcdata] = textread(strcat('theta',num2str(theta_index) ,'_...
   ',num2str(Tmk),'mk.txt'),'%f %f');

Mx = Mx_low';
Mz = Mz_low';
```

```
Bx = Blist';
Bz = Bx;
By = Bx;
My = Mx;

Mx(Mx<1e-10) = 0;
My(My<1e-10) = 0;
Mz(Mz<1e-10) = 0;

Hx = Bx - Mx*f2;
Hy = By - My*f2;
Hz = By - Mz*f1;
H_after_induc = Hdata-H_induc;
H_after_induc_1 = H_after_induc(H_after_induc>0);
Spcdata_1 = Spcdata(H_after_induc>0);
Hxdata = H_after_induc_1*sin(theta1*pi/180)*cos(phi*pi/180);
Hydata = H_after_induc_1*sin(theta1*pi/180)*sin(phi*pi/180);
Hzdata = H_after_induc_1*cos(theta1*pi/180);
Bxdata = interp1(Hx,Bx,Hxdata);
Bydata = interp1(Hy,By,Hydata);
Bzdata = interp1(Hz,Bz,Hzdata);

% actual B & theta_B of data
Bdata = sqrt(Bxdata.^2+Bydata.^2 +Bzdata.^2);
Theta_B_data_cos =  Bzdata./Bdata;
Theta_H_data_cos = Hzdata./(sqrt(Hxdata.^2+Hydata.^2+Hzdata.^2));

Bdata_mT = Bdata ./10;
Spcdata_1 = -Spcdata_1;

% simulation after
SBmax = 5000;

n =20; % number of field pieces
for i = 1:n
SBlow = (i-1)*SBmax/n +1; % 1-1000, 1001-2000, 2001-3000 ...
SBhigh =i*SBmax/n;
SBtheta = (SBlow + SBhigh)/2;
 if SBtheta < max(Bdata_mT)
   Stheta_real =  acos(interp1(Bdata_mT,Theta_B_data_cos,SBtheta))...
      *180/pi;
 else
    break
 end
fprintf('%f\n', Stheta_real)
%COMP1
Sys = loadsys('Gs',T,para1,gx,gz);
angles = [phi Stheta_real psi];
Exp = loadexp(fmw,0, SBmax,Stheta_real,phi, psi, T);
[B,spec1,trans] = pepper(Sys,Exp);  % B = 1:5000
sp1 = spec1(SBlow:SBhigh);
%COMP2
Sys1 = loadsys('Gs',T,para2,gx,gz);
```

```
Exp.CrystalOrientation = [phi/180*pi; Stheta_real/180*pi; psi/180*...
    pi];
[B,spec2,trans] = pepper(Sys1,Exp);
sp2 = spec2(SBlow:SBhigh);
sp(SBlow:SBhigh) = sp1 + sp2;
sp11(SBlow:SBhigh) = sp1;
sp22(SBlow:SBhigh) = sp2;
end

figure;
Spcdata_norm = (Spcdata_1-mean(Spcdata_1))/std(Spcdata_1);
subplot(4,1,1);
plot(Bdata_mT,Spcdata_norm);
axis tight
xlabel('B[mT]');
xlim([0 5000]);
ylim([-1 max(Spcdata_norm)]);
title(strcat('data: \phi = ', num2str(phi),  '^\circ ,\theta = ', ...
    num2str(theta1), '^\circ , T = ', num2str(T),'K'), 'fontsize', ...
    10);


sp_norm = (sp - mean(sp))/std(sp);
subplot(4,1,2);
plot(B(1:length(sp_norm)),sp_norm);
axis tight
xlabel('B[mT]');
xlim([0 5000]);
ylim([-1 max(sp_norm)]);

T = 9;
Tmk  = T*1000;
if Tmk == 1800
    gs =2;
else
    gs = 5;
end

theta1 = theta(theta_index+1);

% read realdata.
[Hdata,Spcdata] = textread(strcat('theta',num2str(theta_index) ,'_...
    ',num2str(Tmk),'mk.txt'),'%f %f');
Mx = Mx_high';
Mz = Mz_high';
Bx = Blist';
Bz = Bx;
By = Bx;
My = Mx;

Mx(Mx<1e-10) = 0;
My(My<1e-10) = 0;
Mz(Mz<1e-10) = 0;

```

```
Hx = Bx - Mx*f2;
Hy = By - My*f2;
Hz = By - Mz*f1;
H_after_induc = Hdata-H_induc;
H_after_induc_1 = H_after_induc(H_after_induc>0);
Spcdata_1 = Spcdata(H_after_induc>0);
Hxdata = H_after_induc_1*sin(theta1*pi/180)*cos(phi*pi/180);
Hydata = H_after_induc_1*sin(theta1*pi/180)*sin(phi*pi/180);
Hzdata = H_after_induc_1*cos(theta1*pi/180);
Bxdata = interp1(Hx,Bx,Hxdata);
Bydata = interp1(Hy,By,Hydata);
Bzdata = interp1(Hz,Bz,Hzdata);

% actual B & theta_B of data
Bdata = sqrt(Bxdata.^2+Bydata.^2 +Bzdata.^2);
Theta_B_data_cos =  Bzdata./Bdata;
Theta_H_data_cos = Hzdata./(sqrt(Hxdata.^2+Hydata.^2+Hzdata.^2));

Bdata_mT = Bdata ./10;
Spcdata_1 = -Spcdata_1;

% simulation after
SBmax = 5000;

n =50; % number of field pieces
for i = 1:n
SBlow = (i-1)*SBmax/n +1; % 1-1000, 1001-2000, 2001-3000 ...
SBhigh =i*SBmax/n;
SBtheta = (SBlow + SBhigh)/2;
 if SBtheta < max(Bdata_mT)
   Stheta_real =  acos(interp1(Bdata_mT,Theta_B_data_cos,SBtheta))...
       *180/pi;
 else
    break
 end
fprintf('%f\n', Stheta_real)
%COMP1
Sys = loadsys('Gs',T,para1,gx,gz);
angles = [phi Stheta_real psi];
Exp = loadexp(fmw,0, SBmax,Stheta_real,phi, psi, T);
[B,spec1,trans] = pepper(Sys,Exp);  % B = 1:5000
sp1 = spec1(SBlow:SBhigh);
%COMP2
Sys1 = loadsys('Gs',T,para2,gx,gz);
Exp.CrystalOrientation = [phi/180*pi; Stheta_real/180*pi; psi/180*...
    pi];
[B,spec2,trans] = pepper(Sys1,Exp);
sp2 = spec2(SBlow:SBhigh);
sp(SBlow:SBhigh) = sp1 + sp2;
sp11(SBlow:SBhigh) = sp1;
sp22(SBlow:SBhigh) = sp2;
end

Spcdata_norm = (Spcdata_1-mean(Spcdata_1))/std(Spcdata_1);
```

```
198 subplot(4,1,3);
199 plot(Bdata_mT,Spcdata_norm);
200 axis tight
201 xlabel('B[mT]');
202 xlim([0 5000]);
203 ylim([min(Spcdata_norm) max(Spcdata_norm)]);
204 title(strcat('data: \phi = ', num2str(phi),  '^\circ ,\theta = ', ...
       num2str(theta1), '^\circ , T = ', num2str(T),'K'), 'fontsize', ...
       10);
205
206 sp_norm = (sp - mean(sp))/std(sp);
207 subplot(4,1,4);
208 plot(B(1:length(sp_norm)),sp_norm);
209 axis tight
210 xlabel('B[mT]');
211 xlim([0 5000]);
212 ylim([-1 max(sp_norm)]);
213
214 figure;
215  levelsplot(Sys1,[phi/180*pi, theta1/180*pi, psi/180*pi],[0 Bmax...
       ],115.54);
216  xlabel('comp1');
```

# APPENDIX C

# COMPARISON OF MEASURED AND SIMULATED SPECTRUM

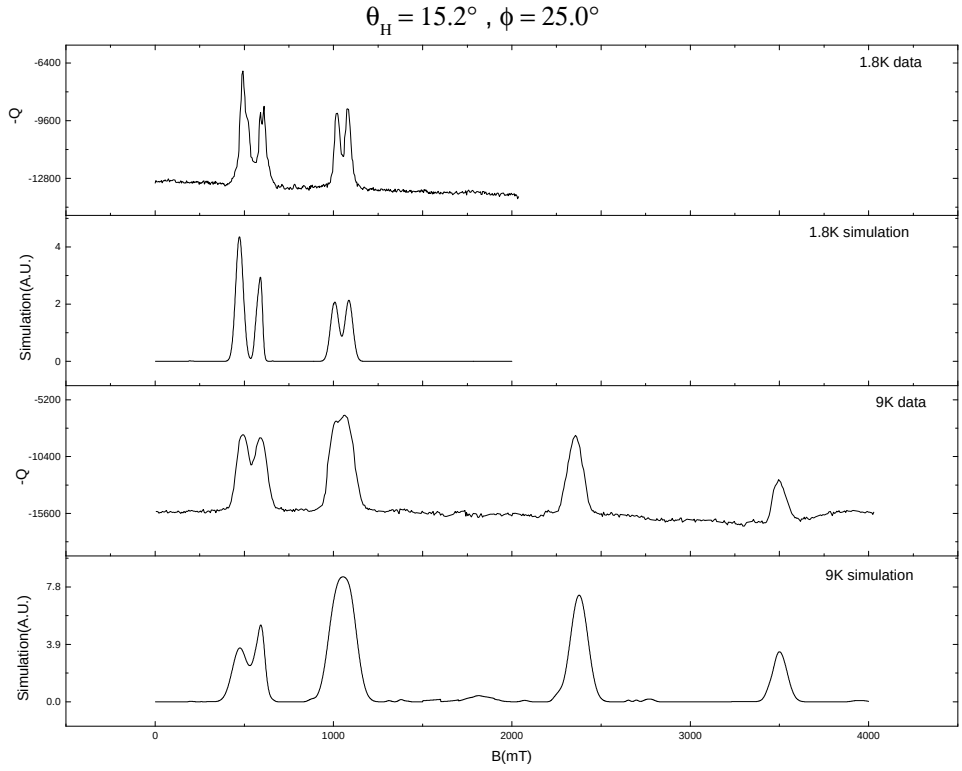


**Figure C.1.** Comparison of experimental and simulated spectra at 1.8 and 9 K, as indicated for $\theta_H = 15.2.0^\circ$ and $\phi_H = 25.0^\circ$.

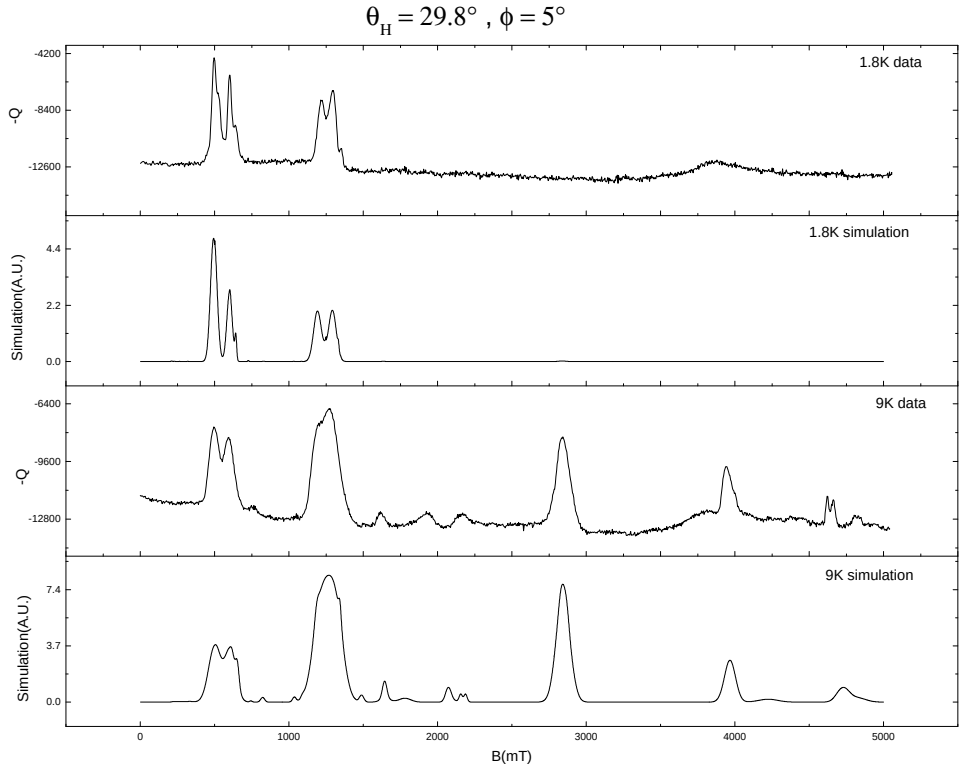


**Figure C.2.** Comparison of experimental and simulated spectra at 1.8 and 9 K, as indicated for $\theta_H = 29.8^\circ$ and $\phi_H = 5^\circ$.

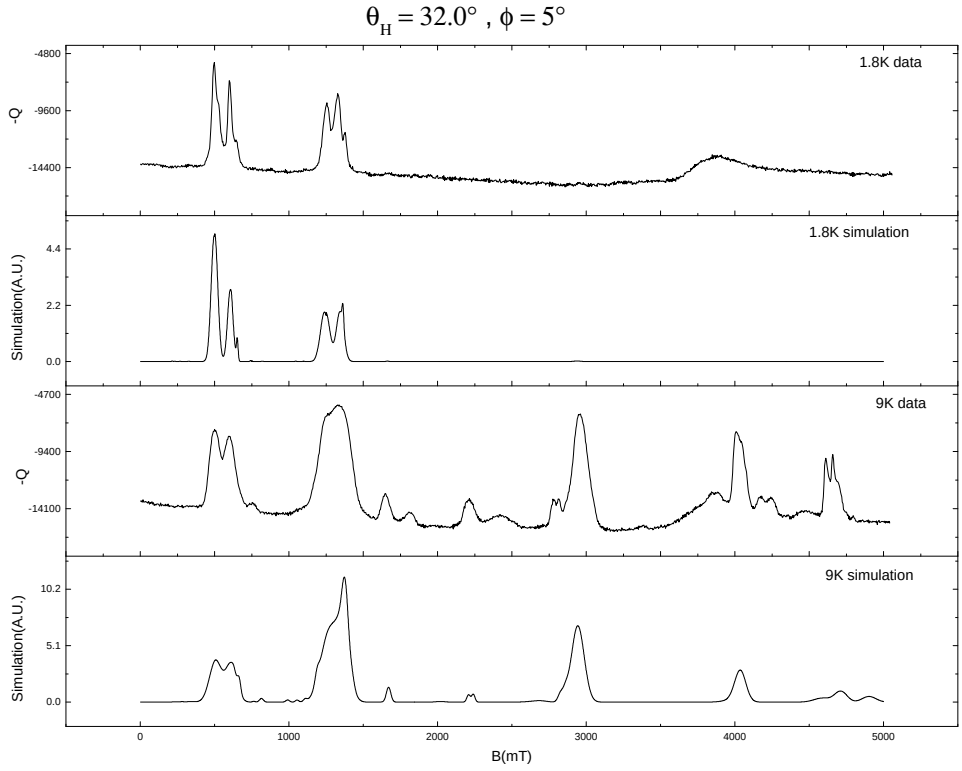


**Figure C.3.** Comparison of experimental and simulated spectra at 1.8 and 9 K, as indicated for $\theta_H = 32.0^\circ$ and $\phi_H = 5^\circ$.

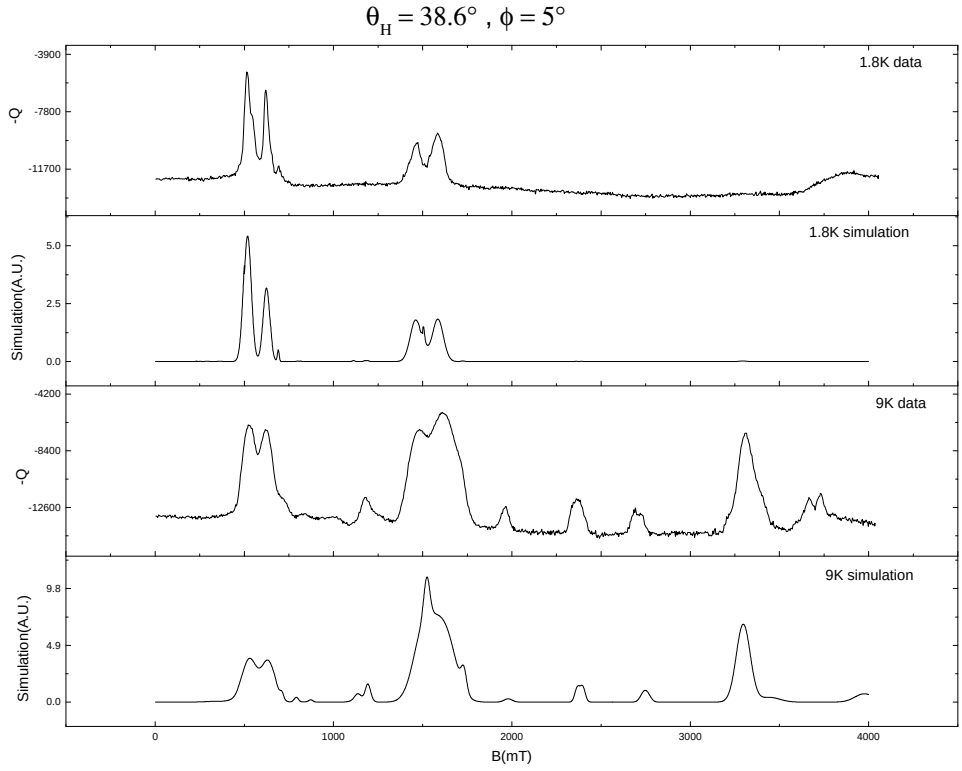


**Figure C.4.** Comparison of experimental and simulated spectra at 1.8 and 9 K, as indicated for $\theta_H = 38.6^\circ$ and $\phi_H = 5^\circ$.

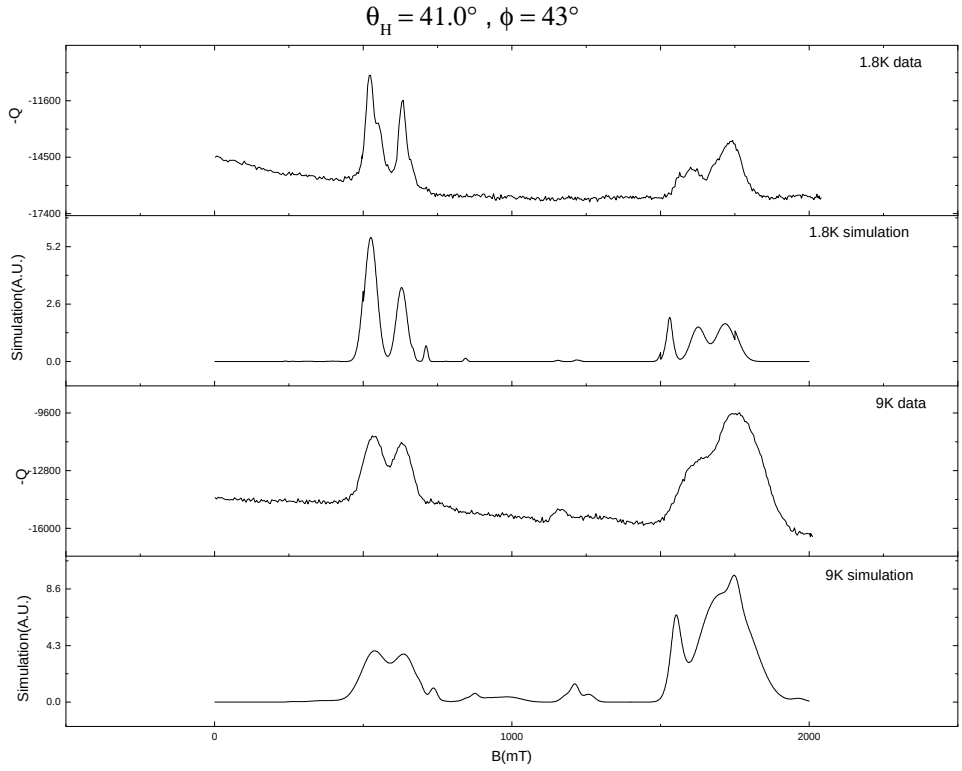


**Figure C.5.** Comparison of experimental and simulated spectra at 1.8 and 9 K, as indicated for $\theta_H = 41.0^\circ$ and $\phi_H = 43^\circ$.

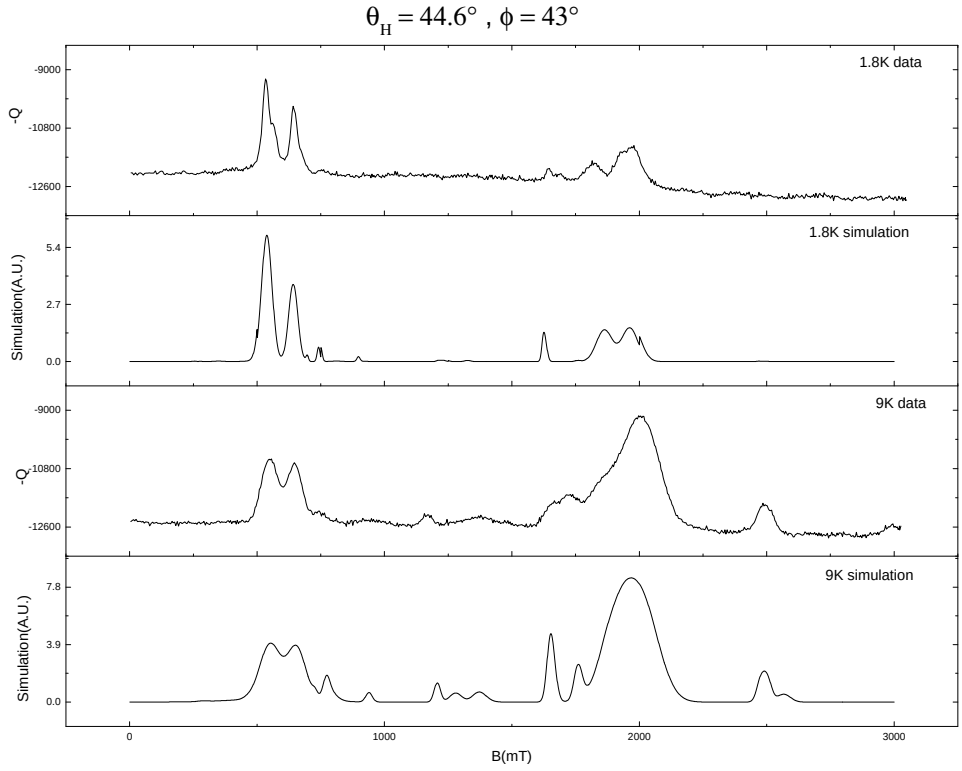


**Figure C.6.** Comparison of experimental and simulated spectra at 1.8 and 9 K, as indicated for $\theta_H = 44.6^\circ$ and $\phi_H = 43^\circ$.

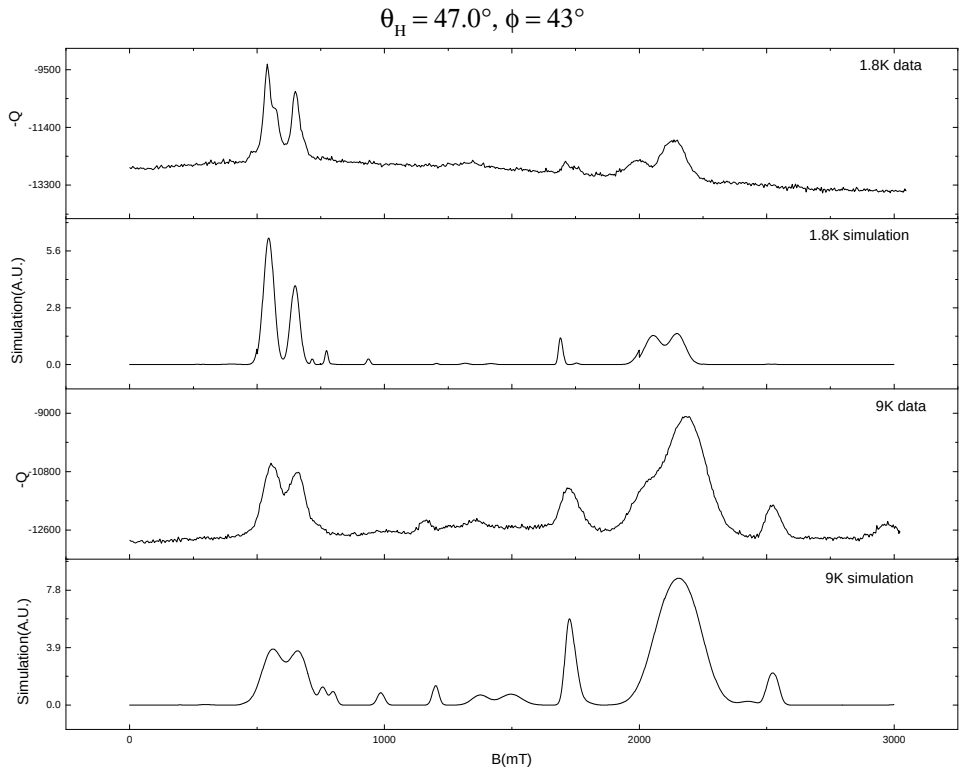


**Figure C.7.** Comparison of experimental and simulated spectra at 1.8 and 9 K, as indicated for $\theta_H = 47.0^\circ$ and $\phi_H = 43^\circ$.

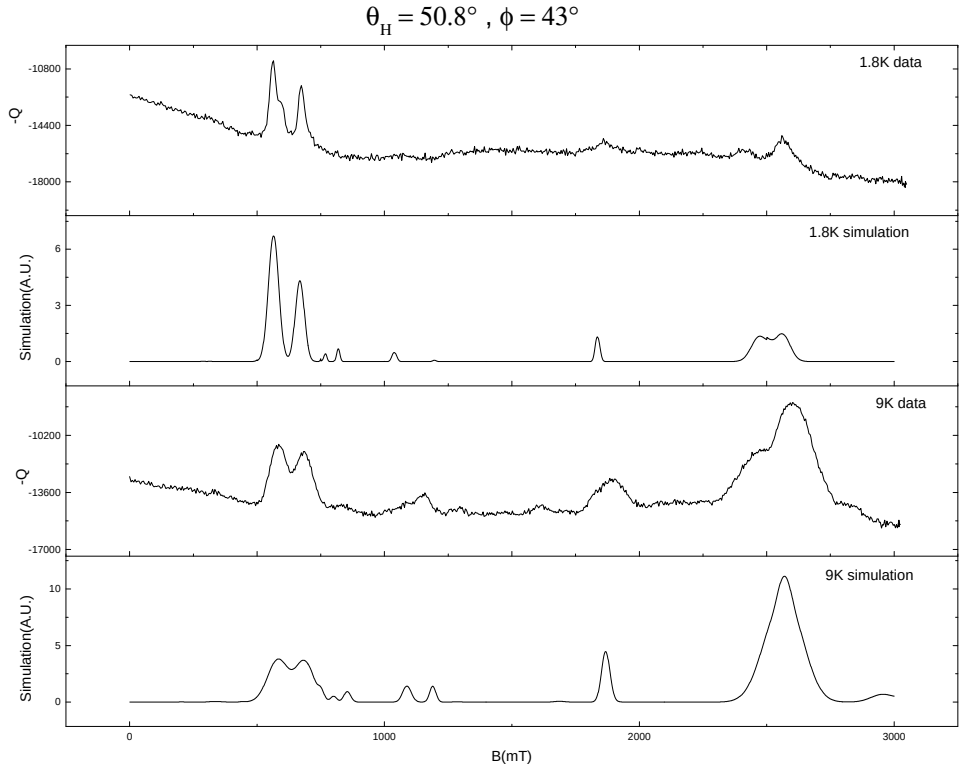


**Figure C.8.** Comparison of experimental and simulated spectra at 1.8 and 9 K, as indicated for $\theta_H = 50.8^\circ$ and $\phi_H = 43^\circ$.

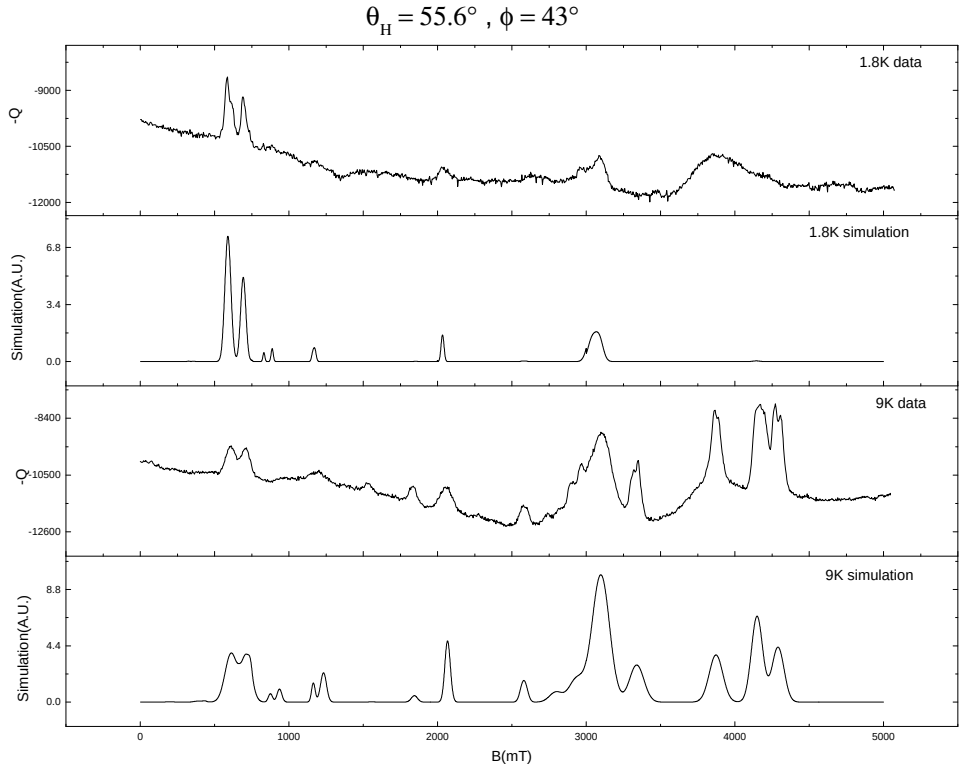


**Figure C.9.** Comparison of experimental and simulated spectra at 1.8 and 9 K, as indicated for $\theta_H = 55.6^\circ$ and $\phi_H = 43^\circ$.

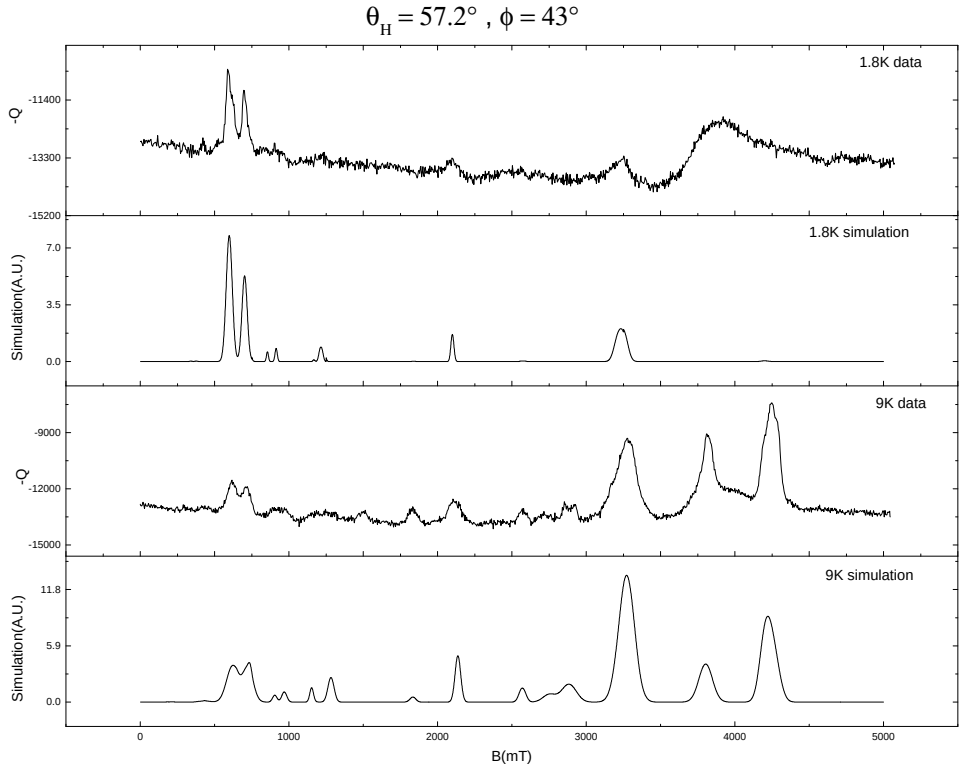


**Figure C.10.** Comparison of experimental and simulated spectra at 1.8 and 9 K, as indicated for $\theta_H = 57.2^\circ$ and $\phi_H = 43^\circ$.

# BIBLIOGRAPHY


[1] W. H. Zurek, "The Environment, Decoherence and the Transition from Quantum to Classical," in *Quantum Gravity and Cosmology*, vol. 1, p. 117, 1991.

[2] A. J. Leggett, "Macroscopic quantum systems and the quantum theory of measurement," *Progress of Theoretical Physics Supplement*, vol. 69, pp. 80–100, 1980.

[3] A. O. Caldeira and A. J. Leggett, "Influence of Dissipation on Quantum Tunneling in Macroscopic Systems," *Physical Review Letters*, vol. 46, no. 4, pp. 211–214, 1981.

[4] A. J. Leggett, "Schrödinger's cat and her laboratory cousins," *Contemporary Physics*, vol. 25, no. 6, pp. 583–598, 1984.

[5] A. J. Leggett, S. Chakravarty, A. T. Dorsey, M. P. Fisher, A. Garg, and W. Zwerger, "Dynamics of the dissipative two-state system," *Reviews of Modern Physics*, vol. 59, no. 1, p. 1, 1987.

[6] Y. Nakamura, Y. A. Pashkin, and J. S. Tsai, "Coherent control of macroscopic quantum states in a single-Cooper-pair box," *Nature*, vol. 398, no. 6730, pp. 786–788, 1999.

[7] J. R. Friedman, V. Patel, W. Chen, S. K. Tolpygo, and J. E. Lukens, "Quantum superposition of distinct macroscopic states," *Nature*, vol. 406, no. 6791, pp. 43–46, 2000.

[8] C. H. van der Wal, A. C. J. Ter Haar, F. K. Wilhelm, R. N. Schouten, C. Harmans, T. P. Orlando, S. Lloyd, and J. E. Mooij, "Quantum superposition of macroscopic persistent-current states," *Science*, vol. 290, no. 5492, pp. 773–777, 2000.

[9] D. Vion, A. Aassime, A. Cottet, P. Joyez, H. Pothier, C. Urbina, D. Esteve, and M. H. Devoret, "Manipulating the quantum state of an electrical circuit," *Science*, vol. 296, no. 5569, pp. 886–889, 2002.

[10] I. Chiorescu, Y. Nakamura, C. J. P. M. Harmans, and J. E. Mooij, "Coherent Quantum Dynamics of a Superconducting Flux Qubit," *Science*, vol. 299, no. 5614, pp. 1869–1871, 2003.

[11] J. R. Friedman, M. P. Sarachik, J. Tejada, and R. Ziolo, "Macroscopic Measurement of Resonant Magnetization Tunneling in High-Spin Molecules," *Physical Review Letters*, vol. 76, no. 20, pp. 3830–3833, 1996.

[12] J. M. Hernandez, X. X. Zhang, F. Luis, J. Bartolomé, J. Tejada, and R. Ziolo, "Field tuning of thermally activated magnetic quantum tunnelling in $Mn_{12}$- Ac molecules," *EPL (Europhysics Letters)*, vol. 35, no. 4, p. 301, 1996.

[13] L. Thomas, F. Lionti, R. Ballou, D. Gatteschi, R. Sessoli, and B. Barbara, "Macroscopic quantum tunnelling of magnetization in a single crystal of nanomagnets," *Nature*, vol. 383, no. 6596, pp. 145–147, 1996.

[14] B. Barbara, R. Giraud, W. Wernsdorfer, D. Mailly, P. Lejay, A. Tkachuk, and H. Suzuki, "Evidence for resonant magnetic tunneling of rare-earth ions: from insulating to metallic matrix," *Journal of Magnetism and Magnetic Materials*, vol. 272, pp. 1024–1029, 2004.

[15] N. Ishikawa, M. Sugita, and W. Wernsdorfer, "Quantum Tunneling of Magnetization in Lanthanide Single-Molecule Magnets: Bis (phthalocyaninato) terbium and Bis (phthalocyaninato) dysprosium Anions," *Angewandte Chemie International Edition*, vol. 44, no. 19, pp. 2931–2935, 2005.

[16] Y. Suzuki, M. P. Sarachik, E. M. Chudnovsky, S. McHugh, R. Gonzalez-Rubio, N. Avraham, Y. Myasoedov, E. Zeldov, H. Shtrikman, N. E. Chakov, and G. Christou, "Propagation of avalanches in $Mn_{12}$-acetate: Magnetic Deflagration," *Physical Review Letters*, vol. 95, no. 14, p. 147201, 2005.

[17] S. McHugh, R. Jaafar, M. P. Sarachik, Y. Myasoedov, A. Finkler, H. Shtrikman, E. Zeldov, R. Bagai, and G. Christou, "Effect of quantum tunneling on the ignition and propagation of magnetic avalanches in $Mn_{12}$ acetate," *Physical Review B*, vol. 76, no. 17, p. 172410, 2007.

[18] A. Hernández-Mínguez, J. M. Hernandez, F. Macia, A. García-Santiago, J. Tejada, and P. V. Santos, "Quantum Magnetic Deflagration in $Mn_{12}$ Acetate," *Physical Review Letters*, vol. 95, no. 21, p. 217205, 2005.

[19] A. Hernández-Mínguez, F. Macia, J. M. Hernandez, J. Tejada, and P. V. Santos, "Phonon-induced quantum magnetic deflagration in $Mn_{12}$," *Journal of Magnetism and Magnetic Materials*, vol. 320, no. 8, pp. 1457–1463, 2008.

[20] D. A. Garanin and E. M. Chudnovsky, "Theory of magnetic deflagration in crystals of molecular magnets," *Physical Review B*, vol. 76, no. 5, p. 054410, 2007.

[21] W. Wernsdorfer and R. Sessoli, "Quantum phase interference and parity effects in magnetic molecular clusters," *Science*, vol. 284, no. 5411, pp. 133–135, 1999.

[22] M. V. Berry, "Quantal Phase Factors Accompanying Adiabatic Changes," *Proceedings of the Royal Society of London A: Mathematical, Physical and Engineering Sciences*, vol. 392, no. 1802, pp. 45–57, 1984.

[23] W. Wernsdorfer, N. E. Chakov, and G. Christou, "Quantum phase interference and spin-parity in $Mn_{12}$ single-molecule magnets," *Physical Review Letters*, vol. 95, no. 3, p. 037203, 2005.

[24] W. Wernsdorfer, M. Soler, G. Christou, and D. N. Hendrickson, "Quantum phase interference (Berry phase) in single-molecule magnets of $Mn_{12}$," *Journal of Applied Physics*, vol. 91, no. 10, pp. 7164–7166, 2002.

[25] G.-H. Kim, "Quantum phase interference in nanomagnets with tetragonal symmetry," *Journal of Applied Physics*, vol. 91, no. 5, pp. 3289–3293, 2002.

[26] C.-S. Park and A. Garg, "Topological quenching of spin tunneling in magnetic molecules with a fourfold easy axis," *Physical Review B*, vol. 65, no. 6, p. 064411, 2002.

[27] C. M. Ramsey, E. del Barco, S. Hill, S. J. Shah, C. C. Beedle, and D. N. Hendrickson, "Quantum interference of tunnel trajectories between states of different spin length in a dimeric molecular nanomagnet," *Nature Physics*, vol. 4, no. 4, pp. 277–281, 2008.

[28] W. Wernsdorfer, T. C. Stamatatos, and G. Christou, "Influence of the Dzyaloshinskii-Moriya exchange interaction on quantum phase interference of spins," *Physical Review Letters*, vol. 101, no. 23, p. 237204, 2008.

[29] M. S. Foss-Feig and J. R. Friedman, "Geometric-phase-effect tunnel-splitting oscillations in single-molecule magnets with fourth-order anisotropy induced by orthorhombic distortion," *EPL (Europhysics Letters)*, vol. 86, no. 2, p. 27002, 2009.

[30] M. N. Leuenberger and D. Loss, "Quantum computing in molecular magnets," *Nature*, vol. 410, no. 6830, pp. 789–793, 2001.

[31] A. Ardavan, O. Rival, J. J. L. Morton, S. J. Blundell, A. M. Tyryshkin, G. A. Timco, and R. E. P. Winpenny, "Will Spin-Relaxation Times in Molecular Magnets Permit Quantum Information Processing?," *Physical Review Letters*, vol. 98, no. 5, p. 057201, 2007.

[32] P. C. Stamp, "Quantum information: Stopping the rot," *Nature*, vol. 453, no. 7192, pp. 167–168, 2008.

[33] A. Morello, P. C. E. Stamp, and I. S. Tupitsyn, "Pairwise decoherence in coupled spin qubit networks," *Physical Review Letters*, vol. 97, no. 20, p. 207206, 2006.

[34] S. Bertaina, S. Gambarelli, T. Mitra, B. Tsukerblat, A. Müller, and B. Barbara, "Quantum oscillations in a molecular magnet," *Nature*, vol. 453, no. 7192, pp. 203–206, 2008.

[35] S. Takahashi, J. van Tol, C. C. Beedle, D. N. Hendrickson, L.-C. Brunel, and M. S. Sherwin, "Coherent manipulation and decoherence of S= 10 single-molecule magnets," *Physical Review Letters*, vol. 102, no. 8, p. 087603, 2009.

[36] G. Wolfowicz, A. M. Tyryshkin, R. E. George, H. Riemann, N. V. Abrosimov, P. Becker, H.-J. Pohl, M. L. W. Thewalt, S. A. Lyon, and J. J. L. Morton, "Atomic clock transitions in silicon-based spin qubits," *Nature Nanotechnology*, vol. 8, no. 8, pp. 561–564, 2013.

[37] M. Shiddiq, D. Komijani, Y. Duan, A. Gaita-Ariño, E. Coronado, and S. Hill, "Enhancing coherence in molecular spin qubits via atomic clock transitions," *Nature*, vol. 531, no. 7594, pp. 348–351, 2016.

[38] E.-C. Yang, C. Kirman, J. Lawrence, L. N. Zakharov, A. L. Rheingold, S. Hill, and D. N. Hendrickson, "Single-molecule magnets: high-field electron paramagnetic resonance evaluation of the single-ion zero-field interaction in a $Zn_3^{II}Ni^{II}$ complex," *Inorganic Chemistry*, vol. 44, no. 11, pp. 3827–3836, 2005.

[39] E.-C. Yang, W. Wernsdorfer, L. N. Zakharov, Y. Karaki, A. Yamaguchi, R. M. Isidro, G.-D. Lu, S. A. Wilson, A. L. Rheingold, H. Ishimoto, and D. N. Hendrickson, "Fast magnetization tunneling in tetranickel (II) single-molecule magnets," *Inorganic Chemistry*, vol. 45, no. 2, pp. 529–546, 2006.

[40] E.-C. Yang, W. Wernsdorfer, S. Hill, R. S. Edwards, M. Nakano, S. Maccagnano, L. N. Zakharov, A. L. Rheingold, G. Christou, and D. N. Hendrickson, "Exchange bias in $Ni_4$ single-molecule magnets," *Polyhedron*, vol. 22, no. 14, pp. 1727–1733, 2003.

[41] F. Bloch, "Nuclear Induction," *Physical Review*, vol. 70, no. 7-8, pp. 460–474, 1946.

[42] C. P. Slichter, *Principles of Magnetic Resonance*, vol. 1. Springer Science & Business Media, New York, 1996.

[43] R. S. Edwards, S. Maccagnano, E.-C. Yang, S. Hill, W. Wernsdorfer, D. Hendrickson, and G. Christou, "High-frequency electron paramagnetic resonance investigations of tetranuclear nickel-based single-molecule magnets," *Journal of Applied Physics*, vol. 93, no. 10, pp. 7807–7809, 2003.

[44] E. del Barco, A. D. Kent, E. C. Yang, and D. N. Hendrickson, "Quantum Superposition of High Spin States in the Single Molecule Magnet $Ni_4$," *Physical Review Letters*, vol. 93, no. 15, p. 157202, 2004.

[45] G. de Loubens, G. D. Chaves-O'Flynn, A. D. Kent, C. Ramsey, E. del Barco, C. Beedle, and D. N. Hendrickson, "Magnetization and EPR studies of the single molecule magnet $Ni_4$ with integrated sensors," *Journal of Applied physics*, vol. 101, no. 9, p. 09E104, 2007.

[46] G. de Loubens, D. A. Garanin, C. C. Beedle, D. N. Hendrickson, and A. D. Kent, "Magnetization relaxation in the single-molecule magnet $Ni_4$ under continuous microwave irradiation," *EPL (Europhysics Letters)*, vol. 83, no. 3, p. 37006, 2008.

[47] J. Lawrence, E.-C. Yang, R. Edwards, M. M. Olmstead, C. Ramsey, N. S. Dalal, P. K. Gantzel, S. Hill, and D. N. Hendrickson, "Disorder and intermolecular interactions in a family of tetranuclear Ni (II) complexes probed by high-frequency electron paramagnetic resonance," *Inorganic Chemistry*, vol. 47, no. 6, pp. 1965–1974, 2008.

[48] J. Lawrence, E.-C. Yang, D. N. Hendrickson, and S. Hill, "Magnetic quantum tunneling: key insights from multi-dimensional high-field EPR," *Physical Chemistry Chemical Physics*, vol. 11, no. 31, pp. 6743–6749, 2009.

[49] D. N. Hendrickson, E.-C. Yang, R. M. Isidro, C. Kirman, J. Lawrence, R. S. Edwards, S. Hill, A. Yamaguchi, H. Ishimoto, and W. Wernsdorfer, "Origin of the fast magnetization tunneling in tetranuclear nickel single-molecule magnets," *Polyhedron*, vol. 24, no. 16, pp. 2280–2283, 2005.

[50] C. C. Beedle, J. J. Henderson, P.-C. Ho, T. Sayles, M. Nakano, J. R. O'Brien, K. J. Heroux, E. del Barco, M. B. Maple, and D. N. Hendrickson, "Ferromagnetic ordering and simultaneous fast magnetization tunneling in a $Ni_4$ single-molecule magnet," *Inorganic Chemistry*, vol. 49, no. 13, pp. 5780–5782, 2010.

[51] A. Wallraff, D. I. Schuster, A. Blais, L. Frunzio, R.-S. Huang, J. Majer, S. Kumar, S. M. Girvin, and R. J. Schoelkopf, "Strong coupling of a single photon to a superconducting qubit using circuit quantum electrodynamics," *Nature*, vol. 431, no. 7005, pp. 162–167, 2004.

[52] M. Göppl, A. Fragner, M. Baur, R. Bianchetti, S. Filipp, J. M. Fink, P. J. Leek, G. Puebla, L. Steffen, and A. Wallraff, "Coplanar waveguide resonators for circuit quantum electrodynamics," *Journal of Applied Physics*, vol. 104, no. 11, p. 113904, 2008.

[53] C. P. Poole, *Electron spin resonance: a comprehensive treatise on experimental techniques: 2rd ed.* Dover Publications, Mineola, 1997.

[54] M. Tinkham, *Introduction to superconductivity: 2rd ed.* Dover Publications, Mineola, 2004.

[55] J. Bardeen and M. J. Stephen, "Theory of the Motion of Vortices in Superconductors," *Physical Review*, vol. 140, no. 4A, pp. A1197–A1207, 1965.

[56] P. Nozières and W. F. Vinen, "The motion of flux lines in type II superconductors," *Philosophical Magazine*, vol. 14, no. 130, pp. 667–688, 1966.

[57] C. Song, T. W. Heitmann, M. P. DeFeo, K. Yu, R. McDermott, M. Neeley, J. M. Martinis, and B. L. T. Plourde, "Microwave response of vortices in superconducting thin films of Re and Al," *Physical Review B*, vol. 79, no. 17, p. 174512, 2009.

[58] D. Bothner, C. Clauss, E. Koroknay, M. Kemmler, T. Gaber, M. Jetter, M. Scheffler, P. Michler, M. Dressel, D. Koelle, and R. Kleiner, "Reducing vortex losses in superconducting microwave resonators with microsphere patterned antidot arrays," *Applied Physics Letters*, vol. 100, no. 1, p. 012601, 2012.

[59] H. J. Mamin, R. Budakian, and D. Rugar, "Superconducting microwave resonator for millikelvin magnetic resonance force microscopy," *Review of Scientific Instruments*, vol. 74, no. 5, pp. 2749–2753, 2003.

[60] D. I. Schuster, A. P. Sears, E. Ginossar, L. DiCarlo, L. Frunzio, J. J. L. Morton, H. Wu, G. A. D. Briggs, B. B. Buckley, D. D. Awschalom, and R. J. Schoelkopf, "High-Cooperativity Coupling of Electron-Spin Ensembles to Superconducting Cavities," *Physical Review Letters*, vol. 105, no. 14, p. 140501, 2010.

[61] Y. Kubo, F. R. Ong, P. Bertet, D. Vion, V. Jacques, D. Zheng, A. Dréau, J.-F. Roch, A. Auffeves, F. Jelezko, J. Wrachtrup, M. F. Barthe, P. Bergonzo, and D. Esteve, "Strong Coupling of a Spin Ensemble to a Superconducting Resonator," *Physical Review Letters*, vol. 105, no. 14, p. 140502, 2010.

[62] P. Bushev, A. K. Feofanov, H. Rotzinger, I. Protopopov, J. H. Cole, C. M. Wilson, G. Fischer, A. Lukashenko, and A. V. Ustinov, "Ultralow-power spectroscopy of a rare-earth spin ensemble using a superconducting resonator," *Physical Review B*, vol. 84, no. 6, p. 060501, 2011.

[63] R. Amsuss, C. Koller, T. Nöbauer, S. Putz, S. Rotter, K. Sandner, S. Schneider, M. Schramböck, G. Steinhauser, H. Ritsch, J. Schmiedmayer, and J. Majer, "Cavity QED with Magnetically Coupled Collective Spin States," *Physical Review Letters*, vol. 107, no. 6, p. 060502, 2011.

[64] M. U. Staudt, I.-C. Hoi, P. Krantz, M. Sandberg, M. Simoen, P. Bushev, N. Sangouard, M. Afzelius, V. S. Shumeiko, and G. Johansson, "Coupling of an erbium spin ensemble to a superconducting resonator," *Journal of Physics B: Atomic, Molecular and Optical Physics*, vol. 45, no. 12, p. 124019, 2012.

[65] C. Clauss, D. Bothner, D. Koelle, R. Kleiner, L. Bogani, M. Scheffler, and M. Dressel, "Broadband electron spin resonance from 500 MHz to 40 GHz using superconducting coplanar waveguides," *Applied Physics Letters*, vol. 102, no. 16, p. 162601, 2013.

[66] H. Malissa, D. I. Schuster, A. M. Tyryshkin, A. A. Houck, and S. A. Lyon, "Superconducting coplanar waveguide resonators for low temperature pulsed electron spin resonance spectroscopy," *Review of Scientific Instruments*, vol. 84, no. 2, p. 025116, 2013.

[67] H. Huebl, C. W. Zollitsch, J. Lotze, F. Hocke, M. Greifenstein, A. Marx, R. Gross, and S. T. Goennenwein, "High cooperativity in coupled microwave resonator ferrimagnetic insulator hybrids," *Physical Review Letters*, vol. 111, no. 12, p. 127003, 2013.

[68] V. Ranjan, G. de Lange, R. Schutjens, T. Debelhoir, J. P. Groen, D. Szombati, D. J. Thoen, T. M. Klapwijk, R. Hanson, and L. DiCarlo, "Probing dynamics of an electron-spin ensemble via a superconducting resonator," *Physical Review Letters*, vol. 110, no. 6, p. 067004, 2013.

[69] S. Probst, H. Rotzinger, S. Wünsch, P. Jung, M. Jerger, M. Siegel, A. V. Ustinov, and P. A. Bushev, "Anisotropic rare-earth spin ensemble strongly coupled to a superconducting resonator," *Physical Review Letters*, vol. 110, no. 15, p. 157001, 2013.

[70] A. J. Sigillito, H. Malissa, A. M. Tyryshkin, H. Riemann, N. V. Abrosimov, P. Becker, H.-J. Pohl, M. L. Thewalt, K. M. Itoh, J. J. Morton, A. A. Houck, D. I. Schuster, and S. A. Lyon, "Fast, low-power manipulation of spin ensembles in superconducting microresonators," *Applied Physics Letters*, vol. 104, no. 22, p. 222407, 2014.

[71] K. Yoshida, K. Watanabe, T. Kisu, and K. Enpuku, "Evaluation of magnetic penetration depth and surface resistance of superconducting thin films using coplanar waveguides," *IEEE Transactions on Applied Superconductivity*, vol. 5, no. 2, pp. 1979–1982, 1995.

[72] P. C. Haljan, P. J. Lee, K. A. Brickman, M. Acton, L. Deslauriers, and C. Monroe, "Entanglement of trapped-ion clock states," *Physical Review A*, vol. 72, no. 6, p. 062316, 2005.

[73] R. Langer, C. Ozeri, J. D. Jost, J. Chiaverini, B. DeMarco, A. Ben-Kish, R. B. Blakestad, J. Britton, D. B. Hume, W. M. Itano, D. Leibfried, R. Reichle, T. Rosenband, P. O. Schmidt, and D. J. Wineland, "Long-lived qubit memory using atomic ions," *Physical Review Letters*, vol. 95, no. 6, p. 060502, 2005.

[74] Y. Chen, M. D. Ashkezari, C. A. Collett, R. A. Allão Cassaro, F. Troiani, P. M. Lahti, and J. R. Friedman, "Observation of Tunneling-Assisted Highly Forbidden Single-Photon Transitions in a $Ni_4$ Single-Molecule Magnet," *Physical Review Letters*, vol. 117, no. 18, p. 187202, 2016.

[75] S. Stoll and A. Schweiger, "EasySpin, a comprehensive software package for spectral simulation and analysis in EPR," *Journal of Magnetic Resonance*, vol. 178, no. 1, pp. 42–55, 2006.

[76] C. A. Collett, R. A. A. Cassaro, and J. R. Friedman, "Precision ESR Measurements of Transverse Anisotropy in the Single-molecule Magnet $Ni_4$," *arXiv:1609.09859 [cond-mat]*, 2016. arXiv: 1609.09859.

[77] C. Kirman, J. Lawrence, S. Hill, E.-C. Yang, and D. N. Hendrickson, "Origin of the fast magnetization tunneling in the single-molecule magnet $[Ni(hmp)(t\text{-}BuEtOH)Cl]_4$," *Journal of Applied Physics*, vol. 97, no. 10, p. 10M501, 2005.

[78] K. Bader, D. Dengler, S. Lenz, B. Endeward, S.-D. Jiang, P. Neugebauer, and J. van Slageren, "Room temperature quantum coherence in a potential molecular qubit," *Nature Communications*, vol. 5, p. 5304, 2014.

[79] C. Schlegel, J. van Slageren, M. Manoli, E. K. Brechin, and M. Dressel, "Direct Observation of Quantum Coherence in Single-Molecule Magnets," *Physical Review Letters*, vol. 101, no. 14, p. 147203, 2008.

[80] A. W. Eddins, C. C. Beedle, D. N. Hendrickson, and J. R. Friedman, "Collective Coupling of a Macroscopic Number of Single-Molecule Magnets with a Microwave Cavity Mode," *Physical Review Letters*, vol. 112, no. 12, p. 120501, 2014.

[81] F. Troiani and P. Zanardi, "Size of linear superpositions in molecular nanomagnets," *Physical Review B*, vol. 88, no. 9, p. 094413, 2013.

[82] F. Fröwis and W. Dür, "Measures of macroscopicity for quantum spin systems," *New Journal of Physics*, vol. 14, no. 9, p. 093039, 2012.

[83] L. Sorace, W. Wernsdorfer, C. Thirion, A.-L. Barra, M. Pacchioni, D. Mailly, and B. Barbara, "Photon-assisted tunneling in a $Fe_8$ single-molecule magnet," *Physical Review B*, vol. 68, no. 22, p. 220407, 2003.

[84] Y. Aharonov and D. Bohm, "Significance of Electromagnetic Potentials in the Quantum Theory," *Physical Review*, vol. 115, no. 3, pp. 485–491, 1959.

[85] Y. Aharonov and A. Casher, "Topological Quantum Effects for Neutral Particles," *Physical Review Letters*, vol. 53, no. 4, pp. 319–321, 1984.

[86] J. C. Gallop, *SQUIDs, the Josephson effects and superconducting electronics*. CRC Press, 1991.

[87] B. D. Josephson, "Possible new effects in superconductive tunnelling," *Physics Letters*, vol. 1, no. 7, pp. 251–253, 1962.

[88] J. R. Friedman and D. V. Averin, "Aharonov-Casher-effect suppression of macroscopic tunneling of magnetic flux," *Physical Review Letters*, vol. 88, no. 5, p. 050403, 2002.

[89] S. Shapiro, "Josephson currents in superconducting tunneling: The effect of microwaves and other observations," *Physical Review Letters*, vol. 11, no. 2, p. 80, 1963.

[90] L. D. Landau, "Zur theorie der energieubertragung. II," *Physics of the Soviet Union*, vol. 2, no. 2, pp. 46–51, 1932.

[91] P.-M. Billangeon, F. Pierre, H. Bouchiat, and R. Deblock, "ac Josephson Effect and Resonant Cooper Pair Tunneling Emission of a Single Cooper Pair Transistor," *Physical Review Letters*, vol. 98, no. 21, p. 216802, 2007.

[92] M. T. Bell, W. Zhang, L. B. Ioffe, and M. E. Gershenson, "Spectroscopic Evidence of the Aharonov-Casher Effect in a Cooper Pair Box," *Physical Review Letters*, vol. 116, no. 10, p. 107002, 2016.

[93] M. Kamon, M. J. Tsuk, and J. K. White, "FASTHENRY: A multipole-accelerated 3-D inductance extraction program," *IEEE Transactions on Microwave theory and techniques*, vol. 42, no. 9, pp. 1750–1758, 1994.

[94] A. B. Zorin, "The thermocoax cable as the microwave frequency filter for single electron circuits," *Review of Scientific Instruments*, vol. 66, no. 8, pp. 4296–4300, 1995.

[95] A. Lukashenko and A. V. Ustinov, "Improved powder filters for qubit measurements," *Review of Scientific Instruments*, vol. 79, no. 1, p. 014701, 2008.

[96] S. Linzen, T. L. Robertson, T. Hime, B. L. T. Plourde, P. A. Reichardt, and J. Clarke, "Low-noise computer-controlled current source for quantum coherence experiments," *Review of Scientific Instruments*, vol. 75, no. 8, pp. 2541–2544, 2004.

[97] Y. Nakamura, C. D. Chen, and J. S. Tsai, "Quantitative analysis of Josephson-quasiparticle current in superconducting single-electron transistors," *Physical Review B*, vol. 53, no. 13, p. 8234, 1996.